Universitetet i Stavanger

FACULTY OF SCIENCE AND TECHNOLOGY
MASTER'S THESIS

Study program/specialization: Petroleum Geoscience Engineering	Spring semester, 2020 Open
Author: Hanna Elisabeth Laland Hystad	………………………………………… (signature of author)
Program coordinator: Supervisor(s): Dr. Udo Zimmermann, Dr. Mona W. Minde	
Title of master's thesis: **High resolution heavy mineral studies from Silurian to Triassic successions exposed in the Altiplano of Bolivia (Central Andes).**	
Credits: 30	
Keywords: Heavy minerals Provenance Scanning Electron Microscope (SEM) Energy Dispersive Spectroscopy (EDS) Bolivia Central Andes Altiplano	Number of pages: 88 + supplemental material/other: 12 Stavanger, 26.07.20 date/year

High resolution heavy mineral studies from Silurian to Triassic successions exposed in the Altiplano of Bolivia (Central Andes)

MSc thesis

by

Hanna Elisabeth Laland Hystad

Petroleum Geosciences Engineering

Faculty of Science and Technology

University of Stavanger

Norway

TABLE OF CONTENTS

ACKNOWLEDGEMENTS

First, I would like to express my gratitude to my supervisor, Dr. Udo Zimmermann, at the University of Stavanger. I am thankful for his guidance, especially during the Corona crisis, and for giving me the opportunity to work on this specific topic. I would also like to thank my co-supervisor Dr. Mona Minde, at the University of Stavanger, for all her guidance, particularly her assistance and patience with the scanning electron microscope.

I would also like to express my gratitude to Caroline Ruud, staff engineer, for her assistance with preparing the samples in the laboratory.

I want to thank my fellow students for the all fun and support during these five years at the University of Stavanger. I would especially like to express my gratefulness to my fellow master student Irene Nerhus, who has provided encouragement and participated in valuable discussions throughout this thesis. She has also kept me company during long hours at the lab and made this trying time brighter with all her wit.

Finally, I would like to thank my family and especially my partner Håkon for all his support and patience through these years at the University of Stavanger, particularly during the many late hours I have put into this thesis, and Theodor for all his loving support.

ABSTRACT

Heavy mineral studies play an important role in the understanding of a clastic sediment or sedimentary rock. The mineral composition of a clastic rock may reflect the provenance and sedimentological processes such as sorting and weathering of the detrital grains. Further changes of the original composition at time of deposition may be caused post-depositional by diagenesis and metamorphism. The identification of different sources is useful for different fields of study like correlation purposes, reservoir evaluation and paleogeography. Bolivia is strongly underexplored in this regard, even though hydrocarbon deposits are especially abundant and base metal mining is very abundant. Therefore, this study will be significant in terms of a pilot study to demonstrate the impact of high-resolution heavy mineral studies using an electron microscope coupled with energy dispersive spectroscopy. In this thesis, the method is applied to selected formations in the Bolivian altiplano, close to La Paz, of Paleozoic to Mesozoic ages, which span over 250 million years.

Heavy mineral samples from the Silurian Cancañiri Formation display well-rounded ultra-stable minerals, and a ZTR index of 61%, indicating high reworking of the sediments. The presence of pyrite points to anoxic deposition, which may correlate with consequences of sea-level rise after the Hirnantian glacial event and is a post-depositional effect pointing to the paleoclimate changes. The Devonian samples from the Vila Vila Formation also indicate similar degree of recycling (ZTR = 54%), although some euhedral, angular zircons were observed. In addition, arc-related amphiboles were of interest and may have been sourced by newly exposed metamorphic successions. Late Paleozoic rocks of the Copacabana Formation has a ZTR index of 57%. The shapes of the ultra-stable minerals indicate multiple sources. Chutani Formation rock samples straddling the Permian-Triassic boundary comprise non-oxidized iron grains which are clear signs of an oxygen depleted depositional environment. The ZTR index for the Chutani Formation is 46%, while the Mesozoic samples of the Triassic Tiquina Formation has a ZTR index of only 23%, making it the less reworked of the five formations. The former contains amphiboles and larger amounts of apatite, which could relate to a volcanic arc. The existence of fragile minerals in some formations, such as monazite or amphibole, can point to high sedimentation rates and rapid burial combined with a rather low burial diagenesis and thin post-sedimentary cover successions. This implies that the sensitivity of high-resolution heavy mineral studies in deciphering provenance changes based on a changing tectonic environment during the Paleozoic-Mesozoic in northwest Bolivia.

LIST OF FIGURES

LIST OF TABLES

COMMONLY USED ABBREVIATIONS

APF	Apatite fraction
BSE	Back-Scattered Electron
CL	Cathodoluminescence
EDS	Energy Dispersive Spectroscopy
EMPA	Electron Microprobe Analysis
FEG	Field Emission Gun
FM	Formation
HM	Heavy minerals
keV	Kilo electron-volts
MAG	Magnetic fraction
μm	Micrometer
MLA	Mineral Liberation Analysis
SE	Secondary Electron
SEM	Scanning Electron Microscope
UiS	University of Stavanger
UMSA	Universidad Mayor de San Andrés
WD	Working distance
wt%	Weight percent
ZRF	Zircon fraction
ZTR index	Zircon-tourmaline-rutile index

1. INTRODUCTION

The Bolivian Andes (Figure 1) consist of an almost complete Phanerozoic sedimentary record, which makes it a unique window into the evolution of the Pacific margin of western Gondwana (Sempere, 1995). There are only a few studies that mention or describe the formations which will be studied within this thesis (Table 1). Most of the information that exists regarding this part of the geological record is compiled by Suárez-Soruco and Díaz-Martínez (1996). This publication is an encyclopedia, where descriptions include mainly: names of formations, ages, type localities, lithologies, sedimentological- and paleontological data. Hence at this stage of the knowledge the major achievements are partly detailed, but mainly sedimentological, paleontological and structural data (Suárez-Soruco and Díaz-Martínez, 1996). Quantification of detrital material is not carried out, besides one significant study on detrital zircons (Reimann et al., 2010). Recently, a peer-group around Prof. Zimmermann have employed modern analytical methods, including geochemistry and isotope geochemistry, to study these formations (Arntzen et al., 2018; Berg-Larsen et al., 2018; Lopez et al., 2018a, 2018b, 2018c, 2018d). Hence, provenance studies and detailed mineralogical studies which quantify with the goal of source compositions are absent. An intensive heavy mineral provenance study, like this thesis, should provide first knowledge and shed light on this part of the geological record in Bolivia.

1.1 AIM OF RESEARCH

Five key deposits have been selected, from a pool of 11 formations, based on the detrital zircon record (Arntzen et al., 2018; Berg-Larsen et al., 2018; Lopez et al., 2018a, 2018b, 2018c, 2018d). These formations exhibited a large variety of crystallization ages, and cover a timeframe of around 250 million years, crosscutting different paleotectonic settings (see below). This is an ideal situation to test heavy mineral stratigraphy for the purpose of formation correlation and evaluation of the provenance.

Hence, the major aim of the study is to investigate the provenance of five formations exposed in the Bolivian Altiplano, and to compare the abundances of components per sample through time to understand how the provenance has changed during 250 million years. 11 formations have been selected earlier but because of the Corona crisis, this had to be reduced to grain reasonable datasets throughout the stratigraphy. The five formations here presented are covering key moments during the paleotectonic evolution (see below).

1.2 OBJECTIVES

The objective of the study is to use SEM-EDS (Scanning Electron Microscope - Energy dispersive spectroscopy), in order to enhance the understanding of the detrital material for the five selected formations. The SEM-EDS will be used to identify the minerals, as well as to attempt a semi-quantification of the sample material. The results of the SEM-EDS study will help to further characterize the nature of the source material in terms of composition and tectonic setting. As the aim of the study is to monitor the changes in source material through time, one objective is to compare the different heavy mineral fractions within the samples. This will lead to a first understanding of what material has sourced the different formations, and how these sources have changed from the Silurian until the Triassic.

However, without the Corona crisis, all the 11 formations which have been separated and mounted should have been studied with an MLA (Mineral Liberation Analyzer) at TU Bergakademie Freiberg, Germany. This application enables automated quantification after a shorter study with SEM-BSE-EDS (Scanning Electron Microscope – Back-scatter Electron – Energy dispersive spectroscopy) at UiS. The crisis took away the opportunity not only to fully study the samples at UiS, but especially the quantification in Freiberg. Hence, the thesis needed to be changed and five formations have been selected as the key deposits for the same objective of the study. Furthermore, the work had to be done "by hand" and not automated, which has been more time consuming. The here presented examples are the maximum, which could have been done in this crisis.

1.3 GEOLOGICAL SETTING AND EVOLUTION

Bolivia is located in South America, and it is landlocked, bordering Peru, Chile, Argentina Paraguay and Brazil (Figure 1A). Bolivia consists of several geomorphological regions. Figure 1B illustrates the different geological provinces of Bolivia. These are, according to Sempere *et al.* (1990): the Cordillera Oriental, the Altiplano (the highlands), the Subandean belt and Llanura (the lowlands).
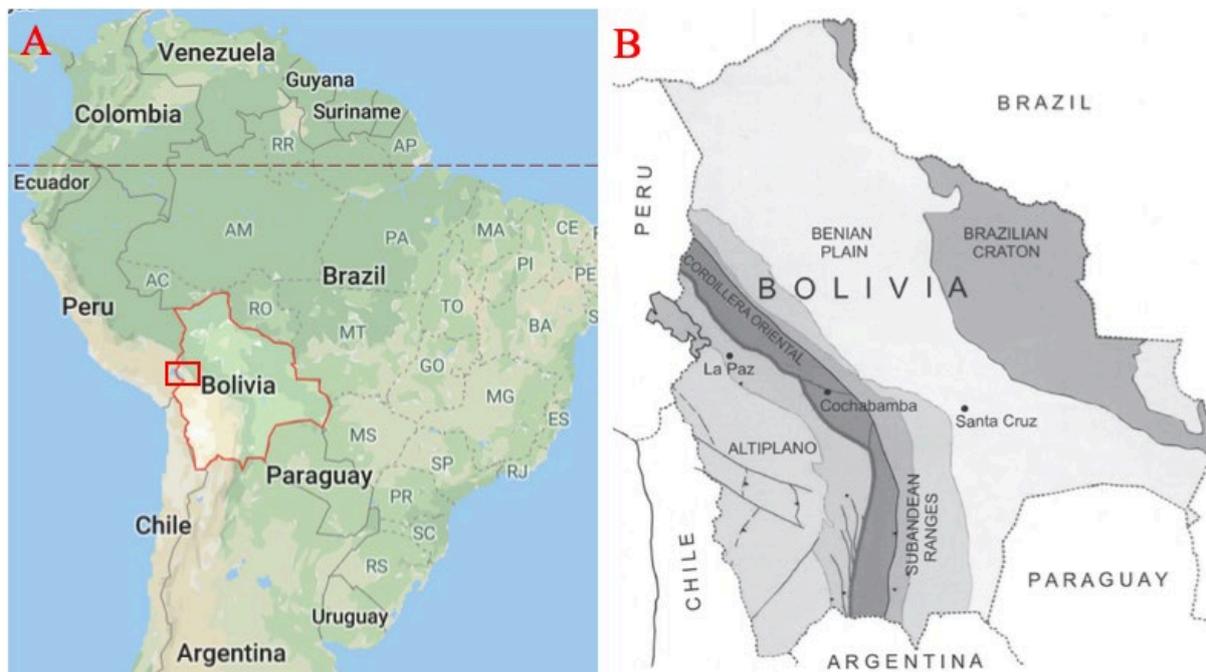
Figure 1: A) Location of Bolivia (modified from Google Maps (2020)). The red box marks the study area; B) map illustrating the different geological provinces of Bolivia (modified from Benedetto (2013); Sempere (1995); Suárez-Soruco (2000)).

Bolivia was located on the western margin of Gondwana (Sempere, 1995). The basement of Bolivia is made up of rocks from Upper Proterozoic or Lower Cambrian age (Sempere, 1995), which crop out in only a few locations in Bolivia. The oldest rocks which have been described in the Northern Altiplano, are basement rocks of an age around 1050 Ma, which were drilled in a well south of the Titicaca Lake. These metagranites are thus of an age equal to Eastern Bolivias' Sunsás orogeny (Suárez-Soruco, 2000). In the Central Altiplano, the oldest outcropping rocks are located in the Eastern Cordillera, and are gneisses and charnockites of ages around 1859 to 2024 Ma (Suárez-Soruco, 2000).

The Arequipa Massif was the center of the Ordovician arc (Figure 2). It is thought that the Ordovician arc may be a continuation of the Famatinian arc system in Argentina and Chile

to the south of Bolivia (Zumsprekel et al., 2015). During the Ordovician, Bolivia was dominated by extension and high subductions rates (Sempere, 1995), which was reflected in a large sedimentary basin developing in northern Bolivia, to the east of Arequipa Massif (Bahlburg et al., 2009) and west of the Amazon Craton (Reimann et al., 2010). This basin is called the Peru-Bolivia trough, and it persisted during Ordovician to Devonian times. During this period, the basin received a large amount of sediment thought to have originated from both the Pampean Orogen, and the Sunsás Orogen to the east (Bahlburg et al., 2011) (Figure 2). The basin was oriented parallel to the modern Pacific margin, and it was restricted by the Sierras Pampeanas to the east of the basin. The geometry of the basin resulted in marine transgressions entering Bolivia from the northwest, from the late Ordovician to Paleocene (Sempere, 1995).
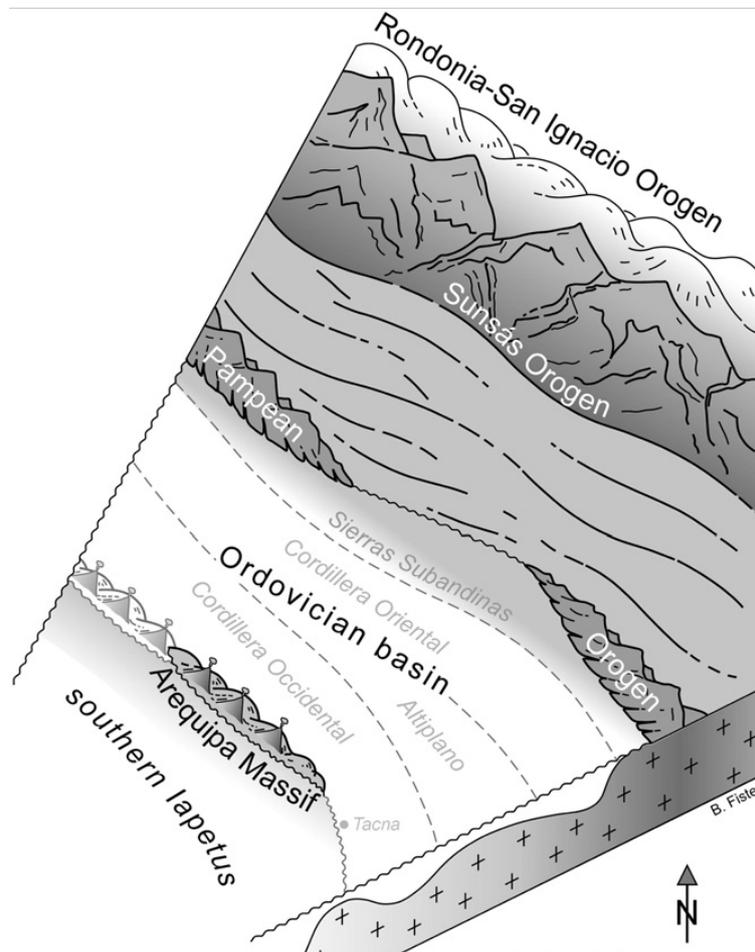
Figure 2: Ordovician paleography of the northern part of Bolivia, with the marine Ordovician basin drawn in relation to Arequipa Massif and the orogens in the east. Note the possible bypass for sediments through the Pampean Orogen (from Bahlburg et al. (2011)).

There has been continuous subduction of the western part of South America since the Cambrian or before (Bahlburg et al., 2009) and which probably continued until Early Devonian (Reimann et al., 2010), when there is no longer evidence of activity such as subduction and arc magmatism along the mentioned margin (Bahlburg et al., 2009). The Ordovician basins of the region are suggested to have formed in an active plate margin, due to the general scarcity of outcrops of that age in the Arequipa Massif (Reimann et al., 2010).

The western margin of South America probably developed into a passive margin during the Silurian and Devonian, which lasted until the Early Carboniferous (Zumsprekel et al., 2015). This is based on the lack of evidence of subduction and arc magmatism in the rock record (Bahlburg et al., 2009). While other authors (Jiménez and López-Velásquez, 2008) consider there to have been subduction of the paleo-Pacific oceanic crust below the Arequipa-Antofalla microcraton (Figure 3). Active subduction in the Central Andean region may have ceased or reinitiated during Permian times, as a result of the amalgamation of Pangea (Sempere, 1995). It is proposed that from the Late Permian, to the Late Triassic, there existed a tectonic quiescence, until the margin yet again experienced subduction, which has continued into the Andean cycle (Bahlburg et al., 2009). Suárez-Soruco (2000) define the geological history of Bolivia, by dividing it into two episodes, based on the breakup of Gondwana around 200 Ma. These are the Pre-Andean and the Andean episodes (Suárez-Soruco, 2000).

The main cause for the Andean orogeny, is the eastward movement, and subduction of the Nazca oceanic plate beneath the South American plate (Jaillard et al., 2000). The formation of the Bolivian Andes is as recent as the late Oligocene (Sempere, 1995). The Altiplano of Bolivia was formed during the Cenozoic, as the uplifting of the Eastern Cordillera initiated, and it is an intermountain basin of $110\,000$ m^2 (Suárez-Soruco, 2000). The Arequipa region was thrusted over the Guaporé Craton in the east, during the Paleocene-Eocene, when the formation of the Altiplano began (Suárez-Soruco, 2000).
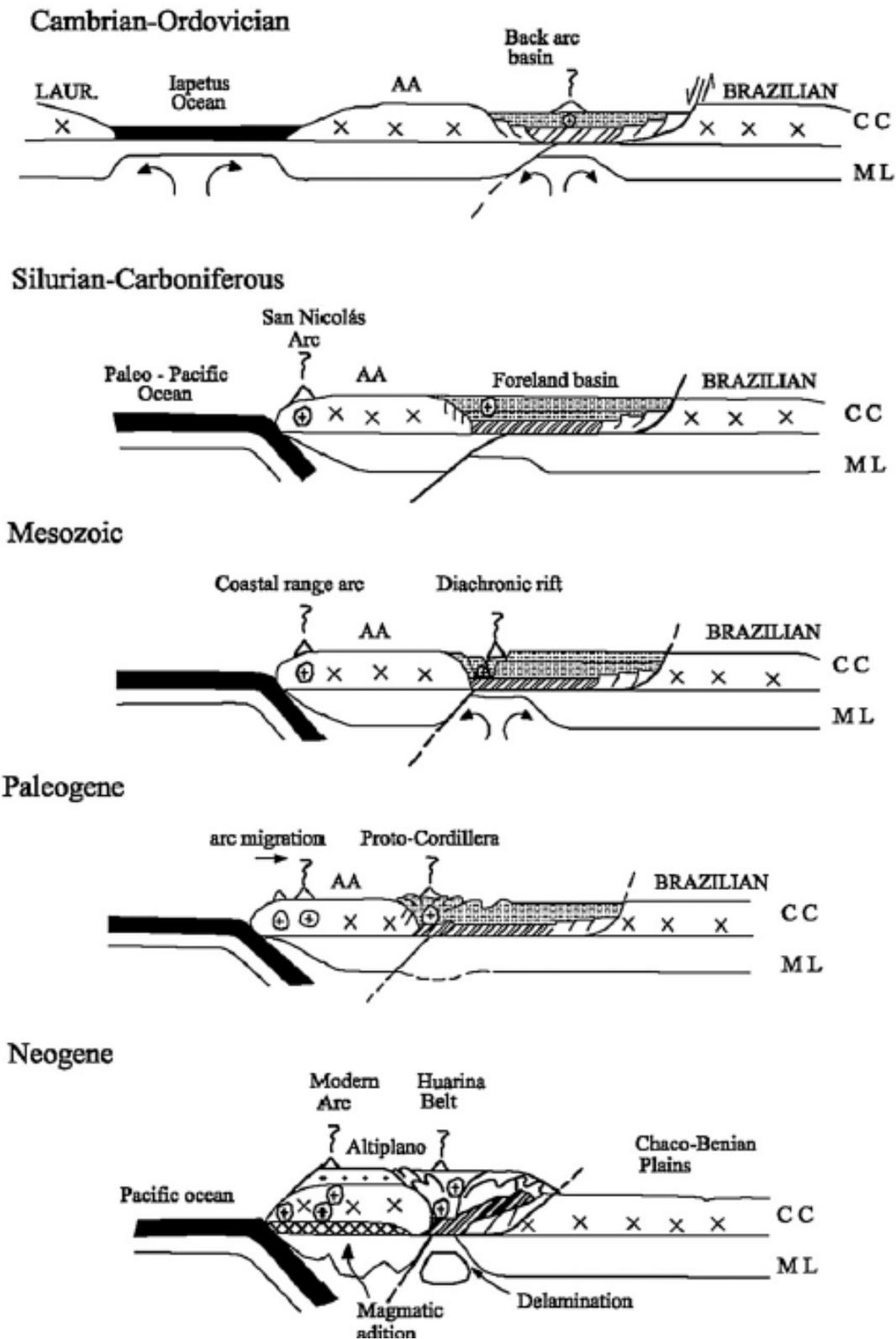
Figure 3: Evolution of the Bolivian Andes from Cambrian to recent. LAUR: Laurentia; AA: Arequipa-Antofalla craton; CC: continental crust; ML: mantle lithosphere (from Jiménez and López-Velásquez (2008)).

Sempere (1995) has summarized the evolution of the Bolivia-Peru basin from the Cambrian to Recent. Tectonically, several extensional phases have taken place, from the Late Cambrian to the Early Ordovician, during the Ordovician (Katian to Llandovery), in the late Middle Triassic, from latest Jurassic to the Early Cretaceous, and during the middle Upper Cretaceous. There was regional or local compression and uplift from the Ordovician (Dapingian to Katian), from Late Devonian to the Mississippian, during the Late Permian, during the Late Triassic and during late Paleocene, as well as from late Oligocene to the Neogene. There was magmatism in local areas only, which was caused by either late-arc activity or post-arc extension. This magmatism occurred from Early to Late Triassic and from late Oligocene to the Neogene. Sedimentologically there were high subsidence rates from the Late Cambrian to the Mississippian, as well as from Upper Cretaceous to Recent. There were also transgressions, which are grouped into three time-intervals. These transgressions occurred from the Ordovician to Mississippian, from the Pennsylvanian to the Late Permian and from Late Cretaceous to Danian and are connected to the major tectonic events (Sempere, 1995).

These events have strongly affected, if not controlled, the source material composition of the formations studied in this thesis and should be possible to identify within heavy mineral compositions.

1.3.1 Stratigraphy

The Cancañiri Formation is the oldest formation studied in this thesis, at the bottom of the stratigraphy (Figure 4), and is proposed to represent a glacial or peri-glacial deposit of Late Ordovician to Early Silurian age. The Cancañiri Formation is overlain by the Llallagua Formation, but not in the Altiplano of Bolivia and therefore not part of this thesis. Unconformably/conformably overlying the Cancañiri Formation is the Uncía Formation which is described as shallow shelf marine fine-grained sediments (Suárez-Soruco, 2000). The Uncia Formation is overlain by the Catavi Formation, which has been deposited at a shallow shelf with coastal influence, during the upper Silurian (Suárez-Soruco, 2000). The sequence is followed by coastal to deltaic sandstones of the Vila Vila Formation of Devonian age (Suárez-Soruco, 2000). These rocks are overlain by those of the Belen Formation, which was deposited at a greater water depth corresponding to a shallow- to deep shelf environment, still of Devonian age (Suárez-Soruco, 2000). The stratigraphy continues with the shallow shelf coastal marine deposits of the Sica Sica Formation and Colpacucho Formation, both of Upper

Devonian age (Suárez-Soruco, 2000). The Colpacucho Formation consists of shallow marine shales (Isaacson and Martínez, 1995) and it is overlain by the Ámbo Group. The Ámbo Group was formed due to coastal progradation (Isaacson and Martínez, 1995), and it is a complex coarsening and thickening upwards sequence consisting of the Cumaná, Kasa, and Siripaca Formations (Isaacson and Martínez, 1995). The Cumaná Formation consists of Devonian to (Upper?) Carboniferous possibly glaciomarine deposits (Arntzen et al., 2018) which marks the base of the Ambo Group, followed by the Kasa Formation which consists of Carboniferous shallow marine deltaic deposits and is divided into the lower and upper member. The lower member corresponds to a shallow clastic shelf, which is dominated by wave and storm depositions, with interbedded braided alluvial plane deposits, while the upper member of the Kasa Formation is a fan delta complex. The Siripaca Formation, which is not exposed in the Bolivian Altiplano, is the last member of the Ambo Group. It consists of fluvial dominated deltaic plain deposits, which comprises of meandering rivers as a contrast to the braided rivers of the Kasa Formation (Isaacson and Martínez, 1995). The Siripaca Formation is also a coal bearing unit, with plant remnants (Suárez-Soruco, 2000). A late Carboniferous transgression resulted in the development of a shallow carbonate ramp (Isaacson and Martínez, 1995), which is assigned to the Copacabana Formation of Upper Carboniferous to Lower Permian age (Suárez-Soruco, 2000). This is followed by the Permian Chutani Formation, consisting of transitional deltaic and coastal deposits with influence from aeolian and fluvial environments (Suárez-Soruco, 2000). Only at the Titicaca Lake (Figure 5), the Triassic Tiquina Formation conformably/unconformably overlies the Chutani Formation. The Tiquina Formation consist of volcaniclastic sediments and it is of Triassic age (Suárez-Soruco, 2000).
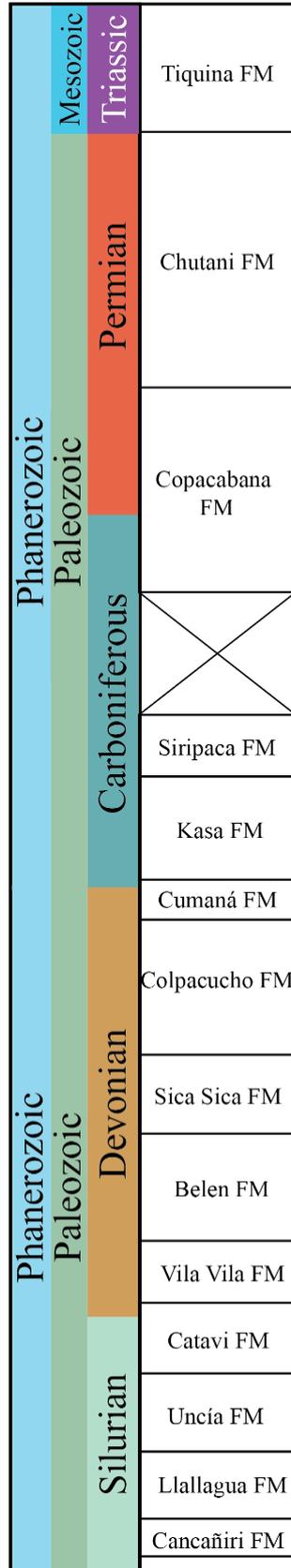
Figure 4: Simplified stratigraphic column of the Bolivian Andes. Modified from Suárez-Soruco (2000), and Suárez-Soruco and Diaz-Martínez (1996). FM = Formation.

All samples were collected in outcrops in the Altiplano of Bolivia. Figure 5 is a map of the sample area, with sample locations marked by stars. This map area corresponds approximately to the red box in Figure 1A.
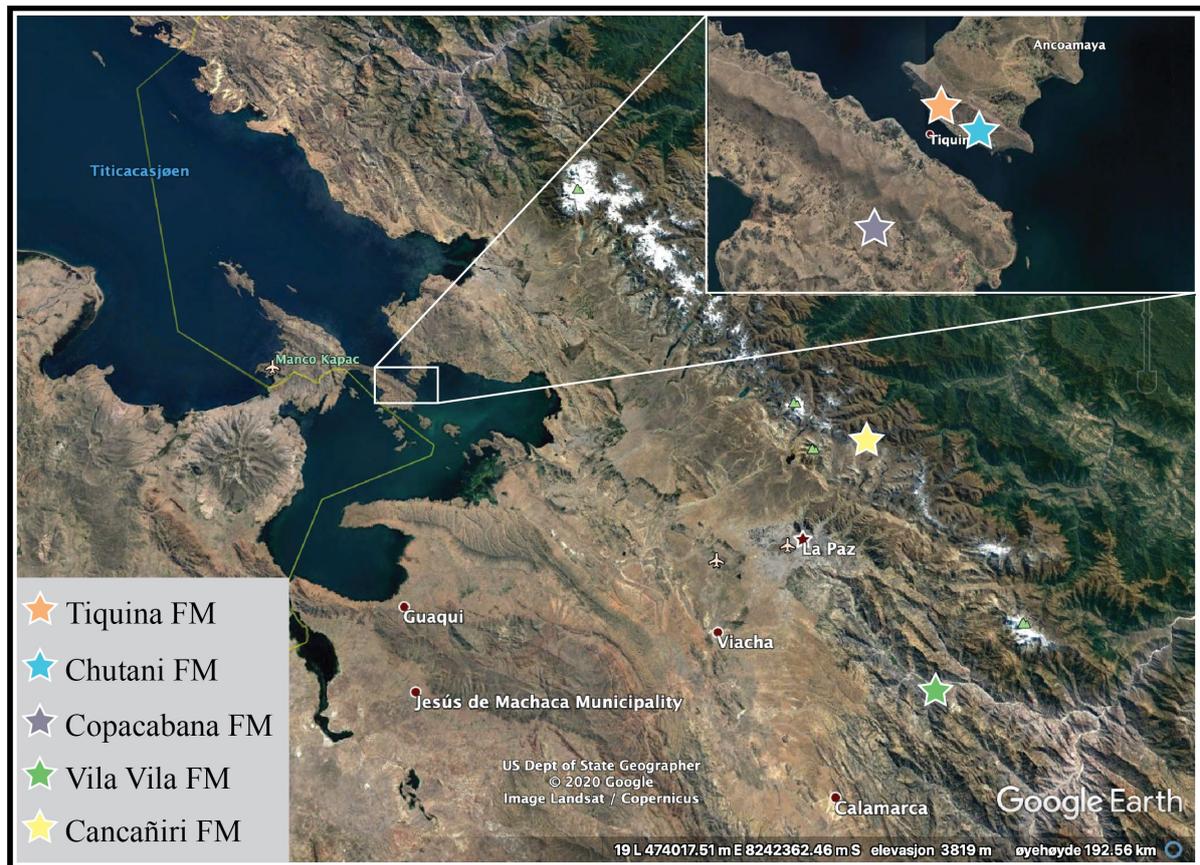
Figure 5: Map of sample locations. Titicaca Lake is seen to the left in the map (modified from Google Earth (2020)). The map area corresponds approximately to the red box in Figure 1A. FM = Formation.

Five formations were picked from 11 available formations. This was based on initial findings from SEM-EDS analysis of all 11 formations, and available zircon ages (Arntzen et al., 2018; Berg-Larsen et al., 2018; Lopez et al., 2018a, 2018b, 2018c, 2018d). As mentioned above, the Cancañiri Formation has been deposited shortly after the cessation of arc magmatism during post-Upper Ordovician, the Vila Vila Formation during the major transgression in Devonian times, the Copacabana Formation during emergence of another volcanic arc and the two last formations may represent still syn-arc sediments (Chutani Formation) and definitely post arc deposits (Tiquina Formation). These formations are listed in Table 1. Each formation corresponds to three heavy mineral fractions each; (i) magnetic fraction, (ii) apatite fraction and (iii) zircon fraction (see below for definition of these).

The five formations which will be the focus of this thesis are marked in bold in Table 1. Time constrains caused by the Corona crisis did not allow for more studies during half a year of work due to laboratory closures, but the selected samples are sufficient enough to interpret the evolution, as the selection is based on the results of detrital zircon dating carried out for a variety of theses or exist already as unpublished data. The unpublished data contain a tendency in reflecting different dominant source regions (Arntzen et al., 2018; Berg-Larsen et al., 2018; Lopez et al., 2018a, 2018b, 2018c, 2018d).

Table 1: List of samples, sorted by age, starting with the oldest at the bottom of the table. The list includes 11 formations, where the sample names for each formation is listed. Note that each sample corresponds to three heavy mineral fractions. Preliminary analyses were carried out for all samples, and the most interesting ones were selected for further study. The highlighted samples (in bold) are the major targets for this study. The last column gives the percentage of heavy minerals (density above 2.95).

Formation	Sample name	Age	Lithology	% > 2.95 (heavy minerals)
Tiquina	**TQ7**	**Triassic**	Redbed sandstones	**0.33**
Chutani	**CH-D**	**Permian**	Shales, marls, dolomites and sandstones	**0.21**
Copacabana	**COPA1**	**Carboniferous - Permian**	Limestones, marls, shales, sandstones and tuffs	**0.08**
Kasa	KAS1	Carboniferous	Sandstones and shales, with diamictite intercalations	
Cumaná	CU2	Devonian- Carboniferous	Diamictites with sedimentary blocks and sandstone, and conglomerate intercalations	
Vila Vila	**VV1**	**Devonian**	Sandstones and quartzitic sandstones	**0.29**
Colpacucho	CLP	Devonian (Givetian - Frasnian)	Shale and sandstones	
Sica Sica	SS1	Devonian	Alternation of sandstones and shales	
Uncía	UN	Silurian (Wenlock - Ludlow)	Shales, siltstones and sandstones	
Catavi	CAT	Silurian (Ludlow - Pridoli)	Sandstones with intercalations of shales	
Cancañiri	**CCE**	**Ordovician**	Diamictites, with interspersed sandstones and shales	**21.4**

2. METHODS

Originally, three methods were planned to analyze the heavy mineral samples: Scanning Electron Microscope coupled with Energy Dispersive Spectroscopy (SEM-EDS), Mineral Liberation Analysis (MLA), and Electron Microprobe Analysis (EMPA). Due to the Corona crisis, only the method available at the University of Stavanger (UiS), could be used. Therefore, only SEM-EDS analysis of the samples were carried out, and MLA or EMPA were not used. Initially, samples from all 11 formations were mounted, and preliminary analysis were carried out using an optical microscope and SEM-EDS at UiS for 10 of the formations, before the Corona crisis occurred and the laboratory facilities at UiS shut down. As the number of samples had to be limited due to the university shutdown during the corona crisis, and the European travel ban, only five of the 11 formations were included in further study and presented in this thesis.

As the sample material already existed at UiS, the first step was to mount the sample material, using an optical microscope, before gluing, polishing, and coating the samples for SEM. Then the samples were analyzed using SEM-EDS and imaged using BSE (Back-scattered electron). Minimum 100 to 150 heavy mineral grains were needed to be identified, per sample, for semi-quantification of heavy minerals.

2.1 SAMPLING AND SEPARATION

The rock samples were collected in Bolivia over the last five years as part of several Bachelor- and Master thesis projects from students from UiS and UMSA (Universidad Mayor de San Andrés) under the supervision of Prof. Zimmermann. The heavy mineral separation was similar for all samples and it was carried out by a third party in Australia. A sample is separated into four fractions: (i) magnetic fraction, (ii) apatite fraction, (iii) zircon fraction and (iv) zircon concentration. These are differentiated by their magnetic characteristics and specific density: the zircon fraction (ZRF) is nonmagnetic and above 3.3 g/cm^3, the apatite fraction (APF) is nonmagnetic and between 2.7 and 3.3 g/cm^3, and the magnetic fraction (MAG) is magnetic and above 2.7 g/cm^3. These three fractions will be studied in this thesis, while the zircon concentrate will not be a part of the study as it merely comprises zircons, which have previously been used for age determinations of the formations.

Each fraction consists of a large number of grains. Before analyzing a representative sample of grains, these were mounted in epoxy. Prior to pouring out any material, the container was shaken in order to mix the material. Two methods of securing a random selection of grains were used, depending on the amount of sample material. For samples with a large amount of sample material, all of the sample material was poured out on a paper and then divided equally into smaller and smaller portions, using a razor blade, until there was a small enough amount of sample material to handle. For the samples with very little sample material only a small amount of the sample was carefully poured onto the paper. Then this portion of grains was used to pick from, before it was set aside, and a new portion was poured out and picked from, before set aside. This was repeated until the container was almost empty. The last remainder of grains were often sticking to the walls of the container and was either retrieved from the container by knocking it into the paper or rinsing it out of the container using ethanol or acetone. This was done to ensure that all the different minerals were represented in the mount which were to be analyzed. A static needle was used to transfer the grains onto double sided tape which was fastened to a plastic plate. This was done under a binocular microscope (Zeiss Stemi DV4). Different amounts of grains were needed for each fraction of the sample. For the magnetic fraction, five rows, with a total of 400-600 grains were needed for the mount. For the apatite and zircon fraction, about two rows, with a total of minimum 200 grains were needed.

A FixiForm was placed over the plastic plate (Figure 6A), which was placed into a CitoVac machine (Figure 6B), which has a vacuum chamber. The epoxy entered the chamber through a hose and was poured into the FixiForm. The vacuum ensured less air bubbles in the epoxy mount, and for an even better result, the epoxy mixture was heated in a heating cabinet before use. After drying, the surface of the mount was grinded on a glass plate, with silicon carbide powder until the grains were adequately exhumed. A Struers Rotopol-35 machine was used for the polishing, using diamond-suspension powder in combination with different polishing cloths. The polishing cloths are called "DAC" and "NAP", and were combined with a three μm diamond suspension, and a one μm diamond suspension respectively. A finished (but not polished) mount is displayed in Figure 6C.

Figure 6: A) A FixiForm placed on the tape acts as a casing for the epoxy; B) The CitoVac machine used to apply vacuum and distribute the epoxy; C) How a finished unpolished heavy mineral mount looks like (sample MAG4). Scalebar is 25 mm.

2.2.1 Mount maps

Maps of all the mounts which were initially made as part of this thesis are displayed in Figure 7. The sample names are written inside each corresponding line, and the mounts are named according to which fraction they correspond to. The samples which were analyzed and presented as part of this thesis are: CCE (Cancañiri Formation); VV1 (Vila Vila Formation); COPA1 (Copacabana Formation); CH-D (Chutani Formation); TQ7 (Tiquina Formation). How these correspond to mount names is also explained in Table 2.

Table 2: Sample names and corresponding mount names.

Formation	Sample name	Mount name zircon fraction	Mount name apatite fraction	Mount name magnetic fraction
Cancañiri	CCE	ZRF1	APF1	MAG1.1
Vila Vila	VV1	ZRF3	APF3	MAG3
Copacabana	COPA1	ZRF4	APF4	MAG4
Chutani	CH-D	ZRF5	APF5	MAG5
Tiquina	TQ7	ZRF5	APF5	MAG5
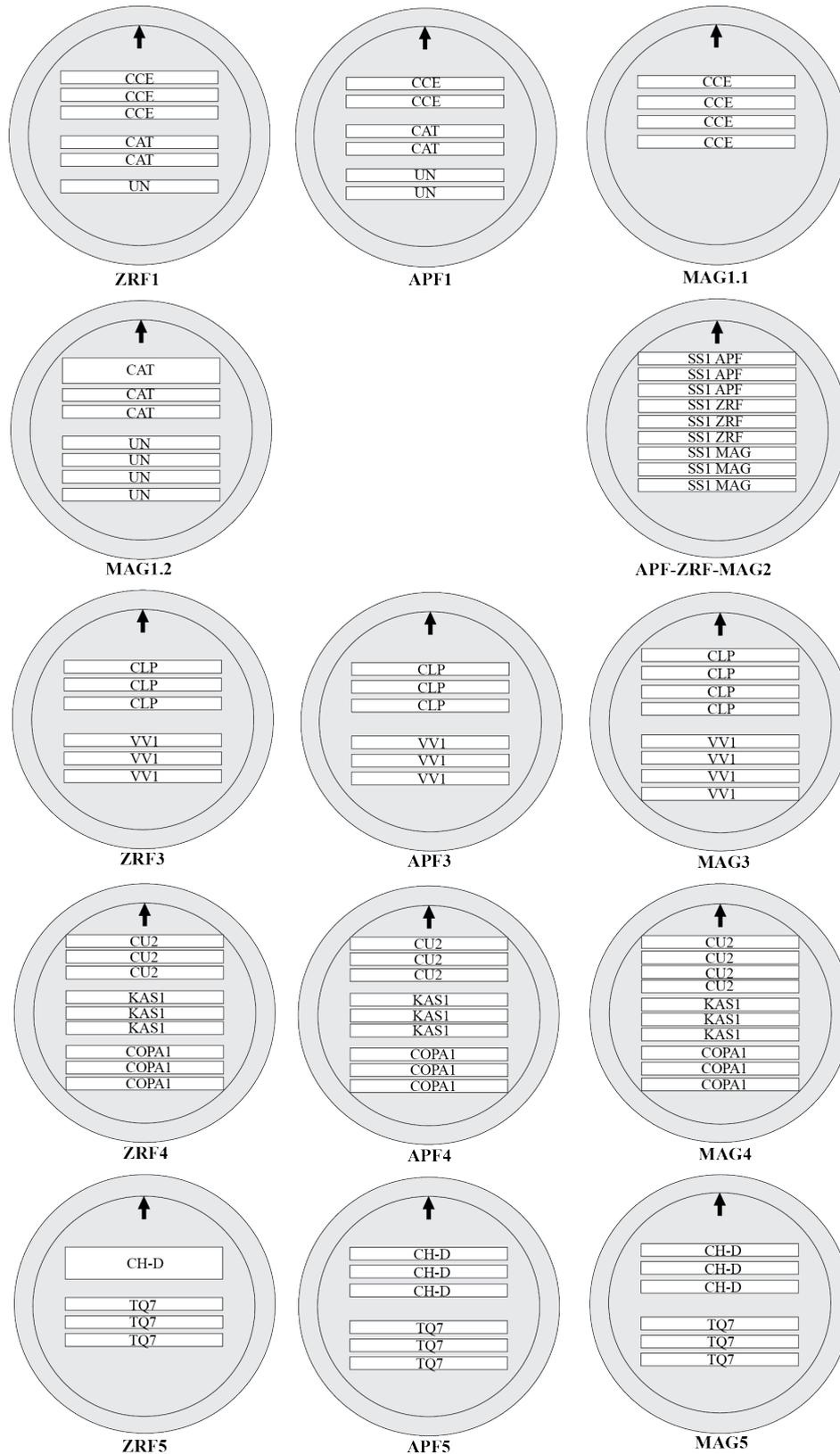
Figure 7: Mount maps for all samples which were mounted for this thesis. Sample names inside their respective lines. Mount name underneath each mount, which corresponds to the heavy mineral fraction(s). Samples that are part of this study: CCE = Cancañiri FM (Formation); VV1 = Vila Vila FM; COPA1 = Copacabana FM; CH-D = Chutani FM; TQ7 = Tiquina FM.

29

2.3 OPTICAL MICROSCOPE

An optical microscope was used for preliminary studies of the samples. Images of the mounts were also taken using an optical microscope which was connected to a computer. For these purposes, an Olympus SZX16 microscope and the software "Stream start" were used. The images were used for orientation when analyzing the mounts in the SEM-EDS, and for the purpose of studying the colors and shapes of the grains.

2.4 FIELD EMISSION GUN - SCANNING ELECTRON MICROSCOPE (FEG-SEM)

At UiS a Zeiss Supra 35VP Field Emission Gun Scanning Electron Microscope (FEG-SEM) (Figure 8) was used to analyze the samples. The mounted samples were analyzed and quantified using the Scanning Electron Microscope – Energy Dispersive Spectroscopy (SEM-EDS) in Back-scattered Electrons (BSE) mode.
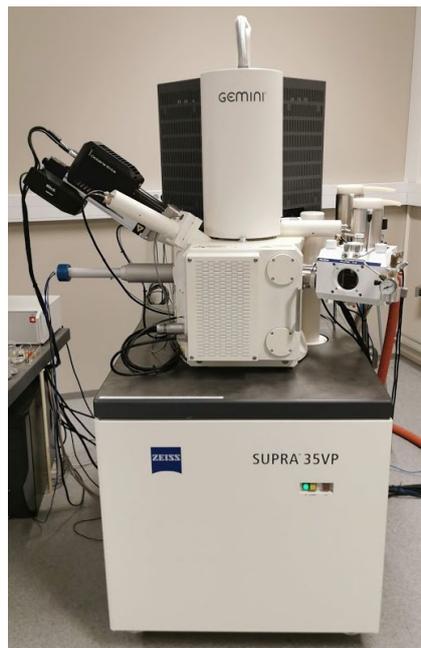
Figure 8: Zeiss Supra 35VP Field Emission Gun Scanning Electron Microscope

At least 100 grains from each sample were analyzed to ensure enough grains for the results to be quantifiable. To ensure a random selection of material and to limit the possible sources of errors, as the semi-quantification of the samples were carried out, a set interval was used to "jump" through each line, depending on the amount of sample material. As there seems to be larger grains at the beginning of line one, and then decreasing grain size throughout the lines

for each sample/fraction, it was important to not only analyze 100 grains at the beginning of each sample/fraction, but to jump through the sample and analyze a random selection of grains for each interval until the entire sample/fraction was covered. As the smaller grains seemed to be of different minerals than the larger grains, it was very important to limit this source of error.

The SEM was set to 20-25kV acceleration voltage, aperture size 30 or 60 μm, and a working distance of 10 mm. When analyzing using the EDS detector, the count time was set to 20 live seconds. For the cathodoluminescence (CL) images, the aperture was set to 120 μm.

2.4.1 Theoretical background

The scanning electron microscope includes an electron gun, which in this case is a field emission gun (FEG), as well as different electromagnetic lenses and detectors (Figure 9). The field emission gun has a rod-shaped cathode with a sharp point at the end, which is held at a negative potential compared to the anode. This results in a very strong electric field at the tip of the cathode which creates a tunneling effect where the electrons can travel through the barrier without the need for any thermal energy in order to lift the electrons over the barrier (Goldstein et al., 1981).
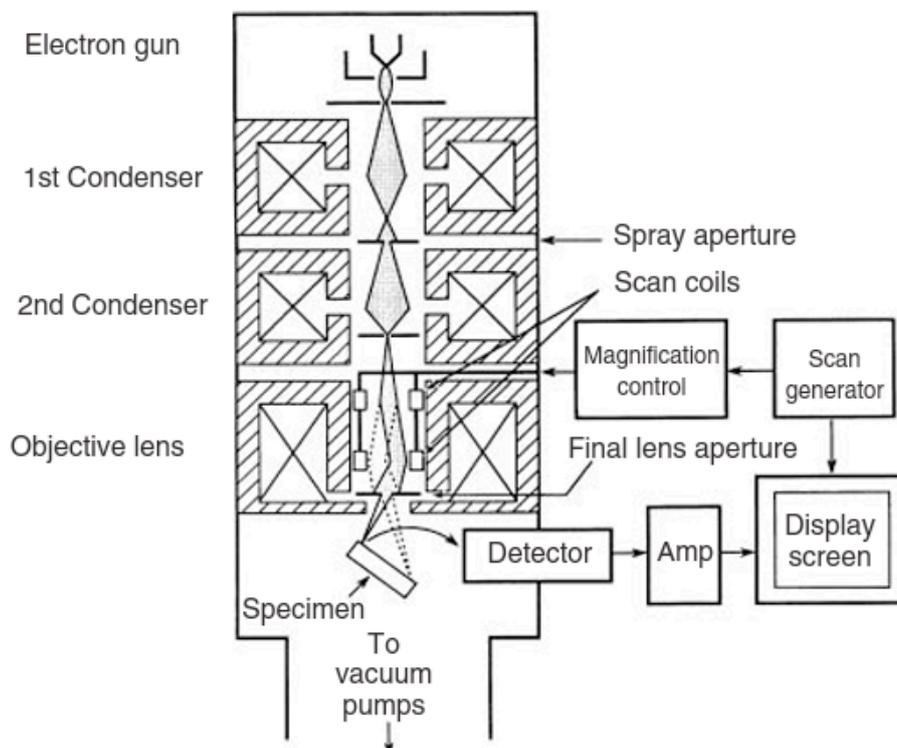
Figure 9: Configuration of a scanning electron microscope (from Leng (2013)).

As the electron gun sends out an electron beam, several electromagnetic lenses are used to focus the beam. As this focused electron beam is directed onto the sample material, different signals are reflected (Figure 10), all depending on the penetration depth of the electron beam into the sample material. The different signals which are reflected from the sample are recognized by several different detectors. These signals are the back-scattered electrons (BSE), the secondary electrons (SE), X-rays, auger electrons and photons (Hjelen, 1989). The samples need to be coated with a conductive material to become conductive, and prevent electrons building up on the surface of the mount during SEM analysis. The mounts were coated with carbon using an Emitech K550 Sputter Coater.

Back-scattered electrons (BSE)

Cathodoluminescence (CL)

Continuous X-rays

Electron beam

Characteristic X-rays

Secondary electrons (SE)

Auger electrons
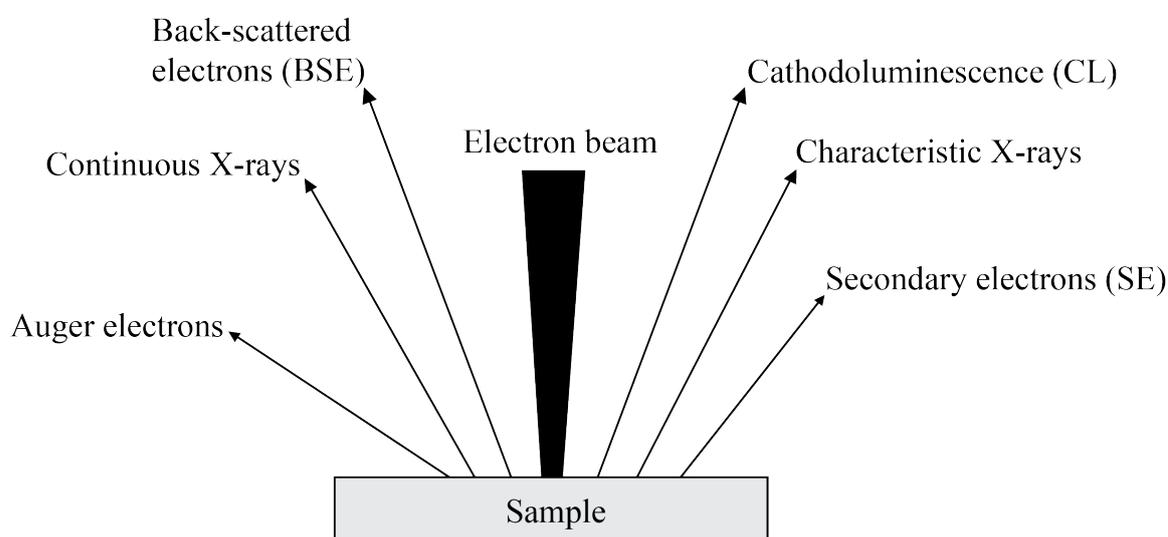
Sample

Figure 10: Signals which can be detected in the SEM as an electron beam is directed at the sample surface. These include back-scattered electrons (BSE), auger electrons, Secondary electrons (SE), continuous and characteristic X-rays, and cathodoluminescence (CL) (modified from Hjelen (1989)).

To identify different minerals in the SEM, Back-Scattered Scanning Electron Microscopy combined with Energy dispersive spectroscopy (BSE-SEM-EDS) has been used. Databases such as mindat.org, webmineral.com and other literature (Deer et al., 1992) were then employed to interpret the chemical composition to determine the corresponding mineral.

2.4.1.1 Back-Scattered Electron (BSE) detector

This detector collects the above-mentioned back-scattered electrons which are reflected from the sample material. As elements have different atomic numbers, depending on the atomic number, the elements appear lighter or darker when using the Back-Scattered Electrons (BSE) detector in the SEM. The higher atomic number, the element creates a stronger field, and thus attracting more of the incoming electrons from the electron gun. This causes an elastic interaction, which will send the electrons back out of the sample. When the elements have a low atomic number, the field around the atoms nucleus is weaker, and the electrons sink deeper into the sample, and less electrons can be reflected from the sample to the detector. This will cause a significant change in the number of back-scattered electrons that reach the detector, depending on the atomic number of the element. Thus, the lighter elements will appear darker and the heavier elements will appear brighter. This allows the different elemental composition to be viewed in greyscale in the SEM, when using the BSE detector, and give an idea of the composition of the sample to choose what to examine using EDS. The advantage of this detector is that the light minerals, which contain lighter elements, will appear dark, while the heavy minerals which are of interest in this thesis, will appear brighter and are then easy to distinguish (Figure 11). When working with the sample for some time, it will be possible to predict the composition of each grain using only the theory behind the BSE detector, even without further analysis.
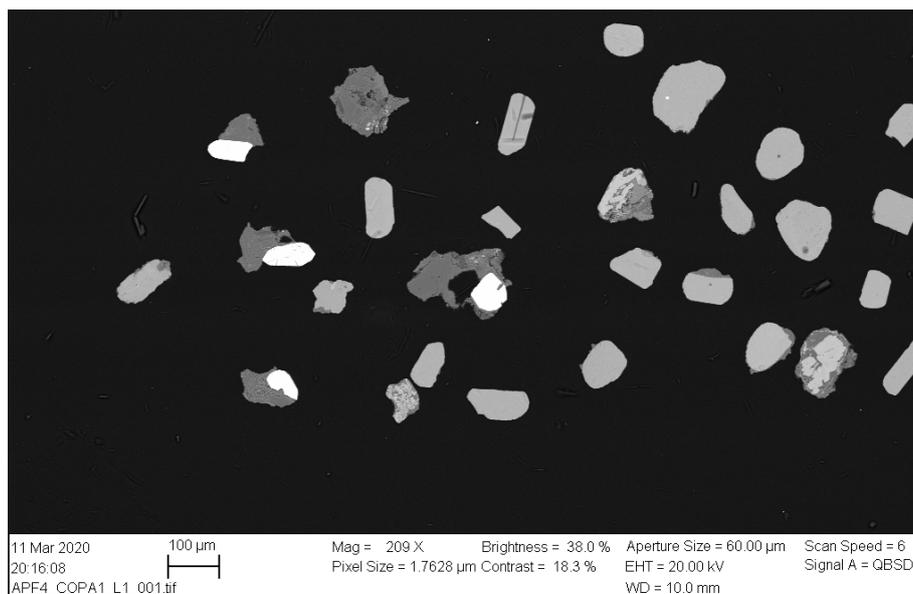
Figure 11: Example of apatite fraction (Copacabana Formation) in BSE mode. Note the different grayscales, which makes it possible to differentiate the minerals in some cases without further analysis. Darker minerals are composed of lighter elements than brighter minerals.

2.4.1.2 Energy Dispersive Spectroscopy (EDS) detector

The Energy Dispersive Spectroscopy (EDS) detects the energy of the X-rays that are emitted by the sample material, to identify the chemical composition of the grains. When the electron beam reaches the sample material, electrons from the beam will hit electrons in the atoms of the material being investigated (Figure 12). As this happens, the electron from the beam will knock out an electron (secondary electron) in an atom shell, and then be scattered itself. Since a void in the electron shell is made, the atom becomes ionized. The atom is then in an excited state (Leng, 2013), and thus, an electron from an outer shell will move in to fill this void. As this electron moves from one shell to the other, an X-ray photon (characteristic X-ray) is emitted (Hjelen, 1989) or an Auger electron (free electron) (Leng, 2013). The energy difference between two electrons in different electron shells, define the energy of the characteristic X-rays. This energy difference relies on the atomic number of the atom, such that by using the characteristic X-rays for each element, the software may detect which elements are present in the sample. The EDS can be used to analyze either an area of the sample, or single points. The spot size is approximately 1-2 μm in diameter.

The EDS at UiS is an EDAX Octane Elite 25 detector. The software which was used together with this detector is called "Team".
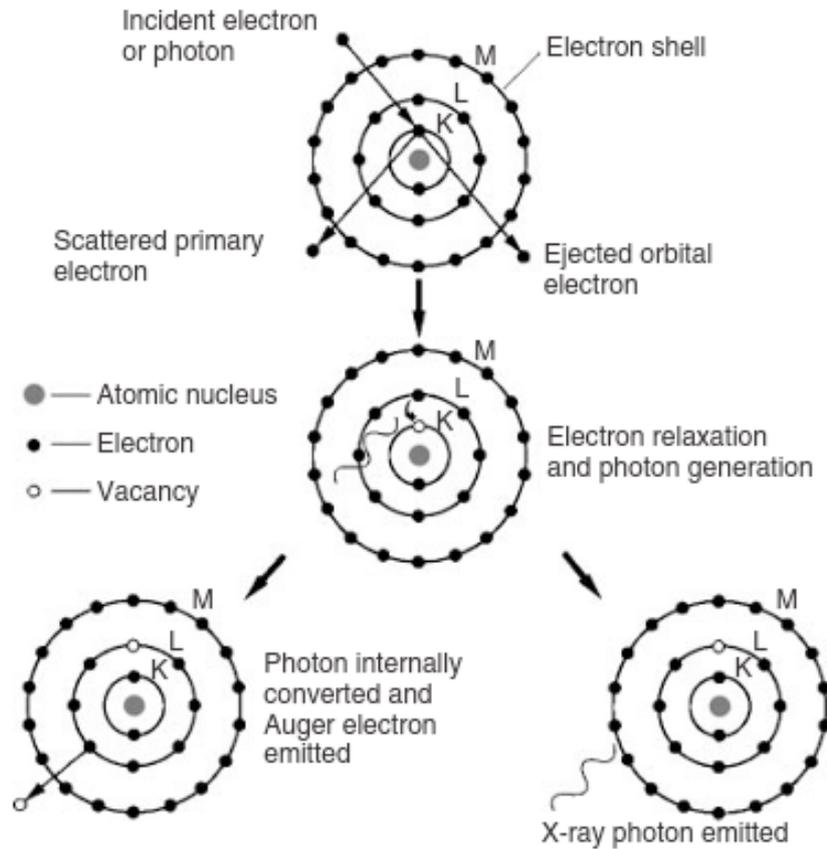
Figure 12: Generation of characteristic x-rays. The incident electron represents the electron bean from the electron gun, which will expel an electron in the atom, and be scattered. As an electron from an outer shell moves to fill the whole in the inner electron shell, photons are emitted. These are the characteristic X-ray photons (from Leng (2013)).

2.4.1.3 Cathodoluminescence (CL) detector

The cathodoluminescence (CL) detector collects the light, which is emitted by the sample material, when the sample is bombarded by electrons. This may happen in some types of material. As the electron beam hits the atoms in the sample, excitation occurs. This results in emission of photons, which can be distinguished by the CL detector. Not every mineral can display cathodoluminescence, but zircon is among those that can produce it, and which will be examined using the CL detector in this thesis (zircon fraction samples).

3. RESULTS

3.1 SEMI-QUANTIFICATION AND DESCRIPTIONS OF HEAVY MINERAL SAMPLES

The FEG-SEM semi-quantification of the samples which were chosen for this study, are presented in Table 3. The results are also illustrated graphically in Figure 13 (ZRF), Figure 14 (APF) and Figure 15 (MAG). Examples of EDS spectrums for the different minerals are given in Appendix A.

For the purpose of these figures/tables, all iron oxides are grouped into one datapoint labelled "iron oxide", and all unknown minerals are included in the datapoint labelled "unknown". These datapoints are discussed in detail later, if necessary, for the samples in question. The EDS cannot identify the oxidation state of iron. It is therefore not possible to chemically distinguish magnetite ($Fe^{3+}_2Fe^{2+}O_4$) from hematite ($Fe^{3+}_2O_3$). Thus, the term "iron oxide" is used in this thesis.

The separation of ilmenite and "iron oxide with titanium" will be used. Ilmenite are the grains with a high titanium content (Ti > 10 %). The iron oxide grains with traces of titanium, or a low titanium content (Ti < 10 %) are included in the "iron oxide" datapoint. Iron oxide with traces of chromium was also found and included in the "iron oxide" datapoint. Considerable amounts of magnesium were present in the iron oxide in the Vila Vila Formation. These grains were identified as magnesioferrite but are included in the "iron oxide" datapoint as well. The different types of iron oxides will later be discussed together with their representative samples, and figures will then illustrate how the "iron oxide" datapoint is divided into the different types.

Table 3: Semi-quantification of all heavy mineral fractions. Values are in percentage (%), except for number of heavy mineral grains which were analyzed per sample (last row). Samples sorted from old (left) and young (right) within each fraction column. ZRF = zircon fraction; APF = apatite fraction; MAG = magnetic fraction; CCE = Cancañiri FM (Formation); VV1 = Vila Vila FM; COPA1 = Copacabana FM; CH-D = Chutani FM; TQ7 = Tiquina FM.

Color code	Mineral	Zircon fractions					Apatite fractions					Magnetic fractions				
		ZRF1 CCE	ZRF3 VV1	ZRF4 COPA1	ZRF5 CH-D	ZRF5 TQ7	APF1 CCE	APF3 VV1	APF4 COPA1	APF5 CH-D	APF5 TQ7	MAG1.1 CCE	MAG3 VV1	MAG4 COPA1	MAG5 CH-D	MAG5 TQ7
	Zircon	40,31	48,43	59,00	83,67	28,14	7,84	4,40	5,83	0,52		9,12	5,20	12,08	4,41	2,46
	Rutile	26,70	44,88	30,50	6,12	13,77	9,41	15,38	5,00	0,52	1,46	32,85	11,56	42,08	0,44	3,55
	Pyrite	32,98					4,71					17,88				
	Barite		3,15	2,00		27,54		2,20	0,83		20,87		1,73			1,64
	Apatite-(F)		3,54	8,50	8,84	27,54	78,04	78,02	88,33	69,11	44,17	4,38	17,15	15,83	3,96	9,84
	Apatite-(Cl)				0,68	0,60				28,27	31,07			1,67	1,32	0,27
	Ilmenite					0,60										2,19
	Iron oxide					1,80				1,05	2,43	0,36	33,14	15,83	88,99	79,51
	Xenotime											0,36	2,50			
	Monazite												3,66	4,17		
	Chromite												0,19			0,55
	Ankerite												7,51	0,42		
	Tourmaline				0,68							21,53	14,26	7,92		
	Amphibole									0,52			1,16		0,44	
	Unknown											13,50	1,93		0,44	
	Total:	100,00	100,00	100,00	100,00	100,00	100,00	100,00	100,00	100,00	100,00	100,00	100,00	100,00	100,00	100,00
	Number of HM grains analyzed per sample	191	254	200	147	167	255	273	120	191	206	274	519	240	227	366

Zircon fractions (ZRF)

For the zircon fraction (Figure 13), the Tiquina Formation is the sample with the lowest percentage of zircon. Except for the Tiquina Formation, the younger the samples are, the higher the zircon content is. An opposite trend is seen regarding the rutile content, with exception of the Cancañiri Formation and the Tiquina Formation. The Vila Vila Formation has highest rutile percentage, then the Copacabana Formation, and then the Chutani Formation has a low rutile content. Tourmaline was only identified in one sample, of all the zircon fractions. This is the Chutani Formation zircon fraction, and only one tourmaline was present. The fluorapatite content increases from zero percentage in the oldest formation (Cancañiri Formation), to almost 28 % in the youngest formation (Tiquina Formation). Only the Chutani Formation, and the Tiquina Formation contain any chlorapatite in their zircon fractions. Barite was found in the zircon fraction for the Vila Vila Formation, the Copacabana Formation, and the Tiquina Formation. The Tiquina Formation has the highest barite content with almost 28 %. Iron oxide and ilmenite were only found in the zircon fraction for the Tiquina Formation. The Cancañiri Formation is the only formation with pyrite, and it contains almost 33 %.
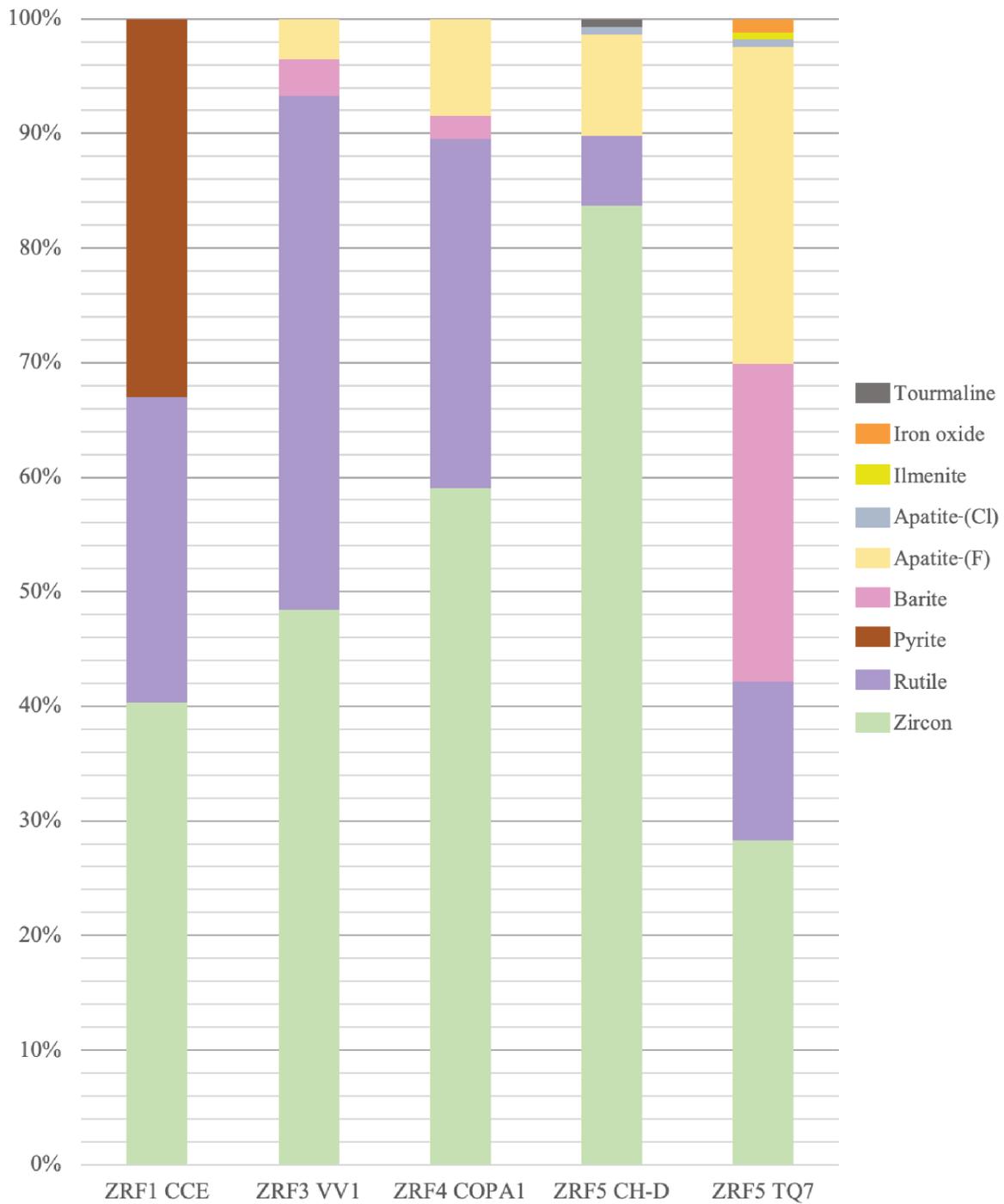
Figure 13: Heavy mineral quantification for all zircon fractions in this study. Samples sorted from old (left) to young (right). ZRF = zircon fraction; CCE = Cancañiri FM (Formation); VV1 = Vila Vila FM; COPA1 = Copacabana FM; CH-D = Chutani FM; TQ7 = Tiquina FM.

Apatite fractions (APF)

All samples have a high content of apatite in the apatite fraction (Figure 14). The highest content of apatite is found in the Chutani Formation, with around 69 % fluorapatite, and 28 % chlorapatite. Fluorapatite is most abundant in the Copacabana Formation, with 88 %. Chlorapatite was only identified in the youngest samples: the Chutani Formation (28 %) and the Tiquina Formation (31 %) and was absent in the older samples. Zircon was encountered in all samples except for the apatite fraction for the Tiquina Formation. The oldest sample (Cancañiri Formation) exhibit the highest zircon content (almost 8 %), and the Chutani Formation has the lowest zircon content (< 1 %). The Vila Vila Formation has the highest rutile content (15 %), and the Chutani Formation has the lowest content (< 1 %). The rutile content is higher in the three older samples than the two youngest. Pyrite was only found in the Cancañiri Formation, and amphibole was only encountered in the Chutani Formation. Barite is found in the Vila Vila, Copacabana, and Tiquina Formations. The Tiquina Formation has the highest content of barite, with almost 21 %. Iron oxide was identified in the two youngest samples.
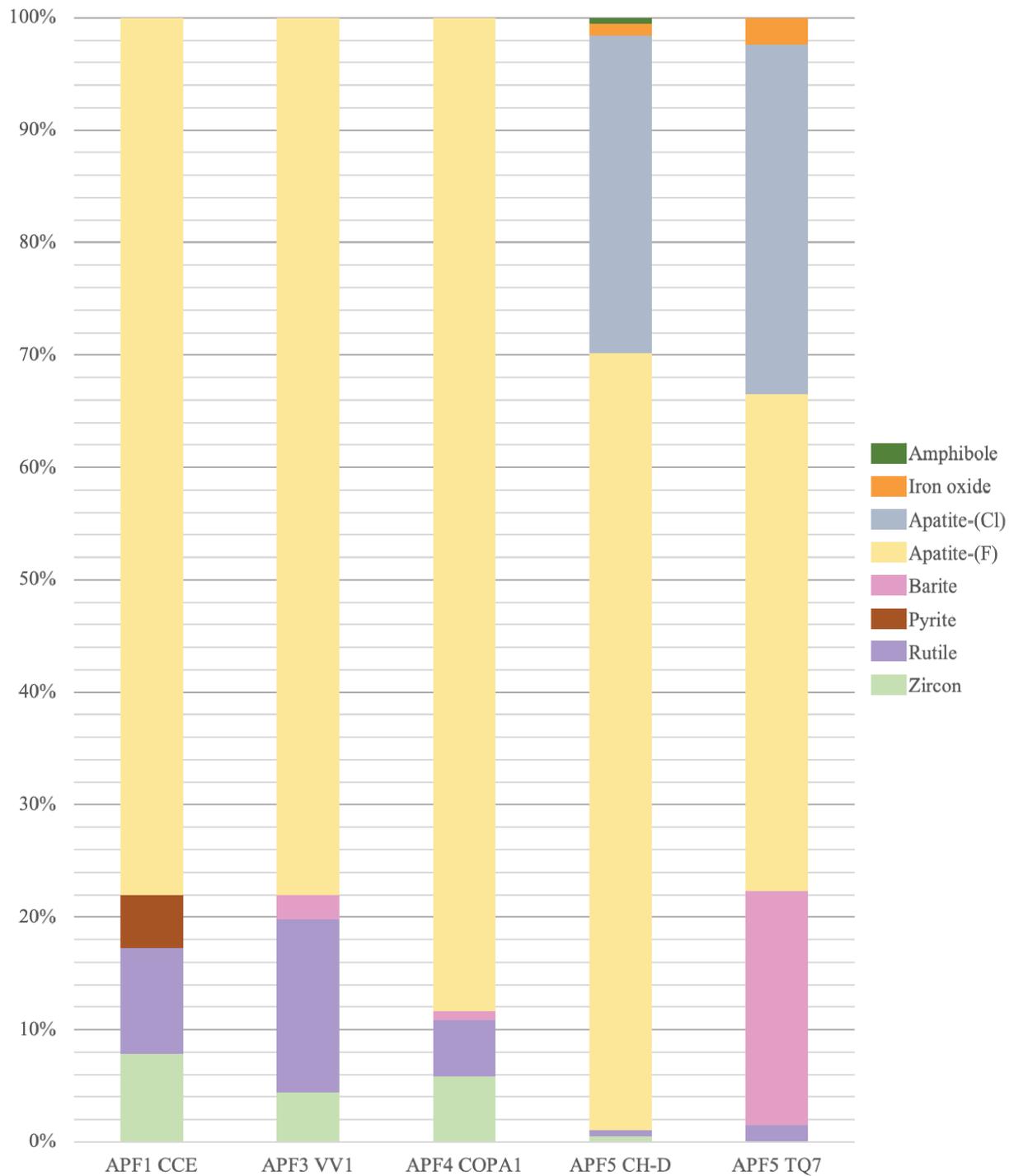
Figure 14: Heavy mineral quantification for all apatite fractions in this study. Samples sorted from old (left) to young (right). APF = apatite fraction; CCE = Cancañiri FM (Formation); VV1 = Vila Vila FM; COPA1 = Copacabana FM; CH-D = Chutani FM; TQ7 = Tiquina FM.

Magnetic fractions (MAG)

The magnetic fraction (Figure 15) is the most diverse fraction, with 14 identified minerals plus unknown minerals. It is also the fraction which displays the most variation between the different formations. The zircon content is generally low, with the lowest amount in the Tiquina Formation. The rutile content varies more, with high amounts in the Cancañiri Formation (33 %) and the Copacabana Formation (42 %). The Vila Vila Formation has around 11 % rutile, the Tiquina Formation has around 3 %, and the Chutani Formation contain less than 1 %. The tourmaline content is highest in the oldest sample and decreasing as the samples get younger. The Chutani Formation and Tiquina Formation has no tourmaline present in the magnetic fraction. The apatite content is highest in the Vila Vila Formation and the Copacabana Formation. All samples have fluorapatite in this fraction, but only the three youngest contain any chlorapatite. The iron oxide content is highest in the younger samples, with almost 89 % in the Chutani Formation. Nearly no iron oxide (< 1 %) was present in the Cancañiri Formation. The quantity of "unknown" is highest in the Cancañiri Formation (13 %), with one unknown mineral (later described as Unknown.CCE.A). The Vila Vila Formation has three unknown minerals, which gives a total of almost 2 % "unknown" in this sample. A small amount of "unknown" is also present in the Chutani Formation (< 1 %). Pyrite is again only identified in the Cancañiri Formation (18 %), while ilmenite was only found in the Tiquina Formation. Ankerite and monazite were both found in the Vila Vila Formation and the Copacabana Formation. Xenotime was encountered in the Cancañiri Formation and in the Vila Vila Formation. Amphibole was found in the Vila Vila Formation and the Chutani Formation. The Tiquina Formation and the Vila Vila Formation are the only ones with barite and chromite.
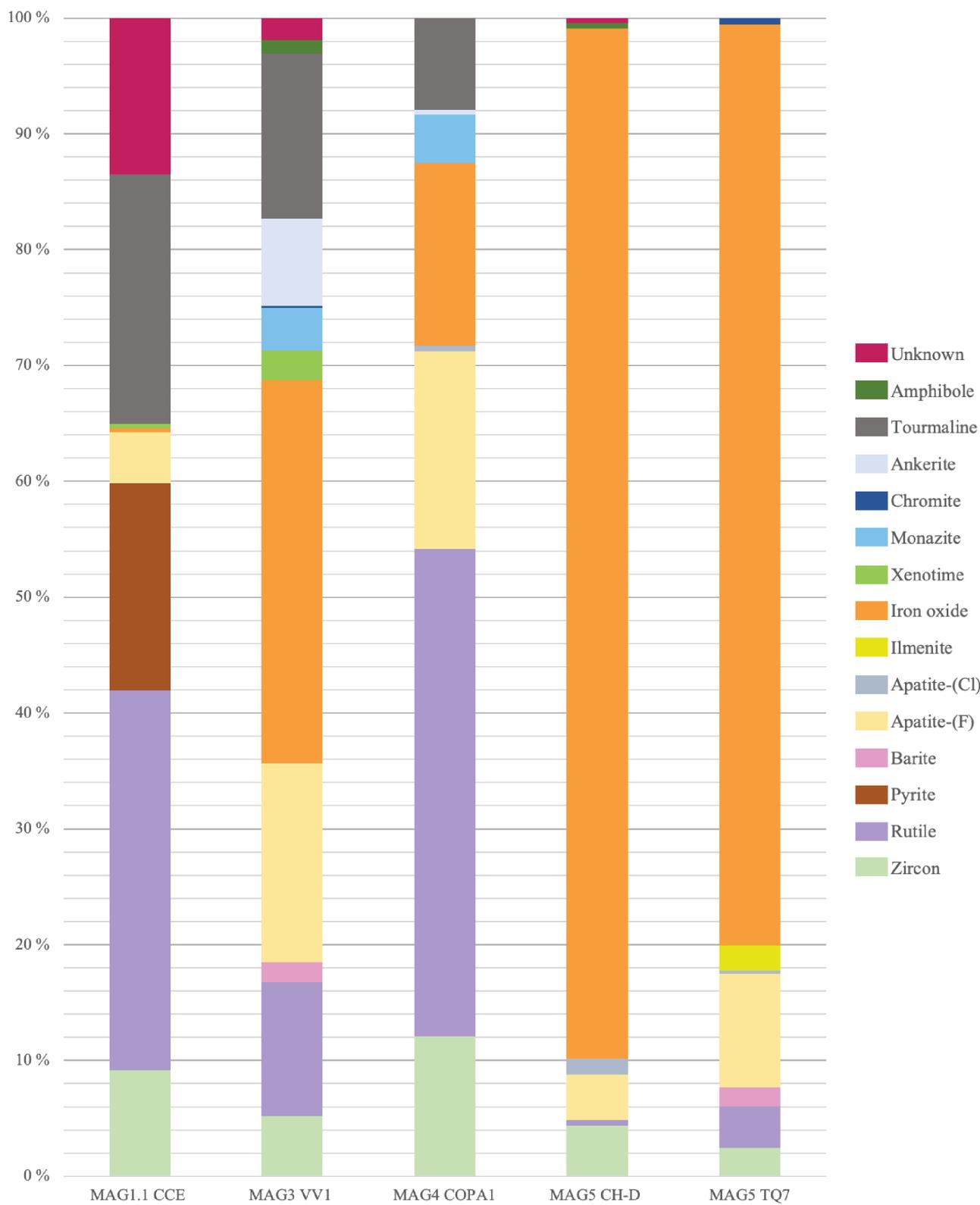
Figure 15: Heavy mineral quantification for all magnetic fractions in this study. Samples sorted from old (left) to young (right). MAG = magnetic fraction; CCE = Cancañiri FM (Formation); VV1 = Vila Vila FM; COPA1 = Copacabana FM; CH-D = Chutani FM; TQ7 = Tiquina FM.

3.1.1.1 Zircon fraction (ZRF1 CCE)

The zircon fraction of the Cancañiri Formation (ZRF1 CCE) only contains three minerals; zircon (~ 40 %), rutile (~ 27 %) and pyrite (~ 33 %) (Figure 16). The size ranges for each mineral in sample ZRF1 CCE are given in Table 4.
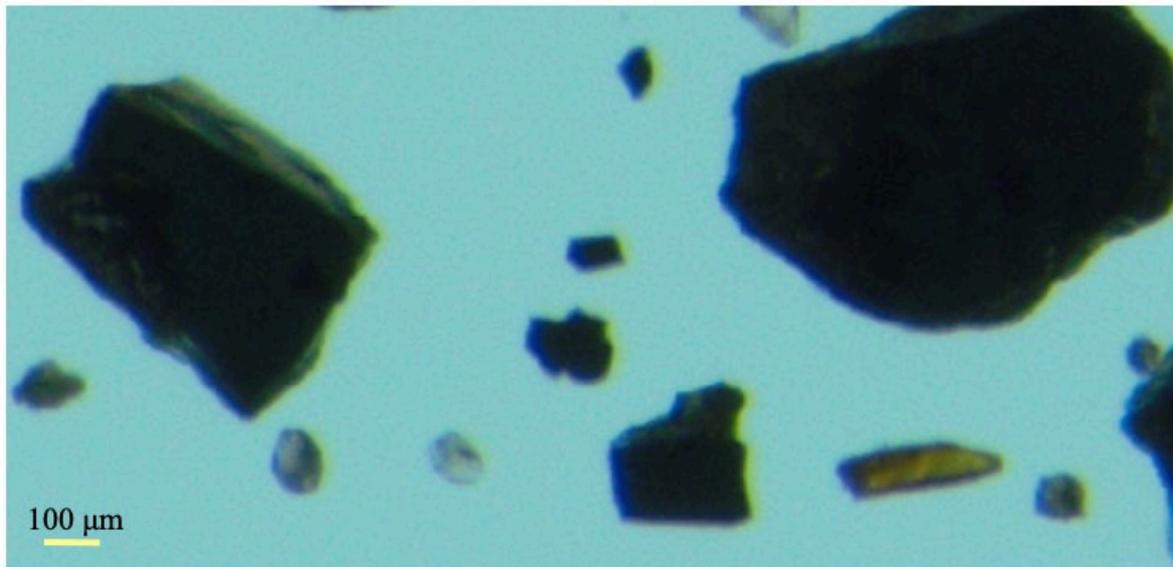
Figure 16: Example of an optical microscope image displaying the shape and color of the different minerals present in sample ZRF1 CCE. The zircons are well rounded, colorless to gray, with a high sphericity. The rutile grains exhibit the typical orange brown color of this sample. The darker grains are pyrite, with its typical cubic appearance.

Table 4: Size ranges (μm) for minerals in sample ZRF1 CCE.

Zircon	30-240
Rutile	30-200
Pyrite	60-380

Zircon

Of the zircons (Figure 17) in the Cancañiri Formation, most are well rounded (Figure 17A), with high sphericity, with only a few exceptions (Figure 17B). Some are sub-rounded (Figure 17C), and some are broken (Figure 17D). The zircons are colorless to a light grey color.
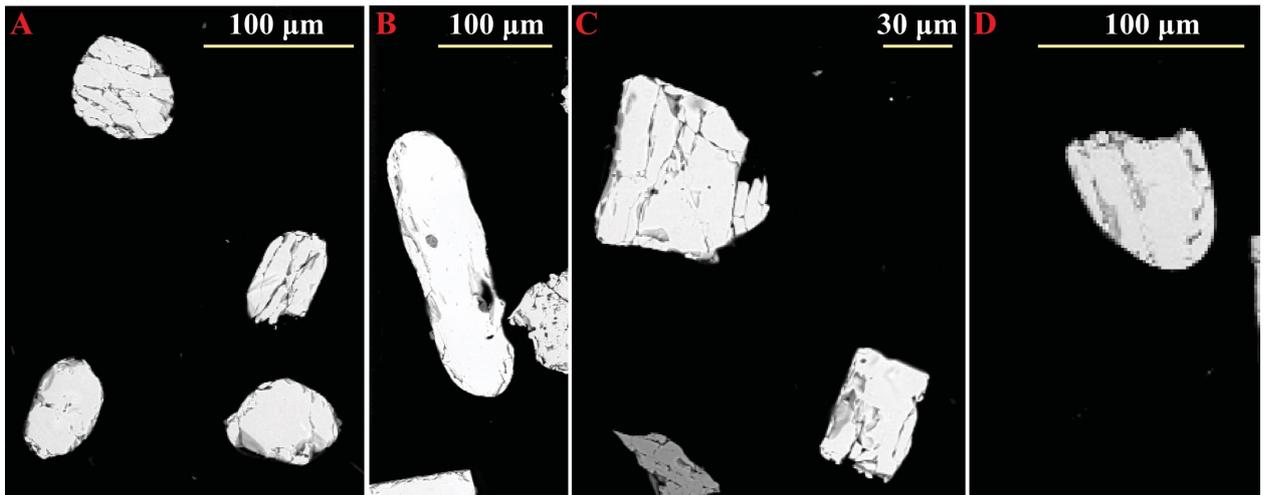
Figure 17: Zircons from the Cancañiri Formation. This sample contain mostly well-rounded grains, but some are sub-rounded (BSE image).

Rutile

The rutile grains in sample CCE, are mostly rounded to well-rounded and with a low sphericity (Figure 18). The color ranges from orange brown to dark brown and brownish/blackish grey. The detrital rutile grains are most often orange brown in color, and most of them appear to have a fragile or broken appearance. The authigenic rutile, which appear in relation to another mineral, most often quartz, is darker in color, grey to almost black.
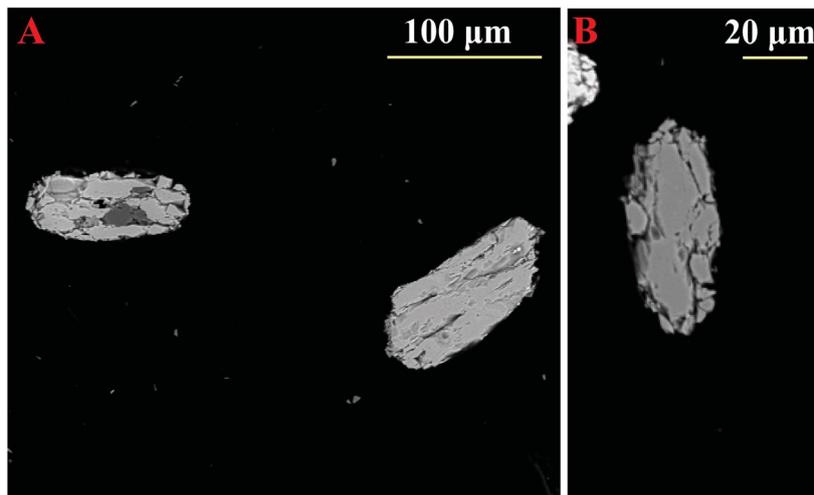
Figure 18: BSE image displaying the typical appearance of rutile grains in the Cancañiri sample.

Pyrite

Angular to sub-angular grains, some sub-rounded. Most have a high sphericity, but some are more elongated. Typical shapes can be seen in Figure 19. Note that the grains that are displayed in the BSE image do not display their actual shape, this is better seen in the inset image. This applies especially to the cubic pyrite crystal, and is due the polishing of the mount, as not all grains are polished sufficiently to express their true shape in the BSE image.
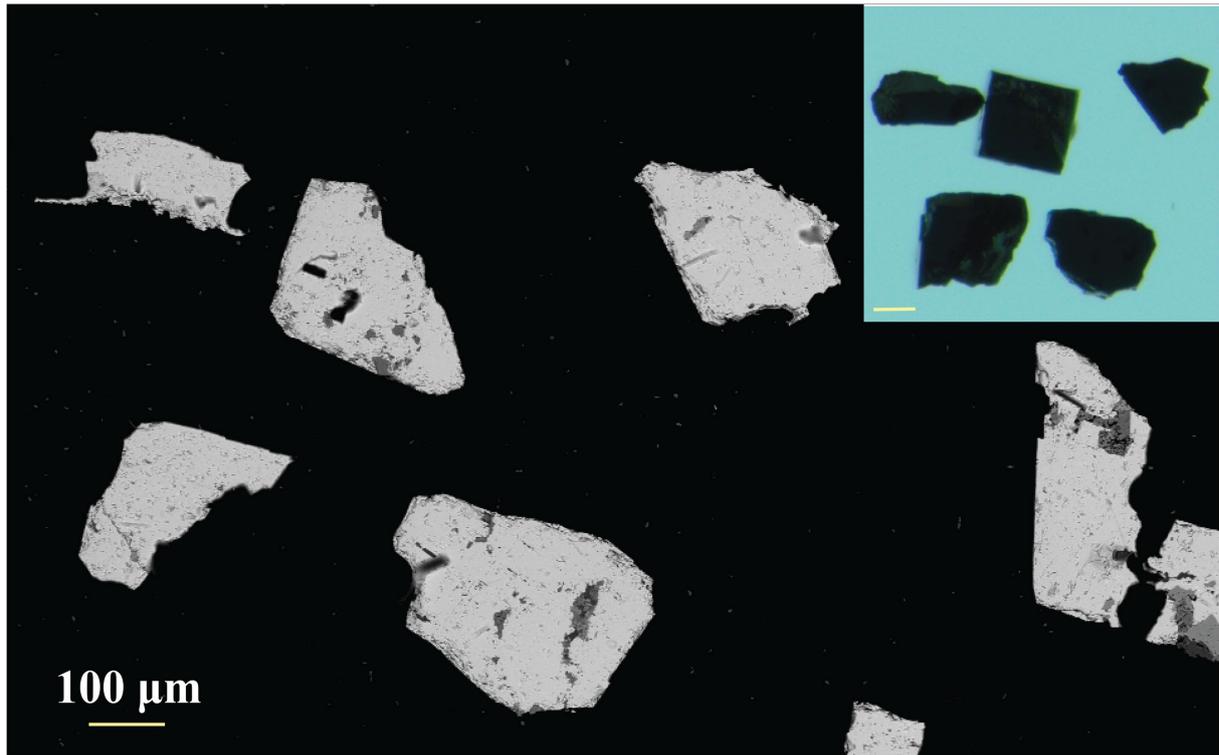
Figure 19: BSE image displaying pyrite grains in the Cancañiri sample. Inset image of the same pyrite grains, taken with an optical microscope (scalebar is 100 µm).

3.1.1.2 Apatite fraction (APF1 CCE)

The apatite fraction of the Cancañiri sample contains zircon (~ 8 %), rutile (~ 9 %), pyrite (~ 5 %) and fluorapatite (~ 78 %). No chlorapatite was identified in this sample. Size ranges for the different minerals in this sample are found in Table 5.

Table 5: Size ranges (µm) for minerals in sample APF1 CCE.

Zircon	40-120
Rutile	30-110
Pyrite	70-320
Apatite-(F)	40-195

Figure 20 presents an area of APF1 CCE. Note the difference in the shape of the grains from the BSE image to the optical microscopy image (inset image). The optical microscopy image clearly exhibits well-rounded grains with a high sphericity, while the BSE image displays grains which are not as rounded. It is thus important to consult both types of images when determining the shape of the grains.
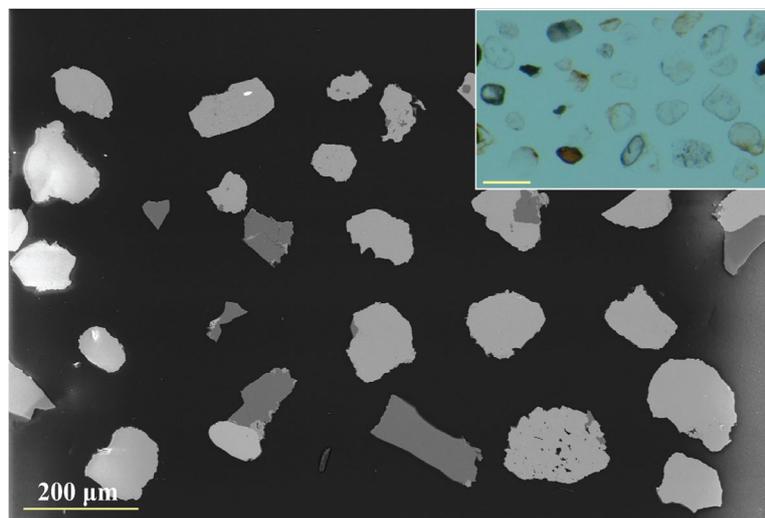
Figure 20: BSE image with different mineral grains in APF1 CCE. Inset of optical microscopy image, scalebar of inset image is 200 µm.

Apatite-(F)

The apatite grains present in APF1 CCE, are only fluorapatites (apatite-(F)). The Cancañiri sample does not contain any chlorapatites (apatite-(Cl)). The fluorapatites are well-rounded, with a high sphericity (Figure 21). Chemically these fluorapatites are very clean and does not exhibit any chlorine in their EDS spectrums. Traces of silica are seen in some spectrums.
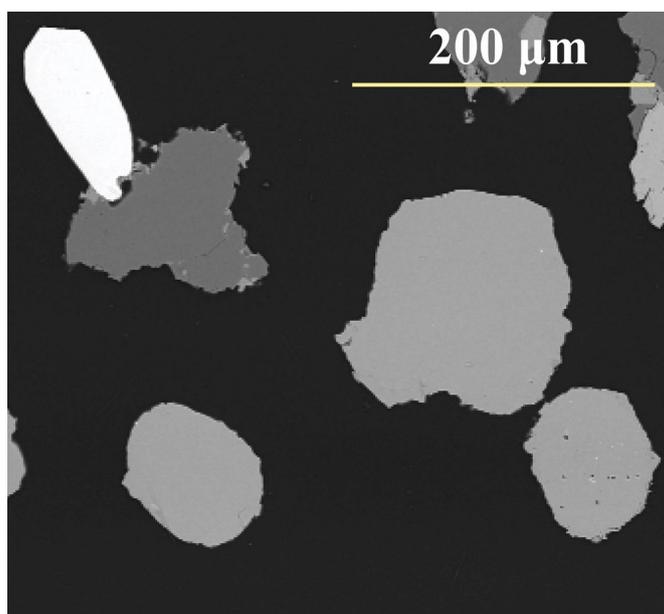
Figure 21: BSE image exhibiting the typical appearance of apatite-(F) in APF1 CCE. The fluorapatites are the light grey, well-rounded grains in the lower part of the image. A well-rounded zircon is visible in the upper left corner in relation with a light mineral (probably quartz).

Other minerals

The rutile grains in the apatite fraction appear mostly as authigenic rutile, in relation to quartz, not as detrital grains, such as it occurred in the zircon fraction of the sample. Other than rutile grains, there are also some zircon grains and some pyrite grains. Both minerals have the same appearance in this fraction as they do in the zircon fraction of the sample.

3.1.1.3 Magnetic fraction (MAG1.1 CCE)

The magnetic fraction of the Cancañiri sample contains iron oxide (< 1 %), xenotime (< 1 %), tourmaline (~ 22 %) and an unknown mineral (~ 14 %), in addition to zircon (~ 9 %), rutile (~ 33 %), pyrite (~ 18 %) and fluorapatite (~ 4 %). The size ranges for minerals in the magnetic fraction (MAG1.1 CCE) are given in Table 6. For the tourmalines, most are 100-300 μm (one is lower, thus the 60-300 range). For the unknown, all but one are 100-290 μm.

Table 6: Size ranges (μm) for each mineral present in sample MAG1.1 CCE.

Zircon	40-185
Rutile	35-200
Pyrite	40-540
Apatite-(F)	25-175
Iron oxide	430
Xenotime	60
Tourmaline	60-300
Unknown	50-290

Tourmaline

The tourmalines in sample MAG1.1 CCE, display varying shapes and colors (Figure 22A), but most are well-rounded. They all have similar chemistry. The EDS at UiS cannot measure and display the amount of boron (B) present in tourmaline. The chemical compositions of tourmalines and amphiboles are often similar, especially considering that boron, which is only in tourmalines, is not possible to determine here. Amphiboles usually display distinct cleavages in the crystals, which does not appear in the grains in this sample. It is thus more likely, also considering the amount of grains, that they are different types of tourmalines, rather than amphiboles.

The identifying character of tourmalines is the lack of cleavage. The grains may have different shapes, mostly tourmalines may be rounded while amphiboles are easy to weather and alter (Andò et al., 2014). However, when the amphiboles are not strongly affected by transport and diagenetic processes the distinction is very complex.

The most characteristic color for the tourmalines, is displayed in Figure 22B and C. These all have similar chemistry, but varying shape. Some of the tourmalines contain calcium, most do not. The iron content is also varying slightly. The tourmalines with calcium or higher iron content have varying colors, and are not of the characteristic color as in Figure 22B and C.

Chemically the tourmalines are rather similar to each other, but some of them have traces of calcium and titanium.
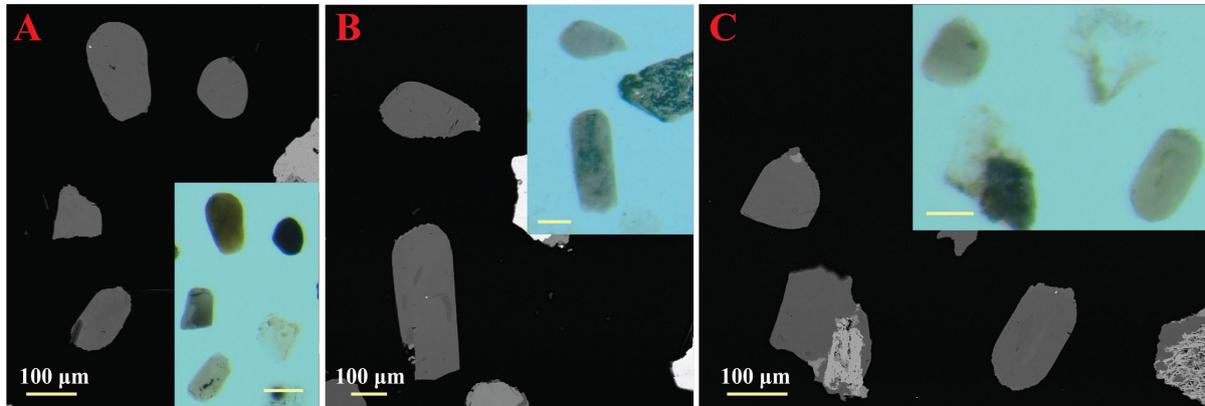
Figure 22: Tourmalines in sample MAG1.1 CCE. A) tourmalines with varying colors and shapes (grain just above scale in inset image is not tourmaline); B) and C) typical colors and shapes for tourmaline in this sample. BSE images with inset images of optical microscopy images. All scales are 100 μm.

Unknown

There is one unknown mineral present in this sample (13,5 %). It resembles a sheet silicate in habit, but it is colorless to yellow, and transparent (Figure 23). The chemistry (Appendix A, Unknown.CCE.A) resembles the chemistry of the chlorite group, with magnesium, aluminum, silica and considerable amounts of iron. Normally minerals of the chlorite group are various shades of green or blue (Mange and Maurer, 1992), but can in rare cases be colorless. To determine which mineral this is, a microprobe analysis or perhaps an X-ray diffraction analysis could be helpful but was not possible to perform due to time constraints and access impossibility of these analytical techniques caused by the Corona crisis.
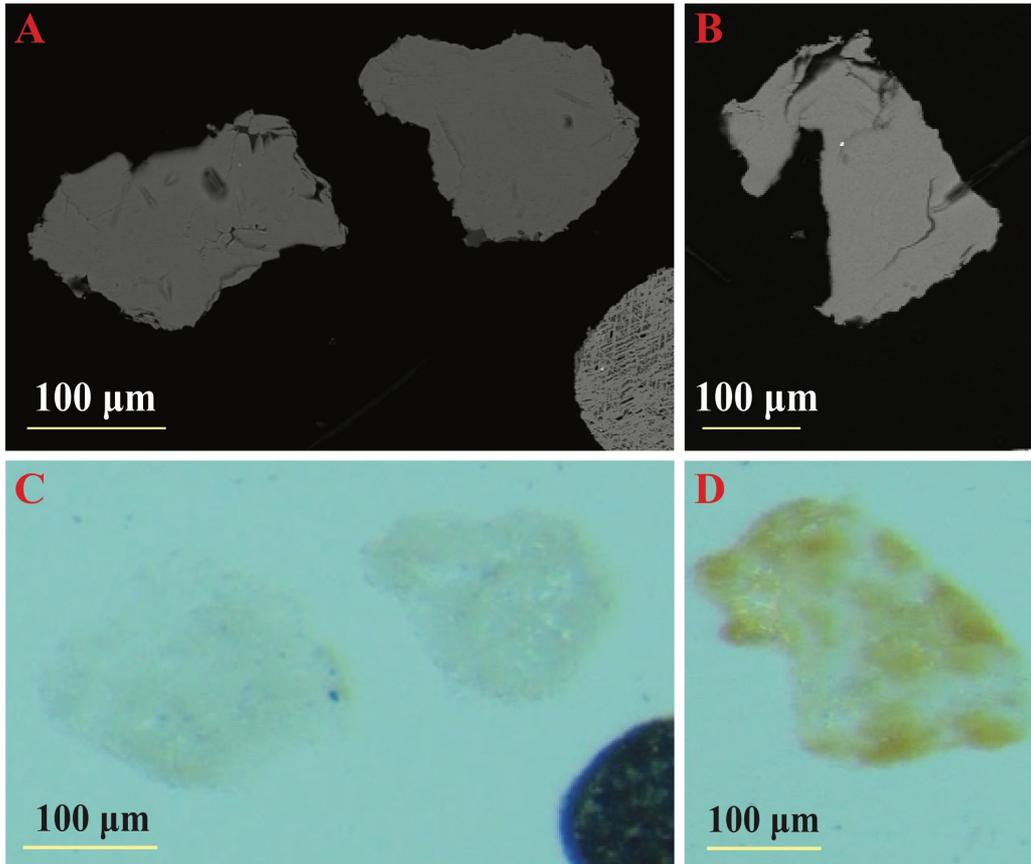
Figure 23: A and B are BSE images of the unknown mineral in MAG1.1 CCE. C and D are optical microscopy images of the same grains as in A and B. These all have the same chemistry.

Other minerals

Zircon, rutile, pyrite and fluorapatite were also found. Xenotime was encountered once, as well as iron oxide. The iron oxide has traces of aluminum.

3.1.2.1 Zircon fraction (ZRF3 VV1)

This sample contains zircon (~ 48 %), rutile (~ 45 %), barite (~ 3 %) and fluorapatite (~ 4 %). Size ranges for the different minerals in ZRF3 VV1 are presented in Table 7.

Table 7: Size ranges (µm) for each mineral present in sample ZRF3 VV1.

Zircon	30-130
Rutile	30-135
Barite	50-190
Apatite-(F)	40-120

Zircon

The zircon grains in sample ZRF3 VV1 range from well-rounded to angular (Figure 24A to E). Some zircon grains are euhedral crystals (Figure 24C to E), with zoning clearly visible even in the BSE images, but especially in the CL images. The euhedral crystals range from angular to rounded, but they are mainly of low sphericity. Of all the zircons, most are of low sphericity, but some also have higher sphericity (Figure 24A). There appear to be more broken zircons in the Vila Vila Formation than in the Cancañiri Formation. The zircons are mainly colorless to steel grey, but some brown grains were also observed, which were initially mistaken for rutile.
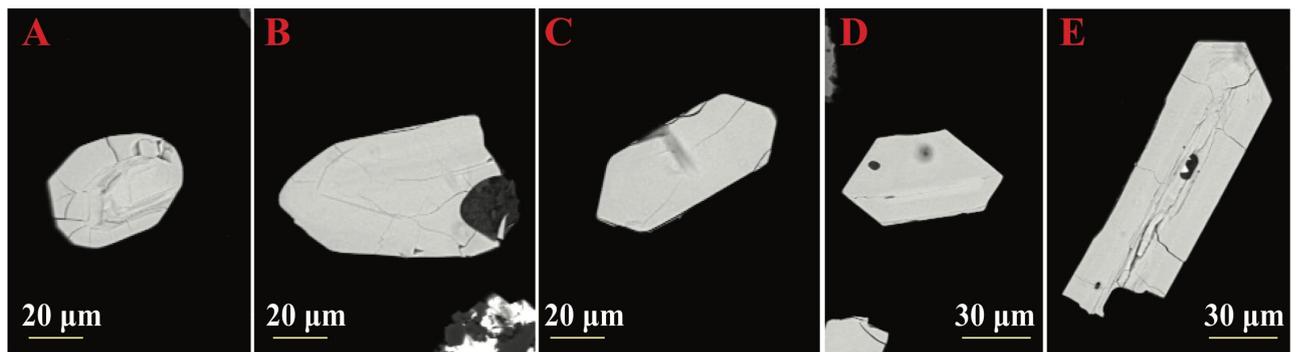
Figure 24: Different zircons from the Vila Vila Formation (ZRF3 VV1). Well-rounded to angular with varying sphericity. Zoning visible in Figure A and E. The zircon in B is clearly broken but still display some of the original crystal habit. The euhedral crystal habit is clearly seen in Figure C to E.

Rutile

The rutile grains have two different occurrences; either they are detrital yellowish brown to brown and transparent grains, or they are authigenic black and opaque, replacing lighter minerals. The brown grains range from well-rounded to angular (Figure 25). The authigenic rutile can be seen replacing lighter minerals, quartz and feldspar, and vary thus in shape. Some exhibit nice "needle-like" crystals probably growing along the cleavages of the original grain.
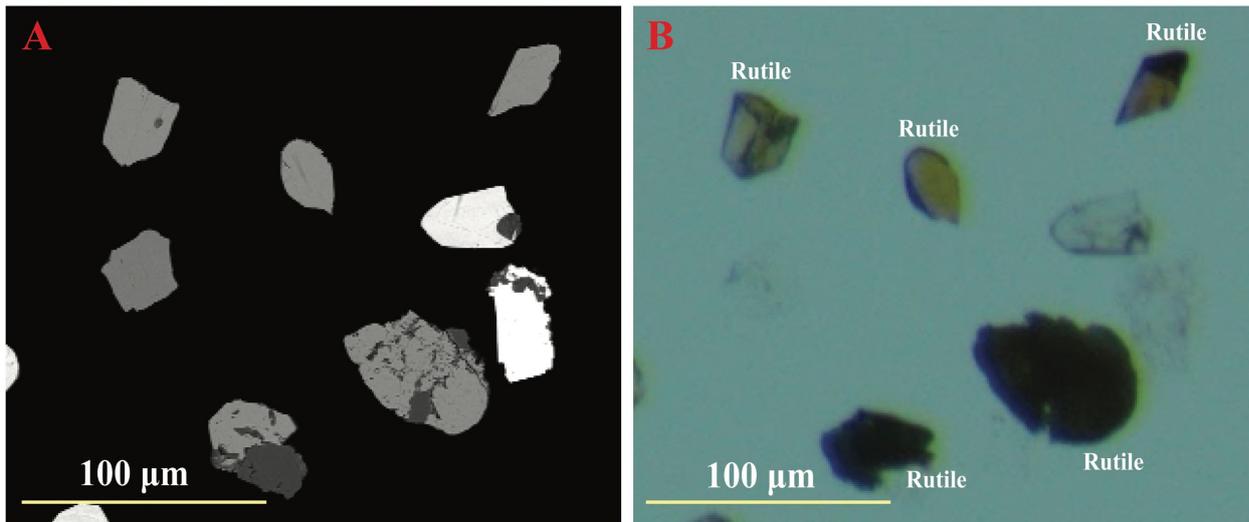
Figure 25: A) BSE image; B) optical microscopy image of rutile in ZRF3 VV1. Note the different shapes of the brown detrital rutile, as well as the appearance of the opaque, authigenic, rutile. The brighter grains in the BSE image are zircon (above) and barite (below).

Other minerals

ZRF3 VV1 also contain barite and a small amount of fluorapatite. The barite is replacing light minerals and have varying shape. In most of the barite grains, there are traces of strontium present. The fluorapatites are sub-angular to sub-rounded. The EDS analysis indicate that the fluorapatites have mainly fluorine and not chlorine, but some have traces of chlorine as well.

3.1.2.2 Apatite fraction (APF3 VV1)

The apatite fraction for Vila Vila Formation contains zircon (~ 4 %), rutile (~ 15 %), barite (~ 2 %) and fluorapatite (~ 78 %). Size ranges for the minerals can be seen in Table 8.

Table 8: Size ranges (µm) for the different minerals in APF3 VV1.

Zircon	40-155
Rutile	50-185
Barite	40-80
Apatite-(F)	45-105

Apatite-(F)

Fluorapatite is the only type of apatite in APF3 VV1. The fluorapatites are angular (Figure 26A) to well-rounded (Figure 26B). These have traces of silica. Some fluorapatites have chlorite traces, but mostly they only contain fluorine.
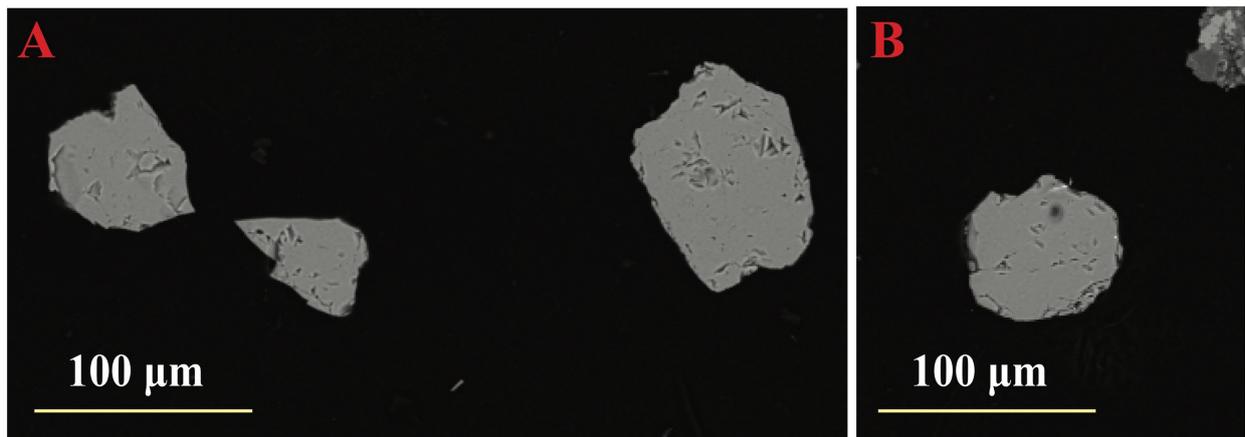
Figure 26: Angular to well-rounded fluorapatites in APF3 VV1. The two grains to the left in A are noticeably angular compared to the well-rounded grain in B.

Other minerals

There are also zircon, rutile and barite in this sample. The rutile occurs as mostly authigenic, replacing lighter minerals. This is also the case with barite. Zircon grains are angular to rounded, with varying sphericity.

3.1.2.3 Magnetic fraction (MAG3 VV1)

This sample is the most diverse sample of all and contains 11 different minerals plus unknown minerals: zircon (~ 5 %), rutile (~ 12 %), barite (~ 2 %), fluorapatite (~ 17 %), iron oxide (~ 33 %), xenotime (~ 3 %), monazite (~ 4 %), chromite (< 1 %), ankerite (~ 8 %), tourmaline (~ 14 %), amphibole (~ 1 %), and different unknown (~ 2 %) minerals. Size ranges for all 11 minerals are listed in Table 9.

Table 9: Size ranges (µm) for the different minerals in MAG3 VV1.

Zircon	30-70
Rutile	20-150
Barite	70-155
Apatite-(F)	30-125
Iron oxide	30-210
Xenotime	30-50
Monazite	20-100
Chromite	40
Ankerite	65-465
Tourmaline	30-160
Amphibole	100-270
Unknown	50-375

Iron oxide

There are two types of iron oxide present in sample MAG3 VV1. Regular iron oxide containing iron and oxygen, and traces of magnesium, and sometimes manganese and silica. The second is an iron oxide with considerable amounts of magnesium. The magnesium rich iron oxide is called magnesioferrite. For the purpose of the previous figures, magnesioferrite has been included in the "iron oxide" datapoint. How the "iron oxide" for MAG3 VV1 is divided see Figure 27.
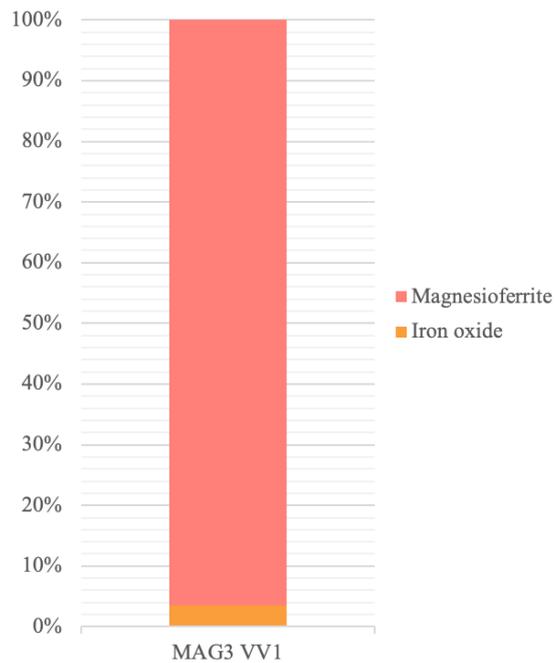
Figure 27: Amount of magnesioferrite and iron oxide in MAG3 VV1. The total of this is called "iron oxide" in previous figures.

The magnesioferrite grains vary from angular to sub-rounded (Figure 28A) and are yellowish to brown in color. The lighter colored grains are transparent while the brown grains are almost opaque (Figure 28B). These grains vary from 30 to 210 μm, while the iron oxide with traces of magnesium are 40-150 μm. The magnesioferrite also has traces of silica, calcium, manganese, and sometimes aluminum or potassium.
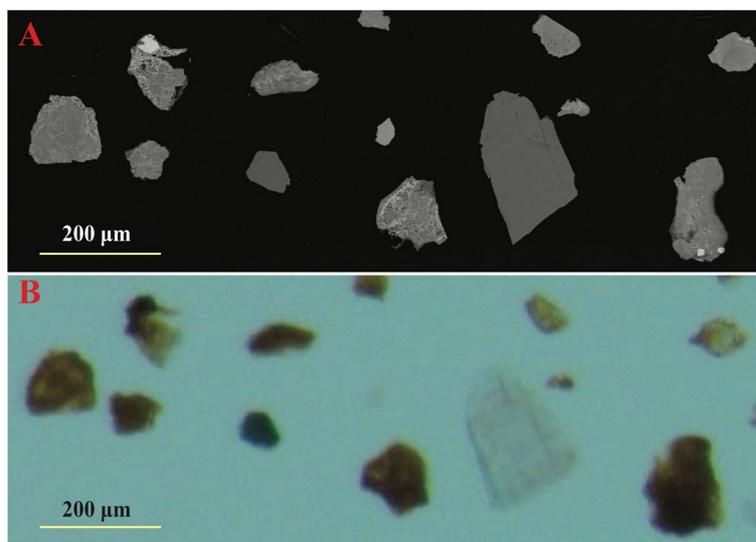
Figure 28: The yellowish to brown grains are magnesioferrite. A) BSE image; B) optical microscope image.

Xenotime-(Y)

Chemically the xenotime grains contain phosphorus (P) and yttrium (Y), and in this sample, also small amounts of rare earth elements (REE). Examples of xenotime grains are seen in Figure 29. The shape of the grains vary, but a hint of the original habit of the crystal is still seen in the xenotime grain in Figure 29A. Xenotime grains appear mainly as colorless to grey, but some grains are black (Figure 29A). The black color could be due to impurities.
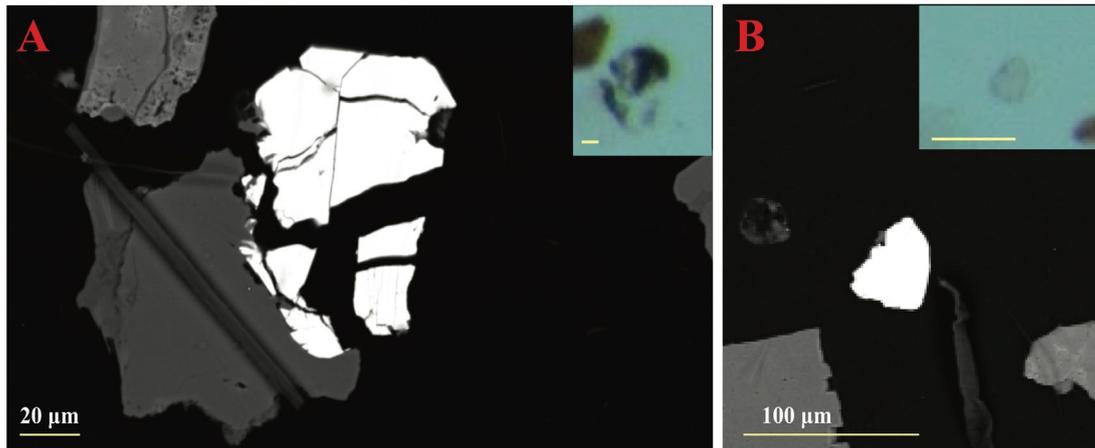
Figure 29: Xenotime in sample MAG3 VV1. BSE images with insets of optical microscopy images. A) scale in inset photo is 20 μm; B) scale in inset photo is 100 μm.

Monazite-(Ce)

These monazite grains contain different REE. In MAG3 VV1, the monazites are all monazite-(Ce), which means they have an abundance of cerium (Ce). Lanthanum (La) and neodymium (Nd) are replacing cerium. There are also traces of thorium (Th) and calcium (Ca) in these grains. The grains are well-rounded and colorless (Figure 30).
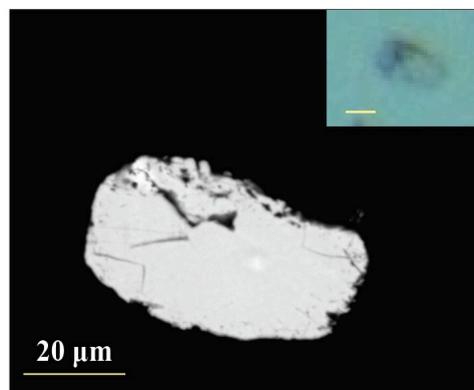
Figure 30: Monazite grain from MAG3 VV1. BSE image with optical microscope image as inset. The scalebar in the inset image is 20 μm.

56

Tourmaline

Light greenish grey to light brown and green tourmalines with varying shapes are present in this sample. The greenish grey tourmalines are most typical (Figure 31). The typical shape is seen in Figure 31A to C: short and stubby prismatic crystals with one flat/broken end and one end with termination. Figure 31D could be a crystal which was glued and cut across the length, thus exhibiting the hexagonal shape of the crystal. The tourmalines range from sub-angular to rounded. The EDS analysis indicate that some grains have traces of titanium or calcium.
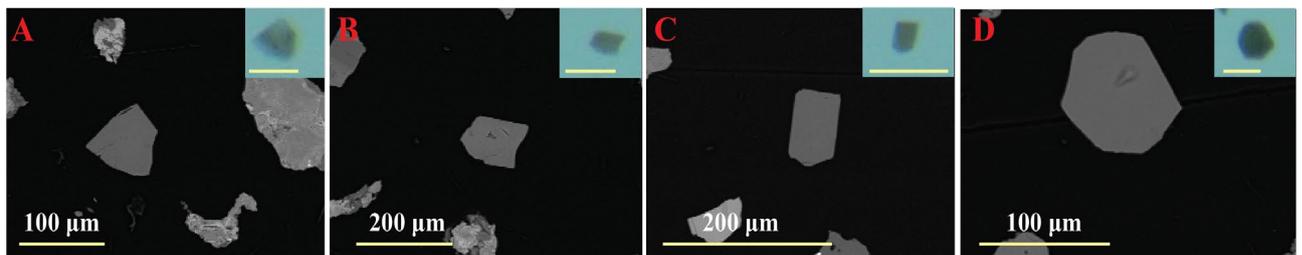
Figure 31: Typical tourmalines of the Vila Vila Formation sample. BSE images with inset of optical microscope image. A) scale of inset image is 100 μm; B) and C) scale of inset images are 200 μm; D) scale of inset image is 100 μm.

Ankerite

Transparent colorless to light grey mineral, with rhombohedral crystal habits visible in most grains (Figure 32).
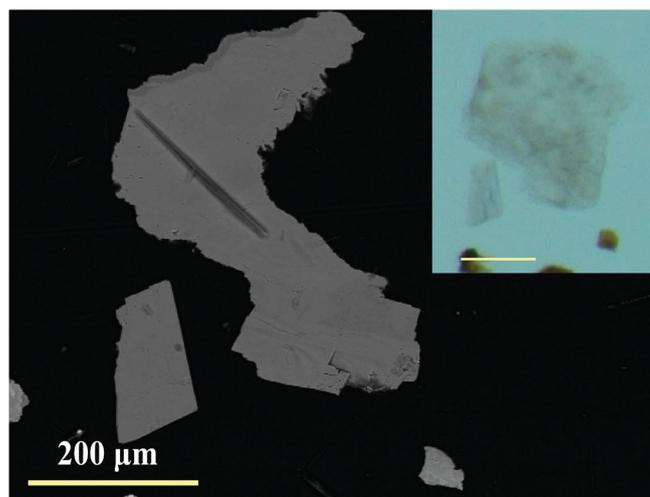
Figure 32: Ankerite in sample MAG3 VV1. BSE image with inset of optical microscopy image. Scale in inset image is 200 μm.

Amphibole

There are some grains of greyish green to dark green coloring, with chemistry resembling amphibole (hornblende). These have varying shapes and sizes, but the larger ones are the ones with dark green coloring (Figure 33).
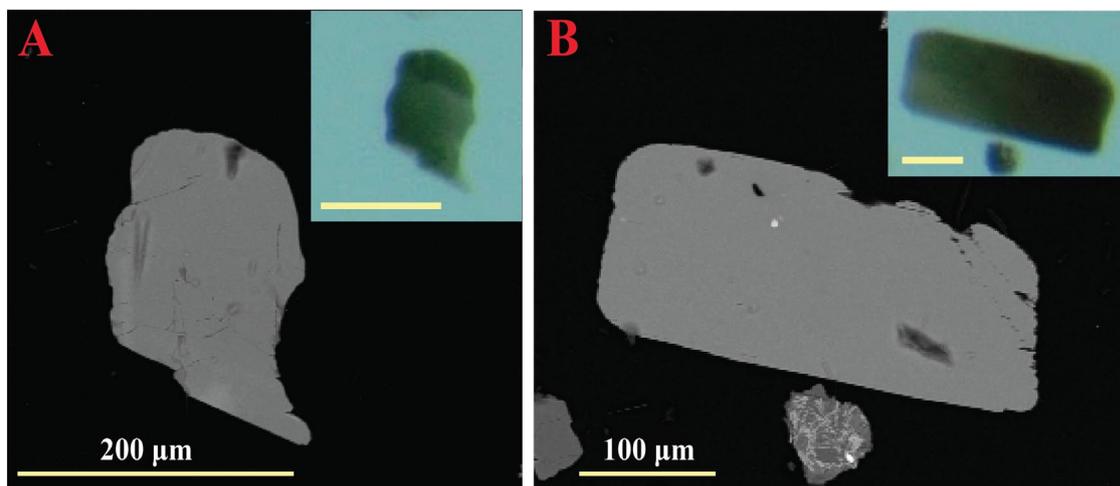
Figure 33: Dark green amphiboles from MAG3 VV1. BSE images with inset of optical microscope image. A) scale of inset image is 200 μm; B) scale of inset image is 100 μm.

Unknown

There are still some unknown minerals in this sample. Three different minerals were found, which were not possible to identify based on their chemistry. These are named "unknown.VV1.A-C" (Appendix A).

Unknown.VV1.A is a colorless mineral. This mineral appears as well-rounded grains, either with high sphericity of elongated (Figure 34). The chemistry indicates magnesium, silica, calcium, iron and oxygen. The magnesium content is relatively high. The size range for this mineral is 55-375 μm. These grains may belong to the group of chain and/or double-chain silicates.
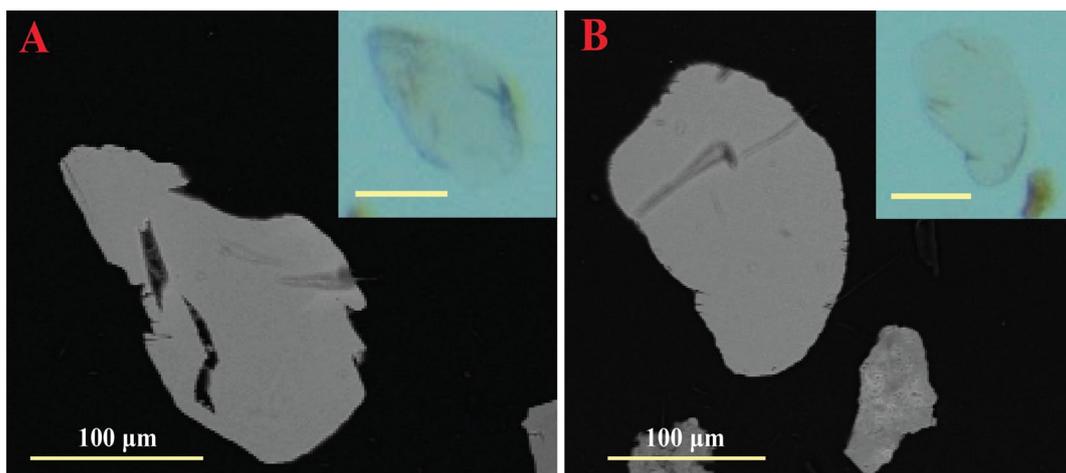
Figure 34: Unknown mineral in MAG3 VV1 (Unknown.VV1.A). BSE images with inset of optical microscope image. Scale of inset images are 100 μm.

Unknown.VV1.B contains only magnesium, silica, iron and oxygen. Only two grains were measured of this mineral. The chemistry resembles unknown.VV1.A, but it does not contain any calcium. One grain (80 μm) is colorless, elongated and angular, and the other (45 μm) has a yellowish-brown tint and is more rounded. The chemistry of the colored grain indicates traces of aluminum.

Unknown.VV1.C is the last unknown mineral in this sample. Chemically, it contains the same elements as unknown.VV1.A, but the amount of calcium is a lot higher, and iron is only present in a small amount. Only one grain (225 μm) was measured, and it is an elongated, sub-rounded grain.

Other minerals

There is also rutile, fluorapatite and barite, as well as one chromite grain in the magnetic fraction of VV1. The barite occurs as authigenic and is replacing light minerals. It looks like the barite in ZRF3 VV1 (Figure 25), some grains also contain strontium, as in the other fractions. The fluorapatite is similar to the fluorapatite in the apatite fraction, but in this fraction, traces of manganese were seen as well.

To determine those few minerals exactly, the best methods would be either RAMAN spectroscopy or electron microprobe analysis, both not available during this thesis. The chemical abundances per element within a SEM-EDS analysis are not always strictly quantitative.

3.1.3.1 Zircon fraction (ZRF4 COPA1)

This sample contain zircon (59 %), rutile (~ 31 %), barite (2 %), and fluorapatite (~ 9 %). Table 10 presents the size ranges of the different minerals in this sample.

Table 10: Size ranges (µm) for each mineral present in sample ZRF4 COPA1.

Zircon	30-215
Rutile	25-165
Barite	70-200
Apatite-(F)	25-170

Zircon

These are mainly angular (top and bottom zircon in Figure 35A) to sub-rounded (bottom zircon in Figure 35B) grains with low sphericity, many are euhedral crystals. Some are also well-rounded and with high sphericity (the middle grain in Figure 35A). Another common shape is one that resemble an arrowhead, as in the topmost zircon in Figure 35A. What is worth noting in this sample is that the zircons more often contain inclusions, some of considerable size. The ones which were studied were quartz and fluorapatite inclusions. A lot of the zircon grains are fractured as the zircon to the right in Figure 35B.
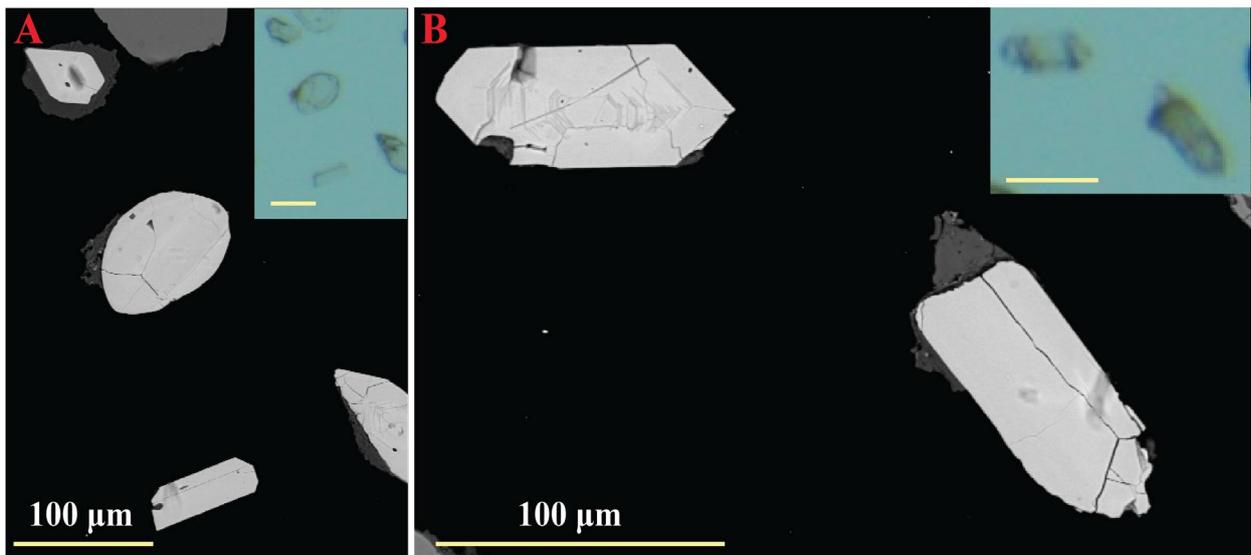
Figure 35: Zircons from ZRF COPA1. BSE images with optical microscopy images as insets. A) scale of inset image is 100 µm; B) scale of inset image is 100 µm.

Rutile

The rutile grains in the Copacabana Formation samples appear either as detrital grains of brown rutile, or authigenic black rutile which is replacing/growing on lighter minerals, such as quartz. The rutile grains are very similar to the one seen in the samples from the Vila Vila Formation. The brown detrital rutile grains are sub-rounded to well-rounded and vary from low to high sphericity. Some of the rutile grains have a small percentage of iron, but it is not enough iron (Fe << 10 %) to call it ilmenite. These rutile-(Fe) are included in the "rutile" datapoint in previous figures. Other than iron, there are also traces of quartz present in some of the rutile grains.

Other minerals

There are also fluorapatite and some barite in the zircon fraction of COPA1. The fluorapatites have both fluorine and chlorine and some also have traces of silica. The barite grains contain traces strontium.

3.1.3.2 Apatite fraction (APF4 COPA1)

The apatite fraction for the Copacabana Formation contain zircon (~ 6 %), rutile (5 %), barite (< 1 %), and fluorapatite (~ 88 %). Size ranges for these minerals are given in Table 11.

Table 11: Size ranges (µm) for all minerals present in sample APF4 COPA1.

Zircon	40-100
Rutile	50-200
Barite	100
Apatite-(F)	50-180

Apatite-(F)

Most of the fluorapatites are well-rounded grains with high sphericity, some have low sphericity and appear as elongated prisms. There are still some that are angular, but these appear to be broken and thus are angular in one end and well-rounded in the other end. Chemically there appear to be some sodium in the apatite grains, as well as magnesium and silica. Largely the fluorapatites are colorless and transparent, but some have yellowish to grey coloring.

Other minerals

In the apatite fraction there are also zircon, rutile and barite.

3.1.3.3 Magnetic fraction (MAG4 COPA1)

This fraction is dominated by rutile (~ 42 %). It also contains zircon (~ 12 %), fluorapatite (~ 16 %), chlorapatite (~ 2 %), iron oxide (~ 16 %), monazite (~ 4 %), ankerite (< 1 %), and tourmaline (~ 8 %). Size ranges for these minerals are given in Table 12.

Table 12: Size ranges (µm) for all minerals present in sample MAG4 COPA1.

Zircon	45-160
Rutile	25-170
Apatite-(F)	60-230
Apatite-(Cl)	70
Iron oxide	45-180
Monazite	40-180
Ankerite	105
Tourmaline	50-215

Iron oxide

The iron oxides appear as black, opaque grains in the optical microscope. In the BSE images, different shapes were observed (Figure 36). In Figure 36A and B, the iron oxide appears to be growing on another grain or replacing another mineral. Sometimes traces of magnesium, silica or aluminum are seen in the EDS analysis.
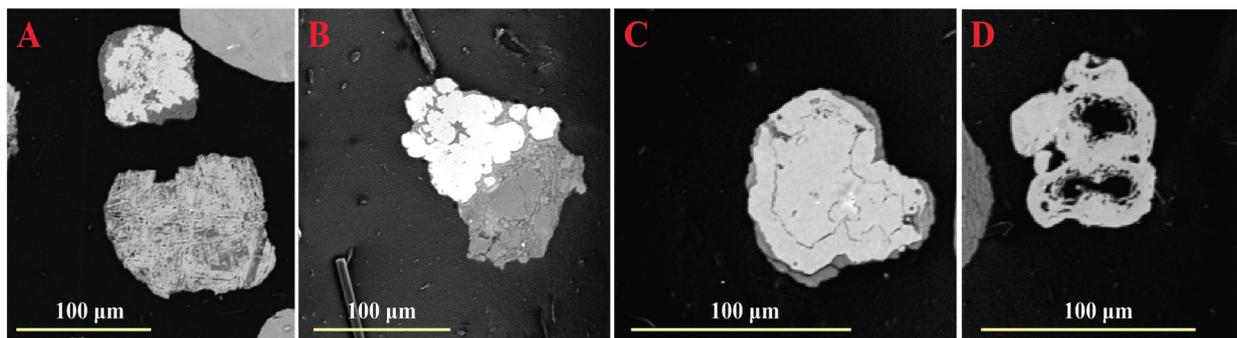
Figure 36: Demonstrating the occurrence of iron oxide in minerals of the magnetic fraction within the Copacabana Formations sample (BSE images).

Monazite-(Ce)

These are well-rounded grains with high sphericity. These are dominantly colorless (Figure 37A), but also range from pale yellow (Figure 37B), to brown (Figure 37C).
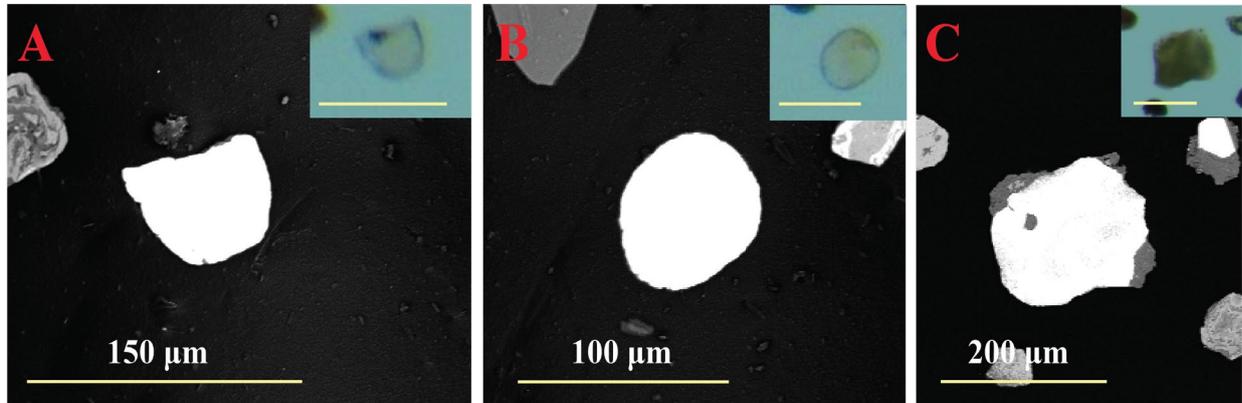
Figure 37: Monazite grains in MAG4 COPA1. BSE images with inset of optical microscopy images. A) scale of inset image is 150 μm; B) scale of inset image is 100 μm; C) scale of inset image is 200 μm.

Tourmaline

Greenish grey to green tourmalines appear in MAG4 COPA1 (Figure 38). There are some opaque black grains present as well, but the greenish grey to green color is by far dominant. The shape of the tourmaline varies, but many have stubby prismatic habits, with terminations in one (Figure 38A) or both (Figure 38C) ends. The tourmalines are rounded to well-rounded.
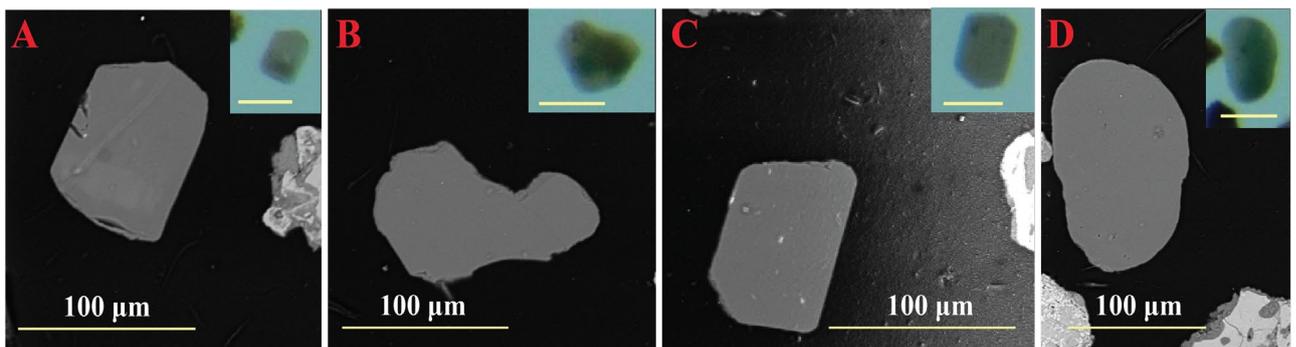
Figure 38: Tourmalines in MAG3 COPA1. BSE images with inset of optical microscopy images (scale in inset images are all 100 μm).

Other minerals

There are also some ankerite grains and chlorapatite grains in this fraction, as well as zircons, rutile grains and fluorapatites. The rutile grains appears mostly as opaque, authigenic rutile and

in the BSE images, it is seen to be replacing or growing on lighter minerals, like the iron oxide (Figure 36A). Of the rutile grains in this sample almost one third of it contain small quantities of iron, and some also have traces of silica. Some of the fluorapatites have traces of manganese.

3.1.4 Chutani Formation (CH-D)

3.1.4.1 Zircon fraction (ZRF5 CH-D)

This sample includes zircon (~ 84 %), rutile (~ 6 %), fluorapatite (~ 9 %), chlorapatite (< 1 %) and tourmaline (< 1 %). Size ranges are presented in Table 13.

Table 13: Size ranges (µm) for sample ZRF5 CH-D.

Zircon	40-100
Rutile	50-80
Apatite-(F)	40-90
Apatite-(Cl)	70
Tourmaline	60

Zircon

Angular (Figure 39A) to well-rounded (Figure 39B) zircons were found in sample ZRF5 CH-D. Most of the zircons are fractured (Figure 39B), some are broken (Figure 39C). The well-rounded zircons vary from high to low sphericity. The sub-rounded to angular zircons are either broken (Figure 39C), or euhedral crystals with terminations at both ends (Figure 39A). They range from colorless to grey, some yellowish-brown zircons were also observed.
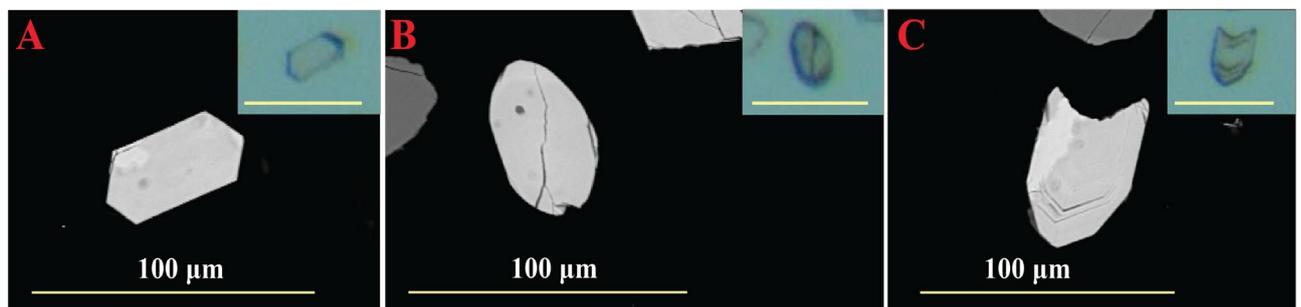
Figure 39: Different types of zircons in ZRF5 CH-D. BSE images, with inset of optical microscopy images. Scales of inset images are all 100 µm.

Rutile

The rutile grains are shades of brown to brownish black (Figure 40). The brownish black grains are opaque authigenic rutile (Figure 40C), while the brown detrital rutile grains are rounded to well-rounded (Figure 40).
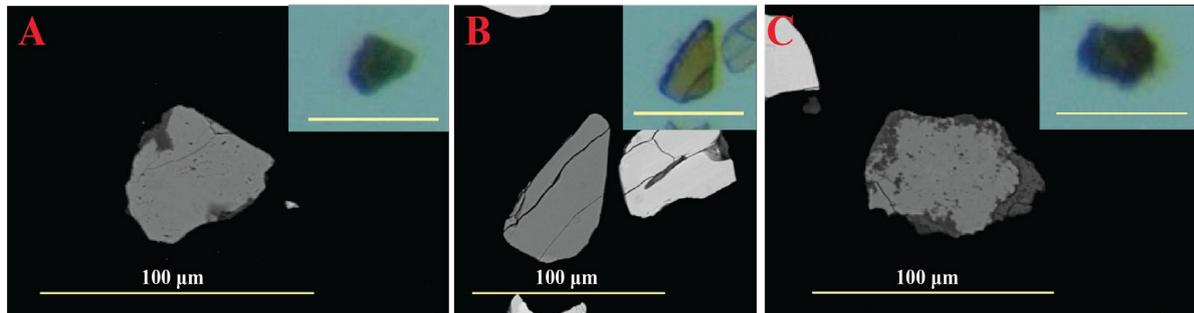
Figure 40: Different rutile grains from ZRF5 CH-D. BSE images with insets of optical microscopy images. Scales of inset images are all 100 μm.

Apatite

In sample ZRF5 CH-D, one grain of chlorapatite (Figure 41A) was identified, while fluorapatites (Figure 41B) were more dominant. The apatite grains were mostly well-rounded, however they do not always look well-rounded when studying the BSE images, as the grains are not polished sufficiently to exhibit their true shape. One hexagonal fluorapatite was seen (Figure 41B). The apatite grains are mostly colorless to light grey or yellow. Chemically, most apatite grains contain both fluorine and chlorine, and thus labelled according to which of these elements is more abundant.
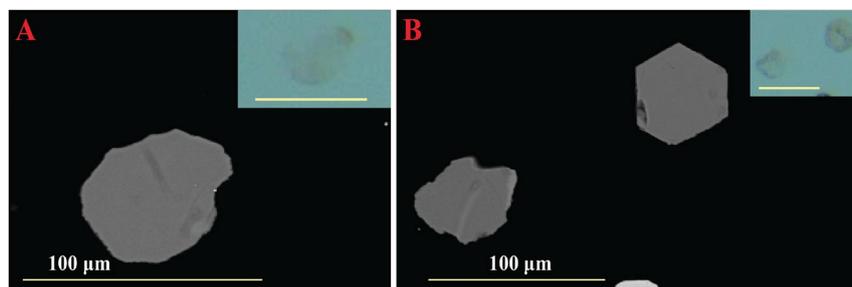
Figure 41: Different types of apatite in ZRF5 CH-D. BSE images with insets of optical microscopy images. Scale of inset images are 100 μm. A) Apatite-(Cl); B) Apatite-(F).

Other minerals

This sample also contain tourmaline, which contains traces of titanium.

3.1.4.2 Apatite fraction (APF5 CH-D)

The apatite fraction of the Chutani Formation includes zircon (< 1 %), rutile (< 1 %), fluorapatite (~ 69 %), chlorapatite (~ 28 %), iron oxide (~ 1 %), and tourmaline (< 1 %). All size ranges are presented in Table 14.

Table 14: Size ranges (µm) for sample APF5 CH-D.

Zircon	50
Rutile	85
Apatite-(F)	30-230
Apatite-(Cl)	40-250
Iron oxide	20
Amphibole	100

Apatite

In this fraction the apatite grains (Figure 42) have both chlorine and fluorine in them, and the amounts of these elements are often very similar, making identification more difficult. The fluorapatite are the ones with larger amount of fluorine, while chlorapatites have larger amounts of chlorine compared to fluorine. The apatite grains also have sodium (Na < 3 %), silica (Si < 2 %), and traces of sulfur. The chlorapatite in this sample have a higher content of chlorine compared to the other formations in this thesis.

The apatite grains are angular to well-rounded, when studying the optical microscopy images, and the sphericity vary as well. The coloring of the grains ranges from colorless to light greyish (Figure 42A and B) or yellow (Figure 42C). There is no notable difference in the chemistry from colorless grains to yellow grains, but it is noted that this is the only formation where the chemistry also indicates sodium, silica and sulfur present in all apatite grains. The grains look quite weathered compared to previous formations, but it seems this could also be an effect of the polishing, as there are rather more weathered grains at one side of the mount compared to the other side.
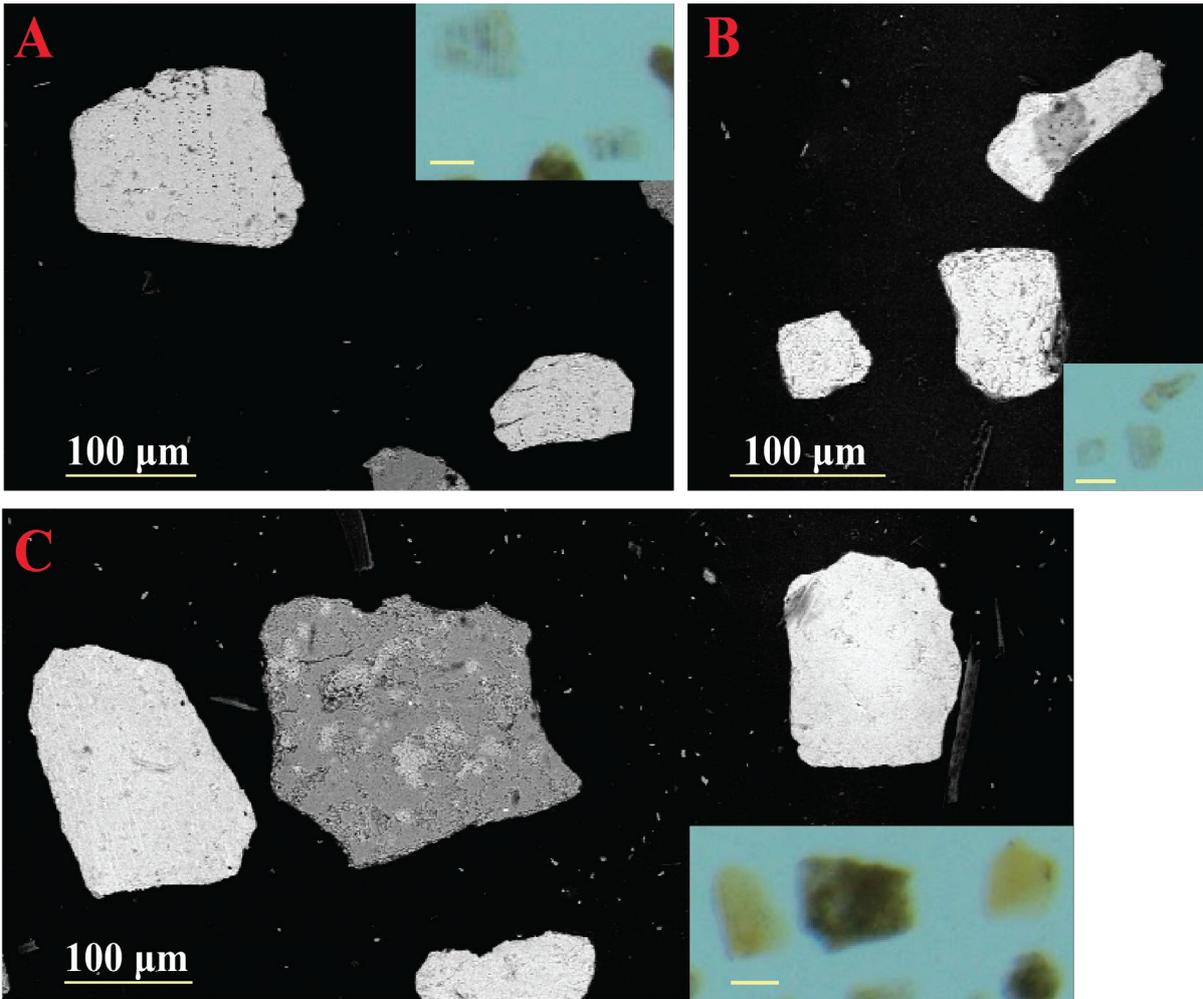
Figure 42: Fluorapatites in the apatite fraction of the Chutani FM sample. BSE images with insets of optical microscopy images. Scale of inset images are 100 μm. A) two fluorapatites; B) three fluorapatites, where the topmost also contains iron; C) two yellow fluorapatites (left and right in the image).

Other minerals

There is also some iron oxide, zircon, rutile and amphibole in this sample.

3.1.4.3 Magnetic fraction (MAG5 CH-D)

This sample consists mainly of iron oxide (~ 89 %), but it also contains zircon (~ 4 %), rutile (< 1 %), fluorapatite (~ 4 %), chlorapatite (~ 1 %), and small amounts of amphibole (< 1 %) and an unknown (< 1 %) mineral. Size ranges are presented in Table 15.

Table 15: Size ranges (µm) for sample MAG5 CH-D.

Zircon	20-70
Rutile	40
Apatite-(F)	40-100
Apatite-(Cl)	50-60
Iron oxide	30-300
Amphibole	265
Unknown	60

Iron oxide

The iron oxide grains in the Chutani Formation differ from the other formations, since the grains display massive iron phases (with very little oxygen) in the core, and iron oxide further out. Thus, depending on where in the grains the EDS analysis was carried out, there would be different results. For simplicity reasons, these grains have then been quantified as iron oxide. Furthermore, the iron oxide datapoint in this sample can be divided into two datapoints: one regular iron oxide with only iron and oxygen (traces of silica and sometimes also aluminum or calcium), and one iron oxide with the addition of traces of chromium (Cr) pointing to a spinel (Figure 43).
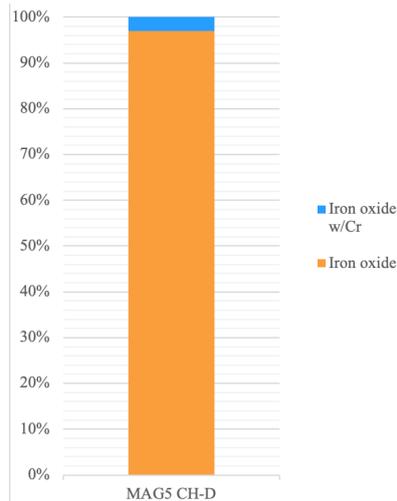
Figure 43: Amount of iron oxide with chromium, and regular iron oxide in MAG5 CH-D. The total of these two iron oxides are included in the "iron oxide" datapoint in previous figures. W/Cr = with chromium.

The iron oxide grains in this sample looks quite different from the ones seen in other formations. Although the grains are opaque, brown to black in color, the EDS images display very different shapes (Figure 44). In the EDS image, there are different shades of grey. The brighter areas contain about 30 % more iron (Fe) compared to the darker areas of the grains. This iron phase (bright areas) contains very little oxygen, perhaps up to 6 % in some cases. The outer parts of these grains are iron oxide, which have around 20-30 % oxygen. There is no visual difference between the iron oxide with or without chromium (Cr).
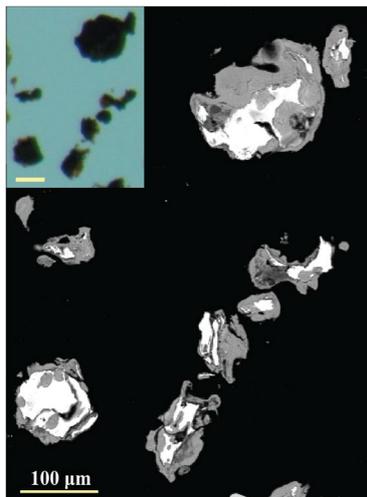
Figure 44: Iron oxide in MAG5 CH-D. The brighter areas contain very little oxygen, and about 30% more iron compared to the darker areas. BSE image with inset of optical microscopy image. Scale of inset image is 100 μm.

Apatite-(F)

The fluorapatites (Figure 45) in this sample are similar as the ones in the apatite fraction of the Chutani Formation sample. The only noticeable difference is the appearances of the grains in the EDS images. The grains look much less brittle than they do in APF5 CH-D, suggesting the appearance of apatite grains in the apatite fraction is a polishing effect.
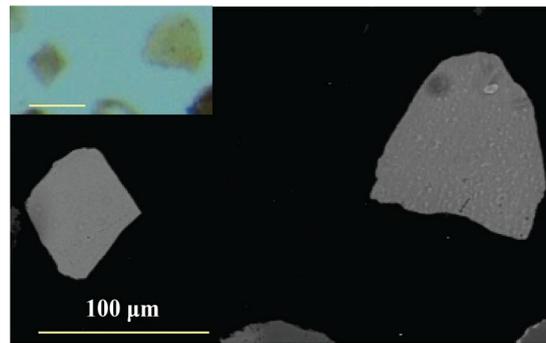
Figure 45: Fluorapatites in MAG5 CH-D. BSE image with inset of optical microscopy images. Scale of inset image is 100 μm.

Amphibole

One amphibole was discovered in this sample. The chemistry, color and presence of cleavage was used to differentiate it from tourmaline. It is a colorless and elongated grain (Figure 46).
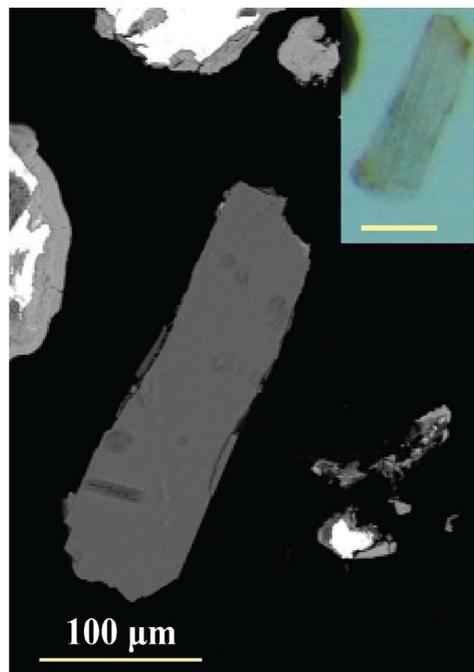
Figure 46: Amphibole in MAG5 CH-D. BSE image with inset of optical microscopy image. Scale of inset image is 100 μm. Cleavages are visible along the length of the grain and is best seen in inset image.

Other minerals

There are also zircons in this sample, and they are angular to well-rounded. Some have one rounded end and exhibit nice angular termination at the other end, while others are broken. Two chlorapatite grains, one rutile grain and an unknown grain were observed. The unknown grain contains sulfur, iron and manganese. This grain is black and opaque in the optical microscope.

3.1.5 Tiquina Formation (TQ7)

3.1.5.1 Zircon fraction (ZRF5 TQ7)

The zircon fraction of the Tiquina Formation includes zircon (~ 28 %), rutile (~ 14 %), barite (~ 28 %), fluorapatite (~ 28 %), and small amounts of chlorapatite (< 1 %), ilmenite (< 1 %), and iron oxide (~ 2 %). All size ranges are presented in Table 16.

Table 16: Size ranges (µm) for minerals in sample ZRF5 TQ7.

Zircon	40-160
Rutile	40-160
Barite	30-200
Apatite-(F)	40-120
Apatite-(Cl)	50
Ilmenite	120
Iron oxide	85-150

Zircon

The zircons (Figure 47) in sample ZRF5 TQ7 vary from angular (Figure 47A) to well-rounded (two top left zircons in Figure 47B and the two lowermost zircons in Figure 47C). Most of them are broken (Figure 47D and E), some are fractured. The sphericity of the zircons varies: the very broken fragments are angular, with high sphericity. There are some well-rounded with high sphericity, and some more elongated. Crystals with well-developed habit, have termination in one (Figure 47A) or both ends (often broken in one end). These vary in sphericity and are angular to rounded grains. Even in the BSE images, many zircons are seen to have zoning (Figure 47A), which is especially evident in the CL images. They range from colorless to light grey, and some are almost light brown (lower right zircon in Figure 47C).
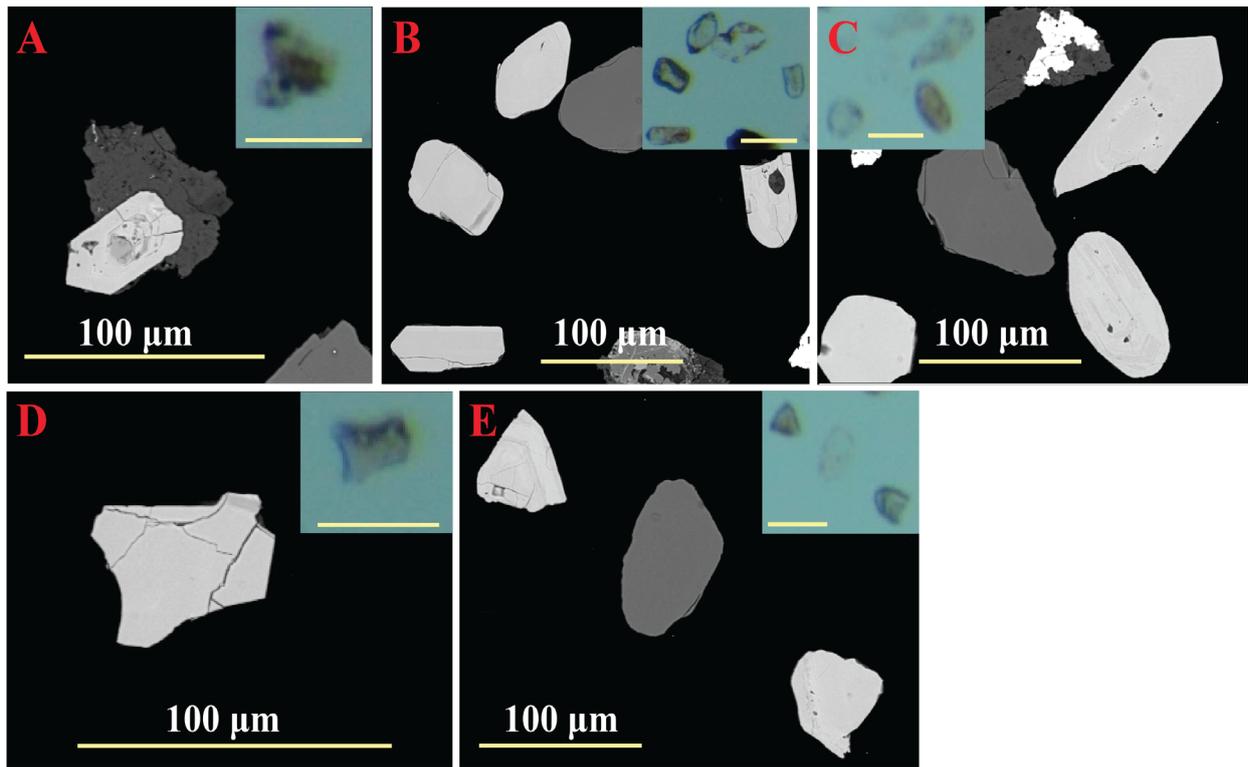
Figure 47: Different types of zircons (the brighter colored grains) in ZRF5 TQ7. BSE images with insets of optical microscopy images. Scale of inset images are 100 µm.

Rutile

The rutile grains in this sample are brown and transparent detrital grains (Figure 48). The elongated grains (Figure 48A) are the most common, while the well-rounded, high sphericity, rutile grains (Figure 48B) are less common.
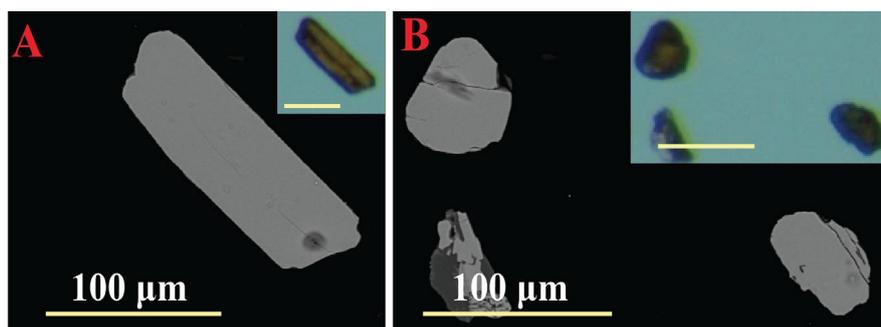
Figure 48: Rutile grains in sample ZRF5 TQ7. BSE images with insets of optical microscopy images. Scale of inset images are 100 µm.

Apatite-(F)

The fluorapatites in this fraction are mostly well-rounded grains (Figure 49). The sphericity varies from high to low. The grains are colorless to light grey, some have brown impurities. All these grains contain both fluorine and chlorine.
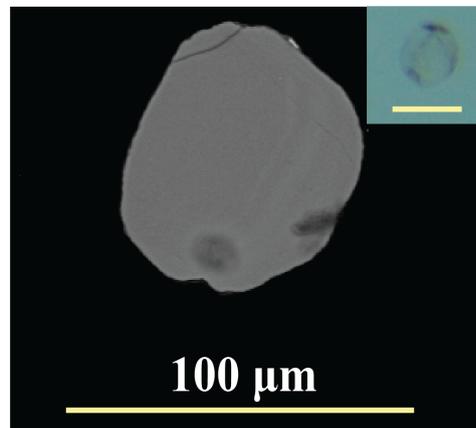
Figure 49: Example of apatite-(F) from ZRF5 TQ7. BSE image with inset of optical microscopy image. Scale of inset image is 100 μm.

Barite

Barite is seen to replace or grow on light minerals in ZRF5 TQ7. The bright areas in Figure 50 are barite, while the darker areas around are light minerals. The color of the barite grains is steel grey to colorless (Figure 50: inset image). Most of the barite grains contain traces of strontium.
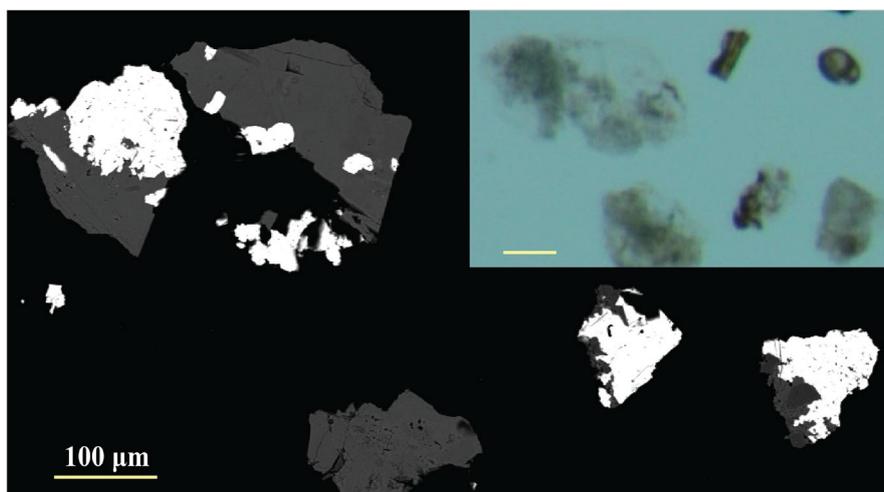
Figure 50: The very bright areas are barite (sample ZRF5 TQ7). BSE image with inset of optical microscopy image. Scale of inset image is 100 μm.

Other minerals

There are also small occurrences of iron oxide, ilmenite and chlorapatite in this sample. The iron oxides have traces of different elements: titanium, silica and aluminum. The ilmenites contain traces of silica.

3.1.5.2 Apatite fraction (APF5 TQ7)

This sample is the only one not containing any zircons. But is includes rutile (~ 2 %), barite (~ 21 %), fluorapatite (~ 44 %), chlorapatite (~ 31 %) and iron oxide (~ 2 %). All size ranges are given in Table 17.

Table 17: Size ranges (µm) for minerals in sample APF5 TQ7.

Rutile	40-70
Barite	25-175
Apatite-(F)	35-150
Apatite-(Cl)	25-145
Iron oxide	30-130

Apatite

These grains (Figure 51) are mainly well-rounded to rounded, with high sphericity, but some are also more elongated. A small amount of grains is angular or sub-angular. These are mostly broken, thus making one end more angular while the other is rounded. The grains appear fragile in this sample, which was probably polished too much. There is no apparent visual difference between the fluorapatite and chlorapatite. In Figure 51, the light grey grains (BSE image) are apatites. The lower left grain is a chlorapatite, while the rest are fluorapatites. The EDS analysis often indicate small amounts of silica/sodium, but no sulfur. Only the Chutani Formation seems to have similar EDS spectrums.
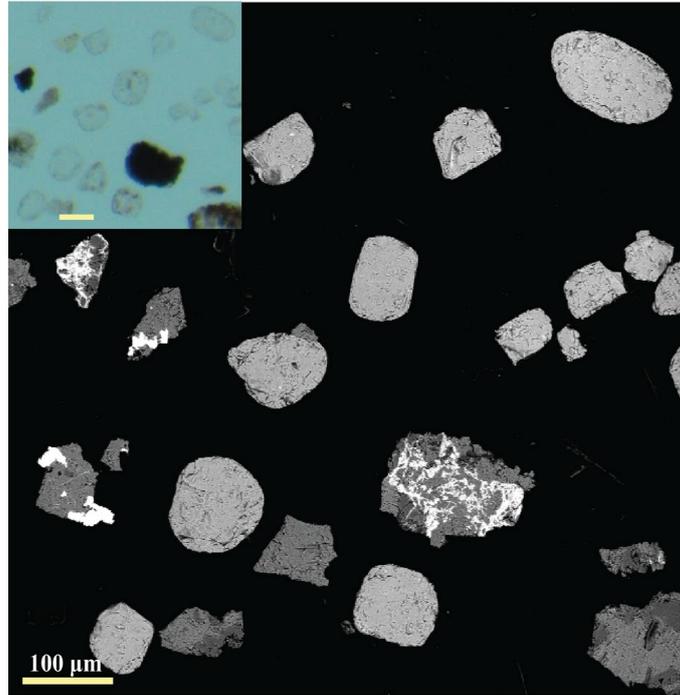
Figure 51: Apatites (light grey grains, like the one next to the scale in the BSE image) in sample APF5 TQ7. BSE image with inset of optical microscopy image. Scale of inset image is 100 μm.

Barite

The barite in sample APF5 TQ7 is almost identical the barite described for sample ZRF5 TQ7. There are small traces of silica/sodium in the barite grains of APF5 TQ7.

Other minerals

Iron oxide and rutile are the last minerals found in this sample. These minerals both appear as opaque black grains. In the BSE images, they can be seen replacing or growing on other lighter minerals. The iron oxides have traces of titanium.

3.1.5.3 Magnetic fraction (MAG5 TQ7)

The magnetic fraction of TQ7 contains zircon (~ 3 %), rutile (~ 4 %), barite (~ 2 %), fluorapatite (~ 10 %), chlorapatite (< 1 %), ilmenite (~ 2 %), iron oxide (~ 80 %), and small amounts of monazite (< 1 %). All size ranges are given in

Table 18. Iron oxide grains with chromite are 30-90 μm, while the iron oxide grains with titanium are 20-180 μm. These are included in the "iron oxide".

What is worth noting in this sample, is the amount of lithoclasts of volcanic appearance, visible in the BSE images. Many interesting shapes were seen, but as these lithoclasts are a mix of minerals, it was out of the scope within the time constraints of the thesis to examine the minerology in all detail as well, for those grains.

Table 18: Size ranges (μm) for minerals in sample MAG5 TQ7.

Zircon	40-150
Rutile	30-130
Ilmenite	30-95
Barite	30-140
Apatite-(F)	40-120
Apatite-(Cl)	60
Iron oxide	20-180
Chromite	30-60

Iron oxide

The "iron oxide" datapoint of this sample consists of three types of iron oxides (Figure 52). These are iron oxide with chromium, iron oxide with titanium and regular iron oxide with mainly iron and oxygen. Many iron oxide grains contain traces of aluminum and silica, as well as small amounts (< 3 %) of titanium, manganese and magnesium. If there is titanium (Ti) present in the grain, it is counted as "iron oxide w/Ti".
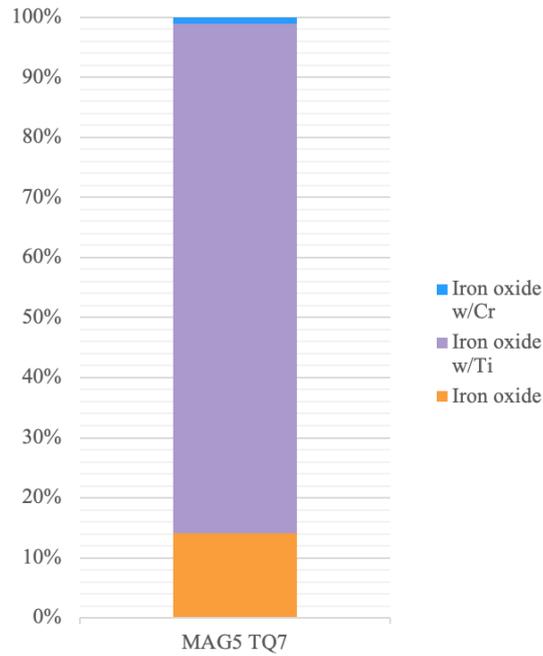
Figure 52: Amount of iron oxide with chromium, iron oxide with titanium and regular iron oxide in MAG5 TQ7. The total of these three iron oxides are included in the "iron oxide" datapoint in previous figures. W/Ti = with titanium; w/Cr = with chromium.

The grains (Figure 53) are all opaque black grains with varying shapes. There are more grains with high sphericity, than low sphericity. The grains vary from well-rounded to angular. Many of the grains exhibit interesting internal structures.
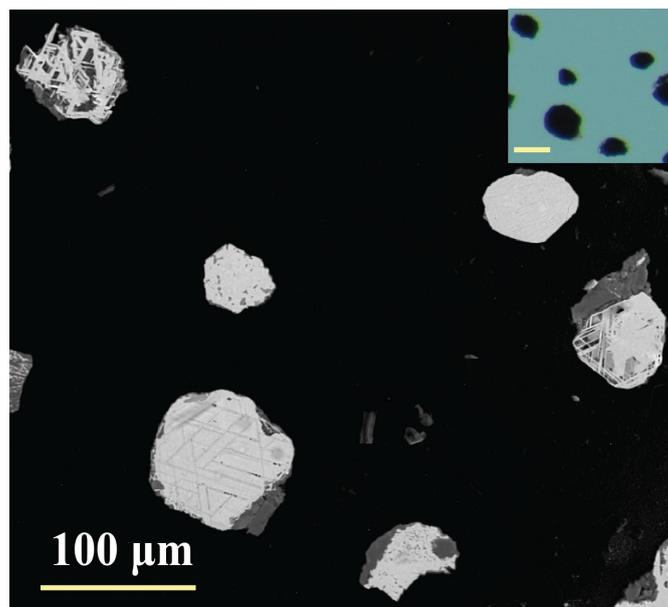
Figure 53: Iron oxide grains from MAG5 TQ7. Note the internal structures visible in the BSE image. BSE image with inset of optical microscopy image. Scale of inset image is 100 μm.

Ilmenite

Ilmenite occur as black, opaque, sub-angular to well-rounded grains, with high sphericity (Figure 54).
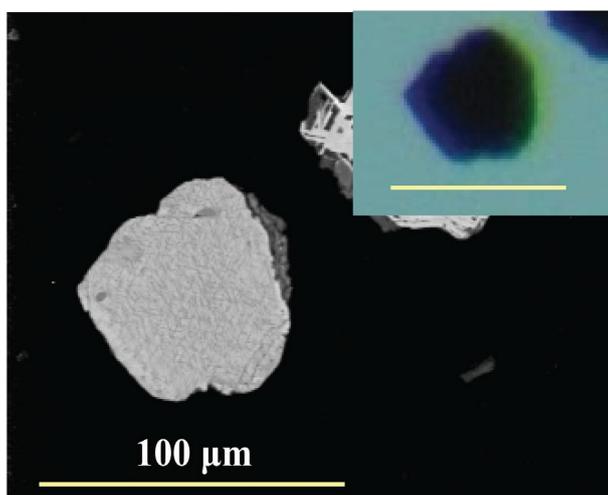
Figure 54: Ilmenite grain in sample MAG5 TQ7. BSE image with inset of optical microscopy image. Scale of inset image is 100 μm.

Chromite

The chromite grains are angular to rounded (Figure 55), with high sphericity. They are all black and opaque.
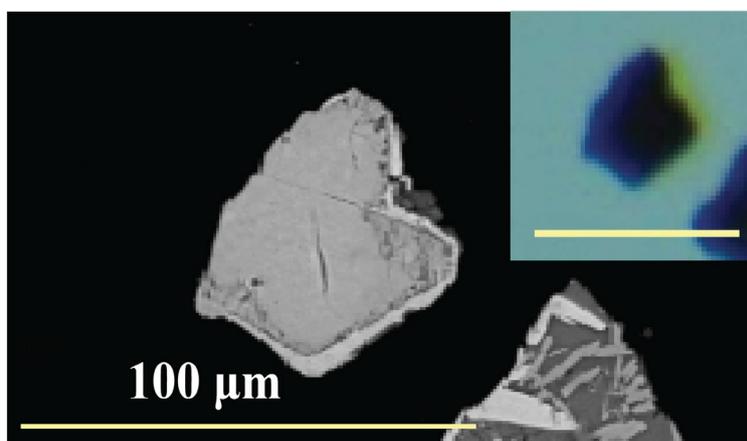
Figure 55: Chromite grain from MAG5 TQ7. BSE image with inset of optical microscopy image. Scale of inset image is 100 μm.

Other minerals

There are also zircon, rutile, barite, apatite-(F) and apatite-(Cl) grains in this sample. Appearances are as described in the other fractions of the Tiquina Formation sample. No brown detrital rutile grains were seen, only opaque, black authigenic rutile grains.

4. DISCUSSION

When reviewing the heavy mineral composition of selected Paleozoic to Mesozoic rock successions in northwest Bolivia the primary heavy mineral suite, as well as the secondary minerals, grown during post-depositional processes, are of relevance. Some post-depositional minerals are rather abundant and would hamper the quantifications. Hence, first some discussion upon those which are of importance for the evaluation of the geological history.

The abundant pyrite grains in the Cancañiri Formation are probably post-depositional, evidenced by the angular cubical crystals (no transport), and would suggest an anoxic post-depositional environment. The Cancañiri Formation correlates to the diamictite of the Zapla Formation (Reimann et al., 2006) of northwestern Argentina, which also demonstrate signs of partially dysoxic to anoxic depositional environment (Benedetto et al., 2015). This diamictite also correlate to the Peruvian Altiplano, as the San Gabán Formation (Reimann et al., 2006). Hence, these partially anoxic depositional environments evidenced in the Cancañiri and Zapla Formations, are proposed to be of regional occurrence, and subsequently linked to the Hirnantian glaciation and deglaciation.

The occurrence of barite could be caused by numerous factors, both regionally and locally. It can often occur as a pore-filling mineral, or due to hydrothermal fluids circulating in the rock, hence be a post-depositional mineral. In this study, barite was found in the Vila Vila, Copacabana and Tiquina Formations, and the visual appearance of it suggests an authigenic or diagenetic mineral occurrence. Authigenic barite could be only a local phenomenon. Ankerite can also occur as a diagenetic mineral, and was mainly found in the Vila Vila Formation, but also as a small occurrence in the Copacabana Formation. The carbonate supply could very well be delivered by the massive carbonate deposits of the Copacabana Formation (Grader et al., 2000) and the mobilization of the fluids during regional tectonic events in the Late Mesozoic or Cenozoic (Sempere, 1995).

The occurrence of massive iron phases in the Chutani Formation could suggest an oxygen depleted depositional environment as well, where these iron phases were later exposed to oxygen, and hence oxidized into iron oxide. The core of these grains is still iron (< 6 % O), with iron oxide (20-30% O) covering the outer parts of the Fe-rich grains, suggesting that the oxidation has occurred post-depositional. The origin of the iron is well established in the overlying Tiquina Formation with its syn-sedimentary mafic volcanism (Berg-Larsen et al., 2018).

The ZTR index (zircon, tourmaline and rutile) indicate the degree of recycling of the sample material. It is calculated using the amount of zircon, tourmaline and rutile divided by the total amount of non-opaque heavy mineral grains (Hubert, 1962). Since the samples in this thesis are divided into three heavy mineral fractions, the average values for the three fractions were used to calculate the values for the entire sample. For formations with a higher ZTR index (Table 19), the rocks contain highly recycled material. As was expected, the older formations display a higher ZTR index compared to the younger rocks. This is also supported by the observations given in the results, regarding the roundness of grains. When calculating the ZTR index, to simplify, the total rutile content for each sample was used. This could influence the ZTR index as there are some rutile which are opaque, authigenic rutile. When quantifying, no separation of the two types of rutile was made due to time constraints.

Table 19: ZTR index (%) for samples included in this study.

Formation	Sample name	ZTR index (%)
Tiquina	TQ7	23
Chutani	CH-D	46
Copacabana	COPA1	57
Vila Vila	VV1	54
Cancañiri	CCE	61

The grainsizes for ZTR minerals are given in Table 20. The most recycled rocks should generally have smaller grain size variations for zircon, tourmaline and rutile, compared to less recycled rocks. Here, it can be observed that the oldest formation (Cancañiri Formation) display the largest variability of grain sizes within these heavy minerals, which points either to a depositional environment with poor sorting, like a fluvial system for instance, or two clear different influences of source components.

Table 20: ZTR grainsizes (µm) for samples discussed in this thesis.

Formation:	Cancañiri	Vila Vila	Copacabana	Chutani	Tiquina
Sample name:	CCE	VV1	COPA1	CH-D	TQ7
Zircon	30-240	30-155	30-215	40-100	40-160
Rutile	30-200	20-185	25-200	40-80	40-160
Tourmaline	60-300	30-160	50-215	60	

The occurrence of ultra-stable minerals, such as zircon, tourmaline and rutile (ZTR), as well as amphibole (possibly arc related) was calculated for all five formations, using the average occurrence for all three heavy mineral fractions. This change in important mineral input is illustrated graphically in Figure 56, illustrating how this input vary over time. Amphibole was only found in a small quantity, and then only in the Vila Vila and Chutani Formations. Hence, this would not indicate a major provenance change.
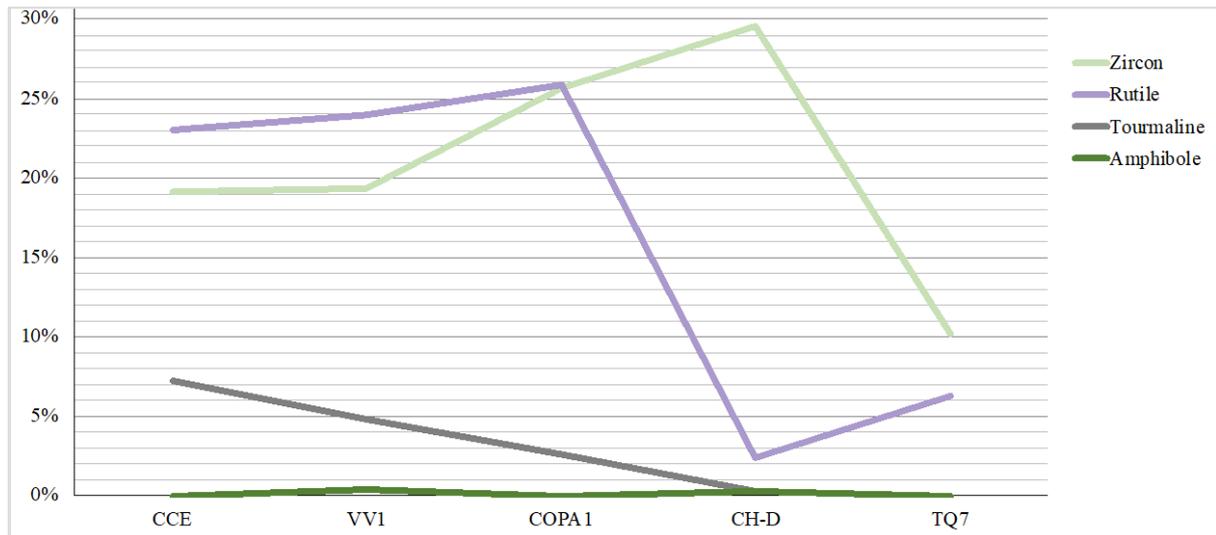
Figure 56: Occurrence (%) of zircon, rutile, tourmaline and amphibole in the samples (formations) in this study. Average values for all three HM fractions were used to calculate the values for the entire formation. Sorted by old (left) to young (right). CCE = Cancañiri FM (Formation); VV1 = Vila Vila FM; COPA1 = Copacabana FM; CH-D = Chutani FM; TQ7 = Tiquina FM.

For the oldest sample (CCE), the ultra-stable minerals (Mange and Morton, 2007), are mostly well-rounded. The stable mineral apatite is also well-rounded. This could indicate that the sample material has been transported some distance or that is has survived several degrees of recycling. Seeing as the ultra-stable minerals are as rounded as the less stable apatites, it could be suggested two different sources for these minerals. The grain size for zircons range from 30-240 μm, with one zircon as an extreme at 240 μm. Generally, the zircons range from 30 to around 150 μm.

In the Vila Vila Formation, the zircons are angular to well-rounded. Many of the zircons are angular euhedral crystals. For this sample, it is clear that the zircon grains have multiple sources, suggested by the wide range in roundness of the grains. The well-rounded zircons must have been transported for quite some distance, while the angular euhedral crystals suggest nearly no transport. Rutile grains (non-opaque) in this sample range from well-rounded to

angular, which would also suggest multiple sources for the rutile. Sub-angular to rounded tourmalines suggest less weathering of these compared to the well-rounded zircon and rutile grains. Some tourmalines still display terminations or a hexagonal shape, suggesting that there is a lower degree of transportation/recycling of these grains. Angular to well-rounded apatite grains would also point to multiple sources. Some amphiboles were observed in this formation. The presence of amphibole, which is a less stable mineral (Mange and Morton, 2007), suggests very short transport. The occurrence of xenotime could be diagenetic, suggested by the euhedral crystal found in this sample. The detrital monazite grains are, in contrast, well-rounded. Monazite is rather instable and would dissolve rapidly, hence the source of monazite must have been rather proximal to the depositional area.

The zircons in the Copacabana Formation are mostly angular, with many euhedral crystals present in the sample. In addition to this, some well-rounded zircons were observed, which would then indicate multiple sources due to the different degrees of roundness. The tourmaline and rutile grains are well-rounded to rounded and sub-rounded, respectively, which could suggest a different source for these compared to the angular euhedral zircon grains. Apatite grains are well-rounded and have high sphericity, which imply some transport, as are the monazite grains, although both are rather fragile, hence the source had to be relatively close to the depositional area.

For the Chutani Formation, both angular (often euhedral) zircon crystals, as well as well-rounded ones are present, implying multiple sources for the zircons. The rutile grains are rounded to well-rounded, which indicates long transportation or many degrees of recycling. Tourmaline is almost absent in the Chutani Formation, with only one grain identified between all three fractions (here in the ZRF, elsewhere in this thesis seen in MAG). Apatite grains range from well-rounded to angular, and one euhedral apatite was observed. As these apatite grains imply varying degrees of transport, it indicates multiple sources for this mineral. A notion which is especially enhanced due to the presence of one euhedral apatite crystal. As the crystal is angular, it suggests that is has not endured (nearly) any transport/recycling.

Of the ultra-stable minerals in the Tiquina Formation, only rutile and zircon were identified, again a paucity of tourmaline, which is compelling. The zircons range from well-rounded, to angular euhedral crystals or broken grains. The rutile grains are well-rounded, and the same is observed for the apatite grains.

The Cancañiri Formation is, as expected, the most recycled. The Tiquina Formation is, by far, the most unrecycled. This points to a new source area and to a very different depositional environment where recycling is rather less significant. Hence, a facies with high sedimentation rates and quick burial. This may happen in a paleogeography with an extreme topography like in rather young orogenic areas.

Amphibole was not expected to be found in a large amount, in any of the rocks, as it is relatively unstable to chemical weathering (Mange and Morton, 2007). Small occurrences were nevertheless discovered in the Vila Vila Formation and the Chutani Formation. The Chutani Formation does not have too much rock material on-top and the rocks are relatively unaffected by diagenesis (Berg-Larsen et al., 2018), and thus the weathering of amphibole was probably minimalized. The discovery in the Vila Vila Formation is around the same amount as in the Chutani Formation. This is more surprising given the age of the rocks, as well as the clear evidence of diagenesis given by other authigenic mineral occurrences in this sample. But it may be that during the Devonian a small-scale new source area had been exposed and shed this source component. Generally, introduction of amphiboles may indicate the appearance of arc-related sources or metamorphic rocks after exhumation. The former is not the case as then amphiboles should have been identified in a small amount in the Silurian deposits. However, when analyzing the entire Devonian stratigraphy in post-Corona times this enigma may possibly be resolved.

Amphibole and apatite are both arc-related heavy minerals found in granites, andesites and basalts, and diorite. Both are also present in extensional systems and in collisional orogens, however the latter can generally be excluded in this geological region during Ordovician to Triassic (Sempere, 1995). Apatite was found in all samples, while amphibole was only present in two. As previously mentioned, the Cancañiri Formation was deposited subsequently to arc activity (Zumsprekel et al., 2015). Another volcanic arc emerged as the Copacabana Formation was deposited, the Chutani Formation represents syn-arc deposits, and the Tiquina Formation represents post-arc deposits. It was therefore expected to see arc-related minerals in these rocks. Amphiboles were only detected in the Vila Vila Formation and the Chutani Formation. A large degree of recycling, or diagenesis, of the older rocks could explain the absence of amphibole. Apatite is most abundant in the younger formations and may point to such an influence. However, the question would be where a late Paleozoic arc has been located, and if the syn-

sedimentary volcanic rocks of the Tiquina Formation (Berg-Larsen et al., 2018) are arc-related or associated with extensional tectonics.

However, all provenance related processes related to ceasing or emerging volcanic arcs are rather reduced in their significance. This may indicate that those changes, observed in northwest Argentina during the Ordovician for instance (Zimmermann and Bahlburg, 2003), are here less impactful. This could possibly be because of their paleogeographic position being rather distal from these tectonic units, combined with possibly unfortunate sediment transport systems, to reveal those changes at the margin of Gondwana during the Paleozoic and South America after the break-up of Pangea. The occurrence of redox-sensitive heavy minerals is very obvious, indicating severe climatic changes (pyrite in the Silurian successions) and most probably thin sedimentary cover of post-Triassic times causing a low degree of diagenesis.

4.1 RELIABILITY OF THE DATA

Although 100-150 grains of heavy mineral fraction are sufficient for subsequent interpretations (Andò and Garzanti, 2013) results may be more robust with several hundred grains analyzed using an automated SEM as planned. However, the general trend is definitely presented in this thesis as well, when used "traditional" SEM-EDS methodology in a point-counting mechanism.

A second issue may be the use of EDS. This is an analytical method which is not entirely quantitative, as the weight percent of the measured elements in the spectra can vary. The method lacks a clear standardization for every analyzed mineral and overlap of energy peaks hamper the calculation of absolute values. This is therefore here not intended to do so, just a major trend can be interpreted: higher or lower peak may point to a higher or lower abundance of a specific element. Some elements are difficult to measure in small amounts, like B or Li at a level to be useful for mineral identification. Thus, some minerals could be mistakenly identified, due to the weight percent of some of the elements. This is minimized when studying the same minerals with an optical microscope, but this has also major limits specifically when trying to differentiate tourmaline and chain-silicates. This effect would have been minimized if applying MLA, as initially planned.

5. CONCLUSIONS

For this study, a high resolution heavy mineral analysis was carried out with the aim of shedding light on the provenance of the detrital material of the selected formations from Paleozoic to Mesozoic times in northwest Bolivia. The chosen method gave the opportunity to study both grain size, shape and chemical composition of the material. The samples range from the Silurian to the Triassic, and the results imply a change in the mineralogical content of the rocks in question.

Arc-related minerals such as apatite and amphibole were identified among the sample material, where apatite is common in arc-related and affected formations (Chutani and Tiquina), while amphibole was only recognized in the Vila Vila and Chutani Formations, representing arc-related input in these rocks or for the Devonian Vila Vila succession a metamorphic source.

The ultra-stable minerals indicate several sources for the sediments, as evidenced by the varying roundness of the grains. Especially interesting are the euhedral, angular, zircon crystals seen in most formations (all except Cancañiri), which would suggest a proximal source for these grains, dating of these grains would provide further information. These samples also demonstrate varying recycling of the ultra-stable minerals, suggesting multiple sources for each formation. The ZTR index indicate a higher recycling of the sediments in the Cancañiri Formation compared to the other formations, which is also supported by the well-rounded ultra-stable minerals in this sample, but interesting enough the formation also holds very large grains, which may give some hints for the depositional process.

Post-depositional minerals such as pyrite, barite, xenotime, partly rutile, and ankerite were identified. Pyrite was only present in the Cancañiri Formation and could imply an anoxic post-depositional environment. This correlates to the Zapla Formation in northwestern Argentina, suggesting a regional oxygen depleted depositional environment caused by sea-level rise after the Hirnantian glacial event. Another good indicator of the depositional environment is seen in the Chutani Formation. Here, massive iron phases (< 6 % O) were observed (outer parts of the grains were more oxidized). This points to an oxygen depleted depositional environment when the Chutani Formation was deposited during Permian times.

Conclusively, the methodological approach could identify very clear different stages of provenance changes and pinpoint less recycling activity in deposits related to or deposited closely after orogenic events. This was not the case for the Cancañiri Formation, and an explanation could be that the deposit is rather younger than expected and deposited distal to

the Ordovician volcanic arc, thus these changes that occurred, and are for instance evident in Argentina, are not seen here to such an extent. A distal paleogeographic position from these tectonic units, combined with unfortunate sedimentary transport, could be why these changes at the margin of Gondwana, after the break-up of Pangea, are not evident in these rocks.

REFERENCES

Andò, S., Garzanti, E., 2013. Raman spectroscopy in heavy-mineral studies. Geological Society London Special Publications 386, 395–412. https://doi.org/10.1144/SP386.2

Andò, S., Morton, A., Garzanti, E., 2014. Metamorphic grade of source rocks revealed by chemical fingerprints of detrital amphibole and garnet. Geological Society, London, Special Publications 386, 351–371. https://doi.org/10.1144/SP386.5

Arntzen, S.K., Olsen, T.M., Lopez, V.S.S., Di Pasquo, M., Zimmermann, U., Ruud, C., Berndt, J., 2018. Devonian or Carboniferous glaciations in the Bolivian Altiplano: Constraints from detrital zircon age dating. Presented at the 11th South American Symposium on Isotope Geology (SSAGI), Cochabamba, Bolivia.

Bahlburg, H., Vervoort, J.D., Andrew DuFrane, S., Carlotto, V., Reimann, C., Cárdenas, J., 2011. The U–Pb and Hf isotope evidence of detrital zircons of the Ordovician Ollantaytambo Formation, southern Peru, and the Ordovician provenance and paleogeography of southern Peru and northern Bolivia. Journal of South American Earth Sciences 32, 196–209. https://doi.org/10.1016/j.jsames.2011.07.002

Bahlburg, H., Vervoort, J.D., Du Frane, S.A., Bock, B., Augustsson, C., Reimann, C., 2009. Timing of crust formation and recycling in accretionary orogens: Insights learned from the western margin of South America. Earth-Science Reviews 97, 215–241. https://doi.org/10.1016/j.earscirev.2009.10.006

Benedetto, J.L., 2013. Upper Ordovician Brachiopods from the San Benito Formation, Cordillera del Tunari, Bolivia. Ameghiniana 50, 418–428. https://doi.org/10.5710/AMGH.05.03.2013.558

Benedetto, J.L., Halpern, K., de la Puente, G.S., Monaldi, C.R., 2015. An in situ shelly fauna from the lower Paleozoic Zapla diamictite of northwestern Argentina: Implications for the age of glacial events across Gondwana. Journal of South American Earth Sciences 64, 166–182. https://doi.org/10.1016/j.jsames.2015.10.004

Berg-Larsen, K., Hystad, H.E.L., Nerhus, I., Skjeldal, M.E., Ruud, C., Zimmermann, U., Lopez, V.S.S., Bertolino, A.R.S., Berndt, J., 2018. Provenance of Permo-Triassic rocks in the Bolivian Altiplano. Presented at the 11th South American Symposium on Isotope Geology (SSAGI), Cochabamba, Bolivia.

Deer, W.A., Howie, R.A., Zussman, J., 1992. An introduction to the rock-forming minerals, 2nd ed. Longman, Harlow.

Goldstein, J., Newbury, D.E., Echlin, P., Joy, D.C., Fiori, C., Lifshin, E., 1981. Scanning Electron Microscopy and X-Ray Microanalysis: A Text for Biologists, Materials Scientists, and Geologists. Springer US. https://doi.org/10.1007/978-1-4613-3273-2

Google Earth, 2020.

Google Maps, 2020.

Grader, G., Isaacson, P., Rember, B., Mamet, B., Díaz-Martínez, E., Arispe, O., 2000. Stratigraphy and depositional setting of the late Paleozoic Copacabana Formation in Bolivia. Zentralblatt Geologie und Paläontologie 1, 723–741.

Hjelen, J., 1989. Scanning elektron-mikroskopi. SINTEF, Trondheim.

Hubert, J.F., 1962. A zircon-tourmaline-rutile maturity index and the interdependence of the composition of heavy mineral assemblages with the gross composition and texture of sandstones. Journal of Sedimentary Research 32, 440–450. https://doi.org/10.1306/74D70CE5-2B21-11D7-8648000102C1865D

Isaacson, P.E., Martínez, E.D., 1995. Evidence for a Middle–Late Paleozoic Foreland Basin and Significant Paleolatitudinal Shift, Central Andes. Petroleum basins of South America: AAPG Memoir 62 231–249.

Jaillard, E., Hérail, G., Monfret, T., Díaz-Martínez, E., Baby, P., Lavenu, A., Dumont, J.-F.,

2000. Tectonic evolution of the Andes of Ecuador, Peru, Bolivia and northermost Chile. pp. 481–559.

Jiménez, N., López-Velásquez, S., 2008. Magmatism in the Huarina belt, Bolivia, and its geotectonic implications. Tectonophysics 459, 85–106. https://doi.org/10.1016/j.tecto.2007.10.012

Leng, Y., 2013. Materials characterization: Introduction to microscopic and spectroscopic methods: Second edition. https://doi.org/10.1002/9783527670772

Lopez, V.S.S., Conde, M., Cuellar, K.A., Tarqui, J., Zimmermann, U., Ruud, C., Storaas, Ø., Solvang, A., Berndt, J., Bertolino, A.R.S., 2018a. Provenance of Devonian rocks of the Bolivian Altiplano. Presented at the 11th South American Symposium on Isotope Geology (SSAGI), Cochabamba, Bolivia.

Lopez, V.S.S., Cuenca, M.A.C., Silva, P.J.E., Ramirez, S.W., Zimmermann, U., Ruud, C., Berndt, J., 2018b. Provenance of the Oligocene to Miocene Aranjuez Formation at La Paz (Bolivia) and modern river sediments of the Bolivian Altiplano. Presented at the 11th South American Symposium on Isotope Geology (SSAGI), Cochabamba, Bolivia.

Lopez, V.S.S., Di Pasquo, M., Ruud, C., Hatløy, S., Kristoffersen, S., Mehus, T., Skarstein, G., Zimmermann, U., Andersen, T., Berndt, J., Matos, R., 2018c. Provenance of Ordovician(?) to Silurian strata in the Bolivian Altiplano. Presented at the 11th South American Symposium on Isotope Geology (SSAGI), Cochabamba, Bolivia.

Lopez, V.S.S., Gareca, Q.M.R., Mendoza, S.G., Zimmermann, U., Ruud, C., Berndt, J., 2018d. Provenance of the Carboniferous to Permian Copacabana Formation of the Bolivian Altiplano. Presented at the 11th South American Symposium on Isotope Geology (SSAGI), Cochabamba, Bolivia.

Mange, M.A., Maurer, H.F.W., 1992. Heavy Minerals in Colour. Springer Netherlands, Dordrecht, Netherlands.

Mange, M.A., Morton, A.C., 2007. Geochemistry of Heavy Minerals, in: Mange, M.A., Wright, D.T. (Eds.), Developments in Sedimentology, Heavy Minerals in Use. Elsevier, pp. 345–391. https://doi.org/10.1016/S0070-4571(07)58013-1

Reimann, C., Bahlburg, H., Kooijman, E., Berndt, J., Gerdes, A., Carlotto, V., Lopez, S., 2010. Geodynamic evolution of the early Paleozoic Western Gondwana margin 14°–17°S reflected by the detritus of the Devonian and Ordovician basins of southern Peru and northern Bolivia. Gondwana Research 18, 370–384. https://doi.org/10.1016/j.gr.2010.02.002

Reimann, C., Spiske, M., Bahlburg, H., Lopez, S., Carlotto, V., 2006. Sedimentological análisis of the Ordovician and Devonian basins in southern Peru and northern Bolivia.

Sempere, T., 1995. Phanerozoic Evolution of Bolivia and Adjacent Regions.

Sempere, T., Hérail, G., Oller, J., Bonhomme, M.G., 1990. Late Oligocene-early Miocene major tectonic crisis and related basins in Bolivia. Geology 18, 946–949.

Suárez-Soruco, R., 2000. Compendio de geologia de Bolivia.

Suárez-Soruco, R., Díaz-Martínez, E., 1996. Léxico estratigráfico de Bolivia. Revista Tecnica de Yacimientos Petroliferos Fiscales Bolivianos, Bolivia.

Suárez-Soruco, R., Diaz-Martínez, E., 1996. Lexico estratigraphico de Bolivia.

Zimmermann, U., Bahlburg, H., 2003. Provenance analysis and tectonic setting of the Ordovician clastic deposits in the southern Puna Basin, NW Argentina. Sedimentology 50, 1079–1104. https://doi.org/10.1046/j.1365-3091.2003.00595.x

Zumsprekel, C.R., Bahlburg, H., Carlotto, V., Boekhout, F., Berndt, J., Lopez, S., 2015. Multi-method provenance model for early Paleozoic sedimentary basins of southern Peru and northern Bolivia (13°–18°S). Journal of South American Earth Sciences 64, 94–115. https://doi.org/10.1016/j.jsames.2015.08.013

APPENDIX A - FEG-SEM EDS EXAMPLES OF SPECTRUMS FOR DIFFERENT MINERALS

APPENDIX A – FEG-SEM EDS EXAMPLES OF SPECTRUMS FOR DIFFERENT MINERALS

EDS examples of how the different minerals usually appear in these samples are given in this appendix. The peak for carbon is due to the carbon coating and was not removed from the spectrums due to time constraint.

ZIRCON
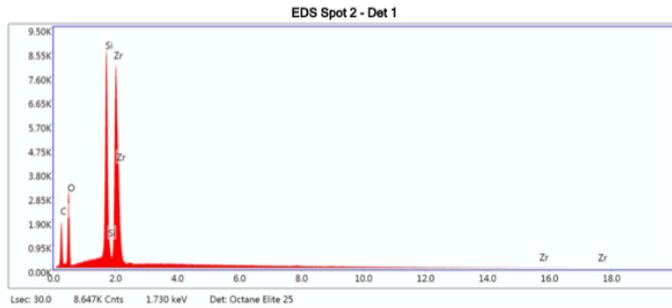
eZAF Smart Quant Results

Element	Weight %	Atomic %	Net Int.	Error %	Kratio	Z	A	F
C K	28.05	49.57	665.19	10.72	0.0469	1.1448	0.1461	1.0000
O K	24.29	32.21	1388.15	10.09	0.0402	1.0999	0.1506	1.0000
SiK	13.64	10.31	5272.61	3.32	0.1115	1.0076	0.8050	1.0072
ZrL	34.01	7.91	5117.75	1.74	0.2548	0.7777	0.9636	0.9997

RUTILE
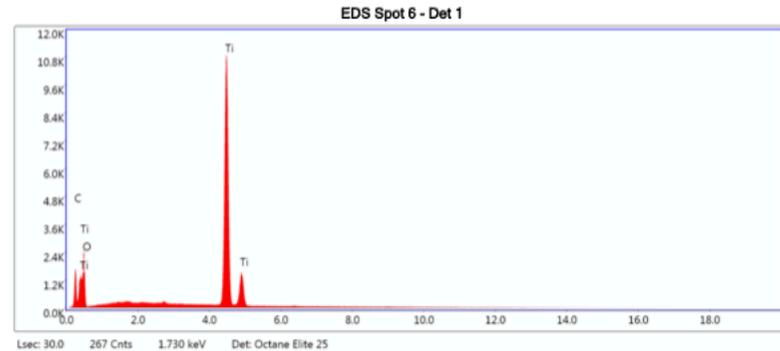
eZAF Smart Quant Results

Element	Weight %	Atomic %	Net Int.	Error %	Kratio	Z	A	F
C K	12.05	24.31	671.08	7.71	0.0592	1.1697	0.4197	1.0000
O K	30.97	46.88	929.79	10.77	0.0337	1.1230	0.0969	1.0000
TiK	56.98	28.81	8949.60	1.54	0.5103	0.8824	1.0119	1.0027

PYRITE

EDS Spot 8 - Det 1
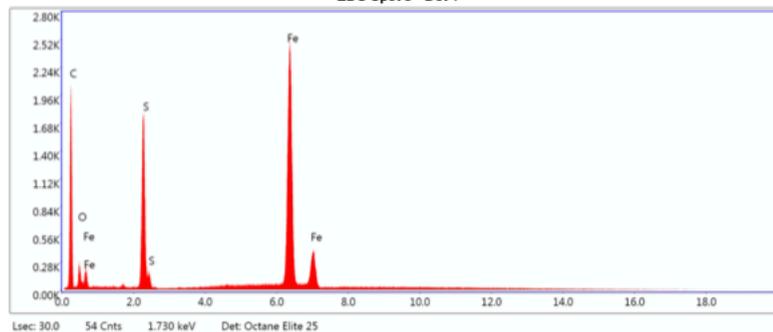
Lsec: 30.0   54 Cnts   1.730 keV   Det: Octane Elite 25

eZAF Smart Quant Results

Element	Weight %	Atomic %	Net Int.	Error %	Kratio	Z	A	F
C K	46.06	76.08	861.58	9.31	0.1223	1.1240	0.2362	1.0000
O K	2.96	3.67	99.50	13.76	0.0058	1.0790	0.1817	1.0000
S K	8.14	5.03	1224.14	3.29	0.0672	0.9673	0.8476	1.0073
FeK	42.84	15.22	2450.15	2.10	0.3644	0.8359	1.0101	1.0073

BARITE

EDS Spot 4 - Det 1
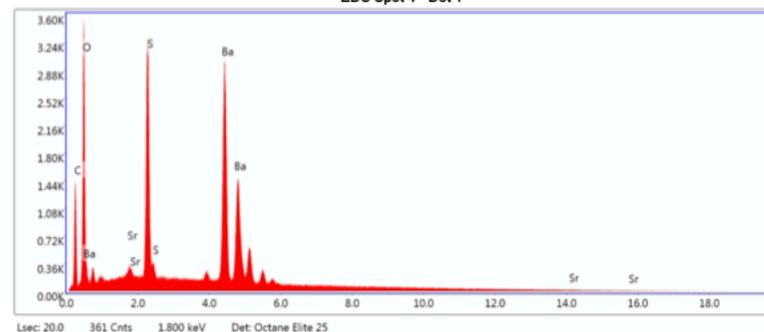
Lsec: 20.0   361 Cnts   1.800 keV   Det: Octane Elite 25

eZAF Smart Quant Results

Element	Weight %	Atomic %	Net Int.	Error %	Kratio	Z	A	F
C K	18.86	45.07	914.31	9.39	0.0613	1.2608	0.2578	1.0000
O K	19.05	34.18	2362.20	8.82	0.0652	1.2137	0.2818	1.0000
SrL	1.37	0.45	200.43	10.78	0.0084	0.8582	0.7129	1.0017
S K	11.10	9.93	3388.99	4.64	0.0881	1.0985	0.7119	1.0153
BaL	49.61	10.37	3750.91	2.58	0.4023	0.7711	1.0521	0.9996

APATITE-(F)

EDS Spot 2 - Det 1
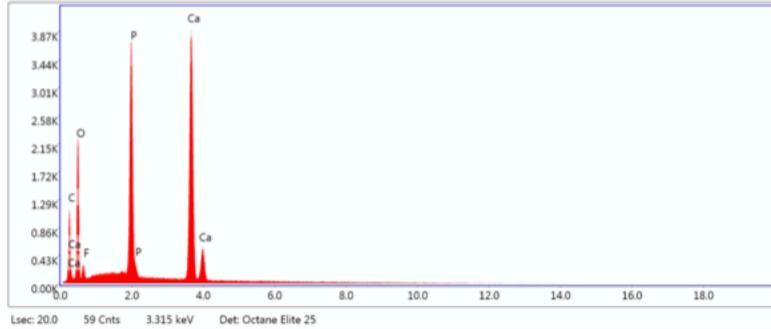
Lsec: 20.0   59 Cnts   3.315 keV   Det: Octane Elite 25

eZAF Smart Quant Results with SEC (BCNOF_2017-09-14)

Element	Weight %	Atomic %	Net Int.	Error %	Kratio	Z	A	F
C K	25.64	38.86	542.03	10.09	0.0716	1.0823	0.2580	1.0000
O K	33.01	37.57	1520.91	10.22	0.0492	1.0368	0.1437	1.0000
F K	6.21	5.95	219.57	12.74	0.0082	0.9640	0.1366	1.0000
P K	12.39	7.29	3633.92	2.79	0.0992	0.9068	0.8755	1.0080
CaK	22.75	10.34	4532.95	1.74	0.2012	0.8918	0.9860	1.0059

APATITE-(Cl)

EDS Spot 1 - Det 1
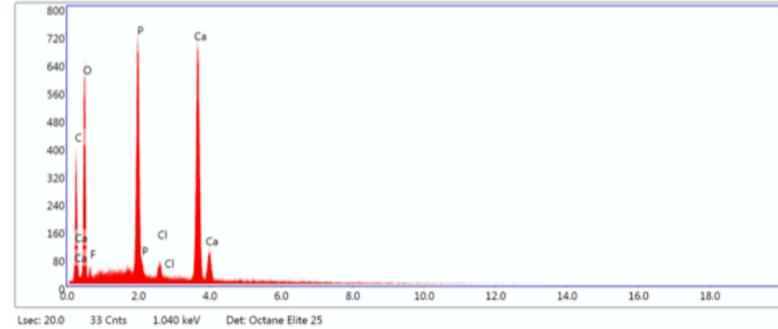
Lsec: 20.0   33 Cnts   1.040 keV   Det: Octane Elite 25

eZAF Smart Quant Results

Element	Weight %	Atomic %	Net Int.	Error %	Kratio	Z	A	F
C K	20.23	33.57	204.22	11.27	0.0597	1.1105	0.2655	1.0000
O K	32.02	39.89	414.54	11.01	0.0608	1.0589	0.1793	1.0000
F K	1.08	1.13	17.12	32.31	0.0020	0.9827	0.1927	1.0000
P K	14.53	9.35	692.04	3.51	0.1238	0.9166	0.9219	1.0081
ClK	1.26	0.71	49.96	17.61	0.0106	0.8873	0.9289	1.0201
CaK	30.88	15.35	815.17	2.97	0.2741	0.8964	0.9863	1.0041

ILMENITE

kV: 20   Mag: 386   Takeoff: 36.8   Live Time(s): 20   Amp Time(µs): 7.68   Resolution:(eV) 132.4

EDS Spot 1 - Det 1
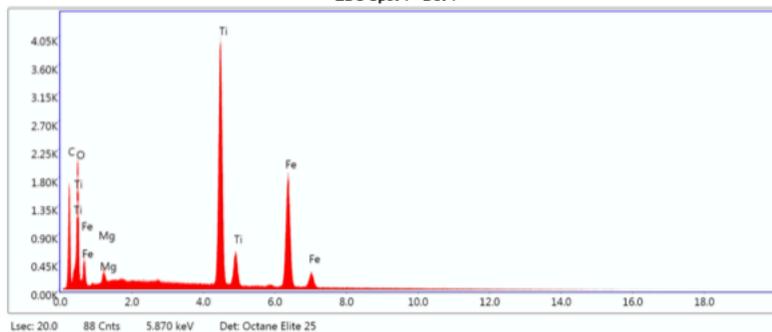
Lsec: 20.0   88 Cnts   5.870 keV   Det: Octane Elite 25

eZAF Smart Quant Results with SEC (BCNOF_2017-09-14)

Element	Weight %	Atomic %	Net Int.	Error %	Kratio	Z	A	F
C K	29.04	49.33	1060.65	8.02	0.1251	1.1293	0.3815	1.0000
O K	25.04	31.93	1382.48	10.26	0.0399	1.0836	0.1471	1.0000
MgK	1.12	0.94	227.03	10.83	0.0044	1.0046	0.3889	1.0014
TiK	23.71	10.10	5000.79	1.90	0.2096	0.8503	1.0097	1.0297
FeK	21.09	7.70	2594.27	2.32	0.1762	0.8378	0.9853	1.0125

IRON OXIDE

kV: 20   Mag: 491   Takeoff: 36.9   Live Time(s): 20   Amp Time(µs): 7.68   Resolution:(eV) 132.4

EDS Spot 1 - Det 1
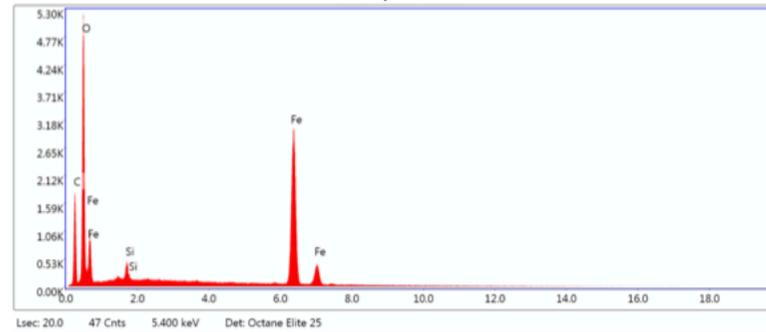
Lsec: 20.0   47 Cnts   5.400 keV   Det: Octane Elite 25

eZAF Smart Quant Results

Element	Weight %	Atomic %	Net Int.	Error %	Kratio	Z	A	F
C K	24.45	41.87	1129.51	8.72	0.0866	1.1259	0.3144	1.0000
O K	32.62	41.93	3550.15	8.28	0.1120	1.0805	0.3176	1.0000
SiK	1.08	0.79	286.11	8.94	0.0066	0.9874	0.6188	1.0033
FeK	41.86	15.41	4439.00	2.16	0.3577	0.8362	1.0138	1.0081

MAGNESIOFERRITE

EDS Spot 5 - Det 1

kV: 20 | Mag: 263 | Takeoff: 37 | Live Time(s): 20 | Amp Time(µs): 7.68 | Resolution:(eV) 132.4
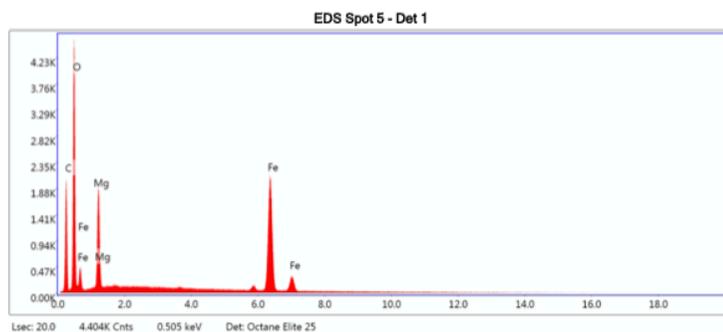
Lsec: 20.0   4.404K Cnts   0.505 keV   Det: Octane Elite 25

eZAF Smart Quant Results with SEC (BCNOF_2017-09-14)

Element	Weight %	Atomic %	Net Int.	Error %	Kratio	Z	A	F
C K	37.06	53.29	1196.77	8.37	0.1389	1.0825	0.3464	1.0000
O K	31.88	34.41	2865.18	9.05	0.0815	1.0373	0.2463	1.0000
MgK	6.71	4.77	1454.08	7.66	0.0276	0.9599	0.4281	1.0010
FeK	24.36	7.53	3001.76	2.32	0.2011	0.7978	1.0172	1.0174

IRON OXIDE WITH TITANIUM (Ti < 10 %)

EDS Spot 6 - Det 1

kV: 20 | Mag: 544 | Takeoff: 36.9 | Live Time(s): 20 | Amp Time(µs): 7.68 | Resolution:(eV) 132.4

Lsec: 20.0   91 Cnts   5.890 keV   Det: Octane Elite 25
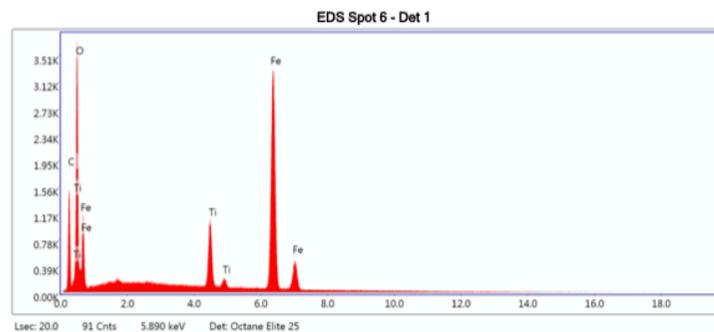
eZAF Smart Quant Results

Element	Weight %	Atomic %	Net Int.	Error %	Kratio	Z	A	F
C K	20.36	39.05	923.21	8.88	0.0730	1.1550	0.3106	1.0000
O K	26.88	38.72	2438.68	8.87	0.0794	1.1092	0.2663	1.0000
TiK	6.82	3.28	1230.68	3.05	0.0632	0.8732	0.9988	1.0633
FeK	45.95	18.96	4799.04	1.91	0.3995	0.8611	1.0033	1.0063

IRON OXIDE WITH CHROMIUM (Cr)

| kV: 20 | Mag: 268 | Takeoff: 37.4 | Live Time(s): 20 | Amp Time(µs): 7.68 | Resolution:(eV) 132.4 |
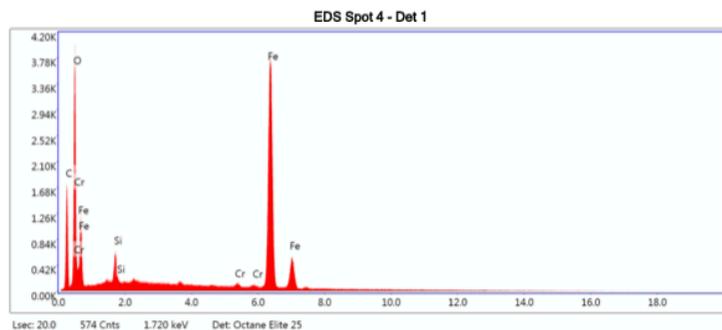
EDS Spot 4 - Det 1

Lsec: 20.0   574 Cnts   1.720 keV   Det: Octane Elite 25

eZAF Smart Quant Results with SEC (BCNOF_2017-09-14)

Element	Weight %	Atomic %	Net Int.	Error %	Kratio	Z	A	F
C K	33.19	56.19	1023.57	8.73	0.1202	1.1275	0.3212	1.0000
O K	21.02	26.72	2048.52	9.00	0.0592	1.0823	0.2600	1.0000
SiK	1.13	0.82	359.93	7.86	0.0070	0.9894	0.6259	1.0033
CrK	0.39	0.15	72.22	17.03	0.0039	0.8425	1.0107	1.1626
FeK	44.27	16.12	5528.12	1.98	0.3785	0.8383	1.0128	1.0070

IRON PHASE

| kV: 20 | Mag: 277 | Takeoff: 36.9 | Live Time(s): 20 | Amp Time(µs): 7.68 | Resolution:(eV) 132.4 |

EDS Spot 1 - Det 1

Lsec: 20.0   509 Cnts   1.740 keV   Det: Octane Elite 25
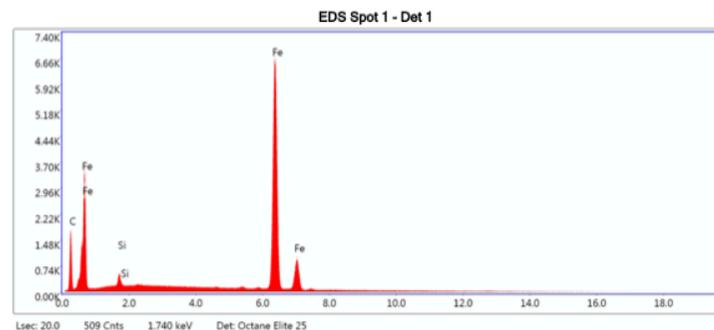
eZAF Smart Quant Results

Element	Weight %	Atomic %	Net Int.	Error %	Kratio	Z	A	F
C K	23.82	58.95	1081.78	9.38	0.0735	1.2183	0.2534	1.0000
SiK	0.95	1.00	265.93	10.56	0.0054	1.0750	0.5313	1.0031
FeK	75.23	40.04	9727.69	1.75	0.6951	0.9162	1.0065	1.0017

XENOTIME

kV: 20	Mag: 286	Takeoff: 36.7	Live Time(s): 30	Amp Time(µs): 7.68	Resolution:(eV) 132.4
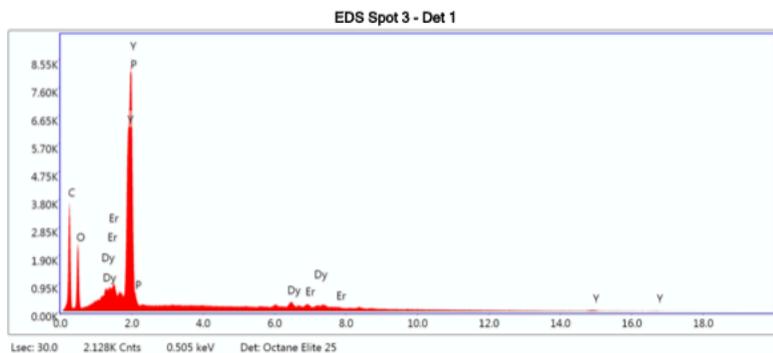
EDS Spot 3 - Det 1

Lsec: 30.0   2.128K Cnts   0.505 keV   Det: Octane Elite 25

eZAF Smart Quant Results with SEC (BCNOF_2017-09-14)

Element	Weight %	Atomic %	Net Int.	Error %	Kratio	Z	A	F
C K	54.44	76.25	1491.90	9.44	0.1339	1.0954	0.2245	1.0000
O K	15.55	16.35	1000.31	10.52	0.0219	1.0511	0.1343	1.0000
Y L	17.05	3.23	3825.90	1.72	0.1319	0.7435	1.0413	0.9999
P K	6.48	3.52	2705.99	3.49	0.0499	0.9233	0.8332	1.0020
DyL	3.63	0.38	258.25	10.20	0.0244	0.6233	1.0706	1.0086
ErL	2.86	0.29	182.95	13.94	0.0189	0.6157	1.0649	1.0079

MONAZITE

kV: 20	Mag: 252	Takeoff: 37	Live Time(s): 20	Amp Time(µs): 7.68	Resolution:(eV) 132.4
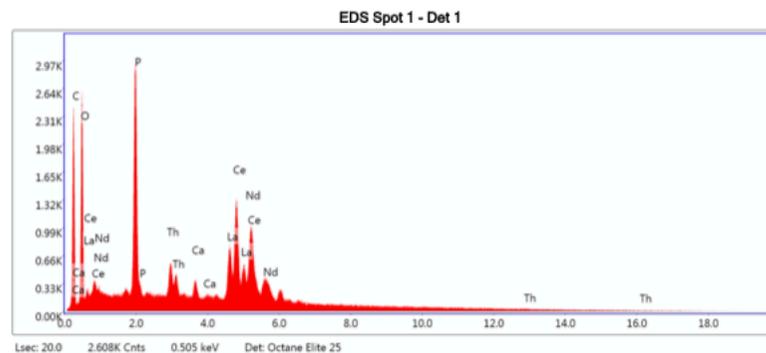
EDS Spot 1 - Det 1

Lsec: 20.0   2.608K Cnts   0.505 keV   Det: Octane Elite 25

eZAF Smart Quant Results with SEC (BCNOF_2017-09-14)

Element	Weight %	Atomic %	Net Int.	Error %	Kratio	Z	A	F
C K	35.48	65.06	1442.34	8.35	0.1481	1.1876	0.3516	1.0000
O K	16.21	22.32	1554.19	9.76	0.0391	1.1425	0.2110	1.0000
P K	8.81	6.26	2805.54	5.14	0.0595	1.0103	0.6659	1.0048
ThM	3.83	0.36	476.96	10.69	0.0297	0.6616	1.1538	1.0144
CaK	1.04	0.57	276.67	12.53	0.0095	0.9997	0.9060	1.0132
LaL	9.63	1.53	863.42	6.56	0.0744	0.7245	1.0608	1.0056
CeL	17.98	2.83	1551.17	3.76	0.1388	0.7282	1.0591	1.0010
NdL	7.02	1.07	552.91	8.29	0.0534	0.7262	1.0496	0.9979

CHROMITE

EDS Spot 2 - Det 1
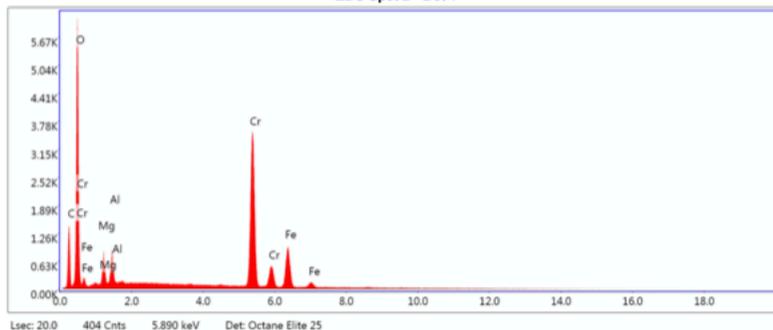
Lsec: 20.0   404 Cnts   5.890 keV   Det: Octane Elite 25

eZAF Smart Quant Results

Element	Weight %	Atomic %	Net Int.	Error %	Kratio	Z	A	F
C K	19.00	35.46	872.90	9.05	0.0652	1.1475	0.2992	1.0000
O K	27.84	39.01	3633.44	7.82	0.1118	1.1016	0.3645	1.0000
MgK	3.62	3.34	615.54	9.02	0.0137	1.0218	0.3704	1.0013
AlK	3.03	2.52	660.73	8.08	0.0146	0.9847	0.4895	1.0021
CrK	33.97	14.65	4893.28	2.06	0.3028	0.8574	1.0102	1.0293
FeK	12.55	5.04	1311.51	3.27	0.1031	0.8531	0.9529	1.0109

ANKERITE

EDS Spot 1 - Det 1
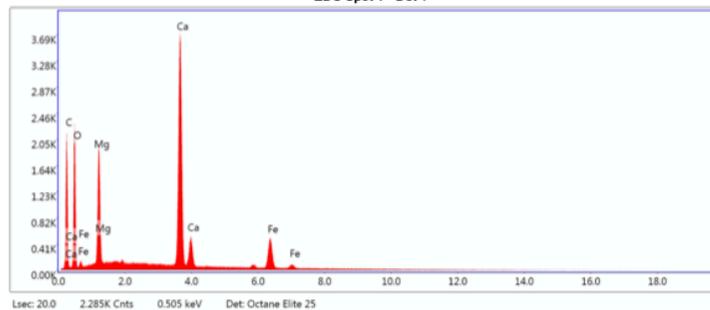
Lsec: 20.0   2.285K Cnts   0.505 keV   Det: Octane Elite 25

eZAF Smart Quant Results with SEC (BCNOF_2017-09-14)

Element	Weight %	Atomic %	Net Int.	Error %	Kratio	Z	A	F
C K	36.55	52.20	1292.29	7.60	0.1640	1.0708	0.4189	1.0000
O K	30.30	32.49	1427.64	10.32	0.0444	1.0257	0.1427	1.0000
MgK	6.72	4.74	1551.28	6.79	0.0322	0.9486	0.5036	1.0017
CaK	20.29	8.69	4287.54	1.78	0.1828	0.8824	1.0082	1.0124
FeK	6.13	1.88	679.28	3.67	0.0497	0.7872	0.9970	1.0343

TOURMALINE

| kV: 20 | Mag: 295 | Takeoff: 36.9 | Live Time(s): 20 | Amp Time(µs): 7.68 | Resolution:(eV) 132.4 |
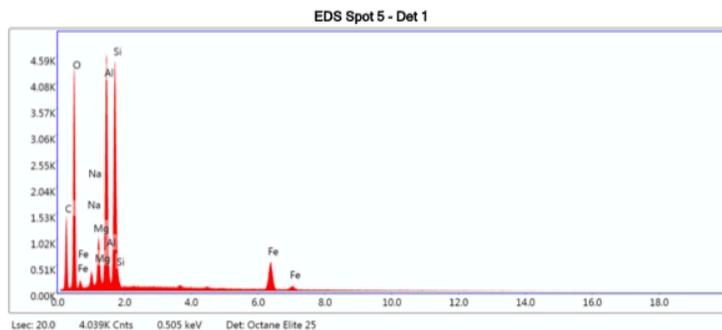
EDS Spot 5 - Det 1

Lsec: 20.0   4.039K Cnts   0.505 keV   Det: Octane Elite 25

eZAF Smart Quant Results with SEC (BCNOF_2017-09-14)

Element	Weight %	Atomic %	Net Int.	Error %	Kratio	Z	A	F
C K	37.36	50.42	866.49	9.87	0.0874	1.0611	0.2206	1.0000
O K	32.90	33.34	2908.52	9.29	0.0718	1.0155	0.2150	1.0000
NaK	1.18	0.83	216.08	11.75	0.0044	0.9224	0.4017	1.0020
MgK	2.47	1.65	793.60	6.71	0.0131	0.9381	0.5624	1.0035
AlK	10.55	6.34	4002.32	4.59	0.0655	0.9033	0.6849	1.0034
SiK	10.14	5.86	3964.76	4.45	0.0660	0.9231	0.7028	1.0020
FeK	5.40	1.57	777.48	3.55	0.0452	0.7767	1.0148	1.0621

AMPHIBOLE

| kV: 20 | Mag: 286 | Takeoff: 37.4 | Live Time(s): 20 | Amp Time(µs): 7.68 | Resolution:(eV) 132.4 |

EDS Spot 3 - Det 1

Lsec: 20.0   6.568K Cnts   1.720 keV   Det: Octane Elite 25
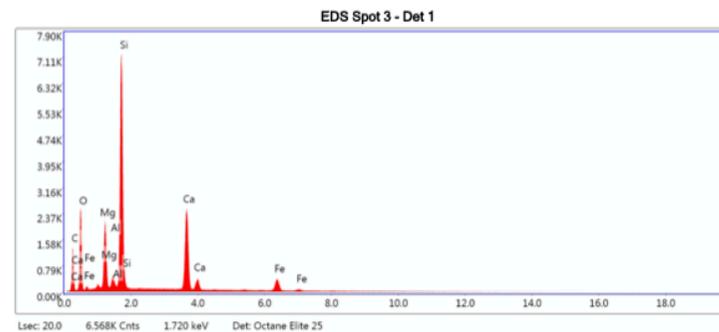
eZAF Smart Quant Results

Element	Weight %	Atomic %	Net Int.	Error %	Kratio	Z	A	F
C K	25.66	40.03	783.47	10.18	0.0547	1.0850	0.1965	1.0000
O K	27.85	32.62	1679.27	9.96	0.0484	1.0395	0.1673	1.0000
MgK	6.65	5.12	1708.26	6.17	0.0358	0.9617	0.5586	1.0030
AlK	1.20	0.84	343.02	7.68	0.0072	0.9263	0.6378	1.0052
SiK	19.69	13.13	6623.25	3.84	0.1403	0.9468	0.7504	1.0032
CaK	14.40	6.73	2916.83	2.21	0.1260	0.8946	0.9662	1.0121
FeK	4.54	1.52	506.58	4.35	0.0376	0.7981	0.9953	1.0415

UNKNOWN

Several minerals which were found could not be identified. These are found under the datapoint "unknown" but are here labelled according to which formation they belong to.

Unknown.CCE.A

| kV: 20 | Mag: 433 | Takeoff: 36.8 | Live Time(s): 100 | Amp Time(µs): 7.68 | Resolution:(eV) 132.4 |
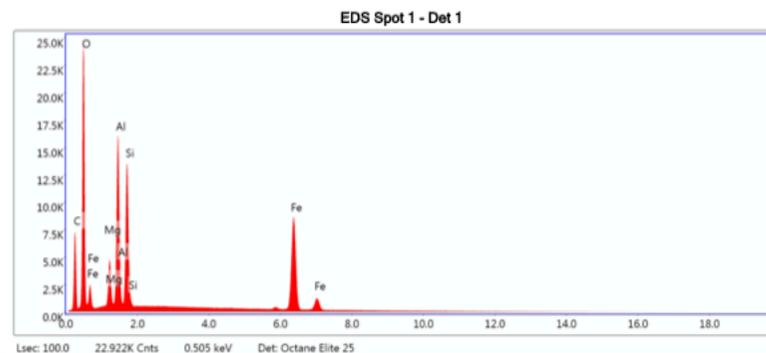
EDS Spot 1 - Det 1

Lsec: 100.0   22.922K Cnts   0.505 keV   Det: Octane Elite 25

eZAF Smart Quant Results with SEC (BCNOF_2017-09-14)

Element	Weight %	Atomic %	Net Int.	Error %	Kratio	Z	A	F
C K	33.34	48.35	884.59	8.93	0.0889	1.0811	0.2468	1.0000
O K	32.51	35.39	3305.42	8.71	0.0813	1.0357	0.2415	1.0000
MgK	2.59	1.86	719.83	6.99	0.0118	0.9580	0.4746	1.0019
AlK	7.98	5.15	2724.59	5.24	0.0444	0.9228	0.6021	1.0023
SiK	6.16	3.82	2332.07	4.73	0.0386	0.9432	0.6633	1.0026
FeK	17.43	5.44	2490.66	1.94	0.1442	0.7953	1.0145	1.0254

Unknown.VV1.A

| kV: 20 | Mag: 252 | Takeoff: 37 | Live Time(s): 20 | Amp Time(µs): 7.68 | Resolution:(eV) 132.4 |
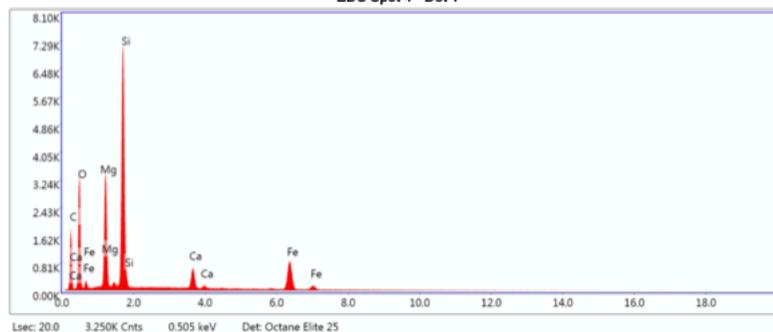
EDS Spot 4 - Det 1

Lsec: 20.0   3.250K Cnts   0.505 keV   Det: Octane Elite 25

eZAF Smart Quant Results with SEC (BCNOF_2017-09-14)

Element	Weight %	Atomic %	Net Int.	Error %	Kratio	Z	A	F
C K	40.68	55.61	1078.61	9.55	0.0998	1.0629	0.2308	1.0000
O K	26.52	27.21	2254.40	9.69	0.0511	1.0176	0.1893	1.0000
MgK	8.09	5.46	2830.86	5.97	0.0428	0.9404	0.5615	1.0023
SiK	14.35	8.39	6560.50	3.87	0.1001	0.9256	0.7522	1.0025
CaK	2.45	1.00	693.25	3.91	0.0215	0.8740	0.9798	1.0265
FeK	7.91	2.33	1221.00	3.01	0.0652	0.7793	1.0119	1.0451

Unknown.VV1.B

| kV: 20 | Mag: 265 | Takeoff: 37 | Live Time(s): 20 | Amp Time(µs): 7.68 | Resolution:(eV) 132.4 |

EDS Spot 10 - Det 1
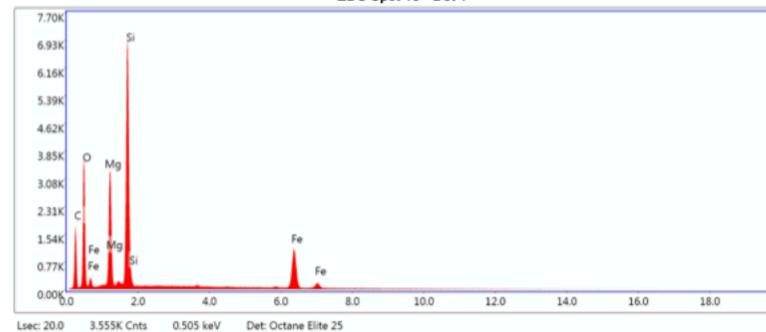
Lsec: 20.0   3.555K Cnts   0.505 keV   Det: Octane Elite 25

eZAF Smart Quant Results with SEC (BCNOF_2017-09-14)

Element	Weight %	Atomic %	Net Int.	Error %	Kratio	Z	A	F
C K	40.51	55.51	1045.70	9.59	0.0980	1.0647	0.2273	1.0000
O K	26.79	27.56	2426.09	9.51	0.0557	1.0194	0.2039	1.0000
MgK	8.22	5.57	2775.94	6.10	0.0425	0.9422	0.5481	1.0021
SiK	14.21	8.33	6332.06	3.98	0.0979	0.9274	0.7413	1.0022
FeK	10.27	3.03	1563.68	2.78	0.0846	0.7810	1.0143	1.0401

Unknown.VV1.C

kV:	20	Mag: 242	Takeoff: 36.7	Live Time(s): 30	Amp Time(μs): 7.68	Resolution:(eV) 132.4
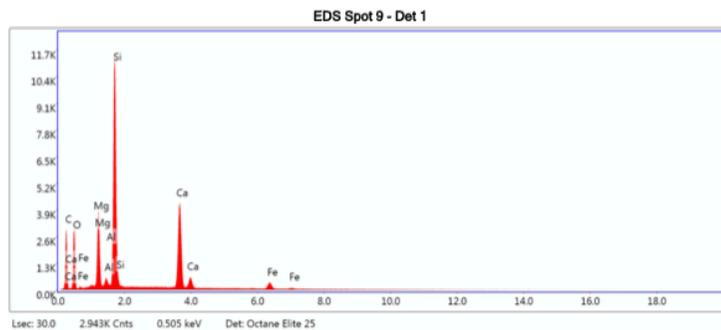
EDS Spot 9 - Det 1


Lsec: 30.0   2.943K Cnts   0.505 keV   Det: Octane Elite 25

eZAF Smart Quant Results with SEC (BCNOF_2017-09-14)

Element	Weight %	Atomic %	Net Int.	Error %	Kratio	Z	A	F
C K	43.62	59.83	1160.26	9.23	0.1136	1.0611	0.2456	1.0000
O K	20.93	21.55	1252.78	10.31	0.0300	1.0159	0.1411	1.0000
MgK	5.67	3.85	2002.51	5.61	0.0319	0.9389	0.5978	1.0032
AlK	0.55	0.34	215.35	9.36	0.0034	0.9042	0.6796	1.0057
SiK	15.06	8.83	6884.27	3.36	0.1108	0.9241	0.7934	1.0037
CaK	12.20	5.02	3239.94	1.85	0.1061	0.8726	0.9853	1.0120
FeK	1.97	0.58	288.49	5.37	0.0162	0.7780	1.0020	1.0552

Unknown.CH-D.A

kV:	20	Mag: 533	Takeoff: 36.9	Live Time(s): 20	Amp Time(μs): 7.68	Resolution:(eV) 132.4

EDS Spot 5 - Det 1

Lsec: 20.0   411 Cnts   1.730 keV   Det: Octane Elite 25
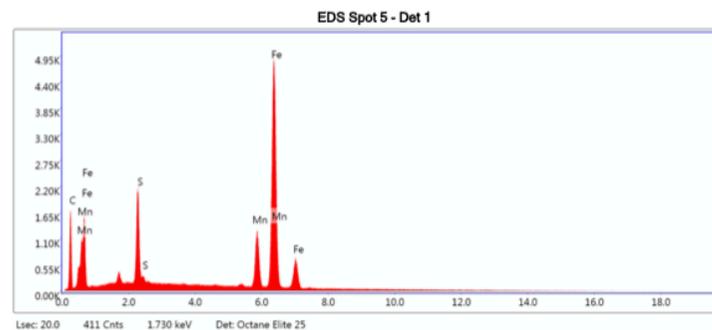
eZAF Smart Quant Results

Element	Weight %	Atomic %	Net Int.	Error %	Kratio	Z	A	F
C K	27.31	62.01	1037.09	9.70	0.0703	1.1990	0.2146	1.0000
S K	6.65	5.66	2067.83	4.00	0.0544	1.0371	0.7823	1.0076
MnK	10.83	5.38	1626.03	2.99	0.1024	0.8848	1.0021	1.0668
FeK	55.21	26.96	7014.70	1.82	0.4998	0.8994	1.0032	1.0033